# MODELLING THE EFFECT OF CONDENSATION AND EVAPORATION OF WATER ON THE TRANSIENT TEMPERATURES INSIDE THE EXHAUST SYSTEM OF AN IC ENGINE DURING A COLD START

Leanne Haworth

Thesis presented in partial fulfilment of the requirements for the degree
Master of Science in Engineering at the University of Stellenbosch


Thesis Supervisor: Mr RT Dobson

March 2010

DEPARTMENT OF MECHANICAL AND MECHATRONIC ENGINEERING
UNIVERSITY OF STELLENBOSCH

## Declaration

By submitting this dissertation electronically, I declare that the entirety of the work contained therein is my own, original work, that I am the owner of the copyright thereof (unless to the extent explicitly stated) and that I have not previously in its entirety or in part submitted it for obtaining any qualification.

Signature: 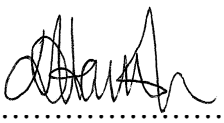 Date: 15/01/2010

# Abstract

The research presented here investigates the hypothesis that condensation and subsequent evaporation of water vapour present in the exhaust gas of an internal combustion engine occur in the sections of the exhaust system between the exhaust port and the catalytic converter exit. It is further hypothesised that these two-phase moisture effects influence the transient temperature profiles in the exhaust system, and potentially cause a delay in the time it takes for the catalytic converter to reach temperatures of 200-300 °C, which are required for light-off to occur.

In order to evaluate this hypothesis a transient, one-dimensional mathematical model of the thermo-fluid behaviour in the exhaust system during a cold start, including moisture effects, was created and solved by means of a computer algorithm. Heat and mass transfer theory was used to formulate the unsteady conservation equations for mass, energy and momentum. The two phase moisture effects were modelled using the analogy between heat and mass transfer, which predicts evaporation and heterogeneous condensation (the condensation of vapour against the pipe wall) due to a vapour pressure gradient between the bulk vapour and a saturated vapour at the surface of the liquid film. Homogeneous condensation (the condensation of liquid in the form of droplets in the gas stream) was also accounted for if the bulk gas temperature dropped below the bulk vapour saturation temperature.

An experimental investigation was performed using two engines, a 1.6 L Volkswagen Bora and a 1.6 L Ford RoCam, in the test cells of Cape Advanced Engineering Pty (Ltd). In order to measure the gas temperatures as accurately as possible specialised radiation shielded sensors with fast time response were designed and installed in the pipe sections of the exhaust systems of both engines. The shielded sensors measured temperatures up 50 °C higher than the conventional thermocouples installed at the same positions, which is in keeping with the results predicted by the theory governing errors associated with temperature measurement in the flowing gas in the exhaust system.

Comparison of the numerically simulated and experimentally measured temperatures indicated that in the sections of the exhaust system leading up to the catalytic converter the moisture has little influence on the temperature behaviour of the exhaust system. In these sections the convective heat transfer is dominant. In the catalytic converter the moisture effects were found to be influential. The experimental results clearly show an early rise in the gas temperatures, followed by a period of constant temperature at approximately the saturation temperature of the bulk vapour (referred to as the temperature plateau) at the catalytic converter mid-bed and exit. The numerically simulated gas temperatures also exhibited this plateau, but an initial very high and sharp peak in the simulated gas temperatures occurred at the start of the plateau. This was not seen in the experimental results and is attributed to non-equilibrium in the evaporation process, indicating that the

rate of evaporation predicted by the mass transfer model used is too high for this application and that the model needs to be refined. Further investigation of the influence of the individual mass transfer processes indicated that the homogeneous condensation is the dominant process in the formation of liquid in the catalytic converter. Heterogeneous condensation was found to occur, but produced a smaller mass of liquid. The maximum amount of liquid predicted to form in the catalytic converter was 12 g/cm, which translates to a film 0.05 mm thick if evenly distributed over the inner surface of the monolith.

In the simulation it was found that both evaporation and condensation are needed in order to simulate the temperature plateau, from which it was concluded that both these processes do occur and the first statement in the original hypothesis is valid. However, by the end of the test period temperatures simulated both with or without the moisture effects closely approached the final temperatures of the experimental investigation, indicating that the influence of the moisture is limited to the early stages of the catalytic converter warm-up. The second part of the hypothesis, postulating that the moisture behaviour caused a delay in the time taken to reach light-off temperature, is therefore concluded to be invalid.

The mathematical model constructed in this research is by necessity a simplified solution to complex thermo-fluid processes. It serves as useful groundwork for further elaboration and refinement of the theory related the moisture behaviour and its influence on the transient temperatures in the exhaust system.

# Opsomming

Die navorsing wat hier uiteengesit word ondersoek die hipotese dat kondensasie en die gevolglike verdamping van water wat teenwoordig is in die uitlaatgas van ‘n binnebrandenjin, plaasvind in die gedeeltes van die uitlaatstelsel tussen die uitlaatklep en die katalitiese-omsetter se uitlaat. Daar word verder veronderstel dat hierdie tweefasevloeieffekte die tydafhanklike temperatuurprofiele in die uitlaatstelsel beïnvloed, wat moontlik kan lei tot ‘n vertraging in die tydsduur vir die katalitiese omsetter om temperature van 200-300 °C te bereik, wat nodig is om noemenswaardige omsetting te bewerkstellig.

Om hierdie veronderstelling te evalueer is ‘n tydafhanklike, eendimensionele wiskundige model van die termo-vloei gedrag in die uitlaatstelsel gedurende ‘n koue inwerktreeding, insluitende vogtigheidseffekte, opgestel en opgelos deur van ‘n rekenaaralgoritme gebruik te maak. Warmte- en massaoordragsteorie was gebruik om die ongestadigde massa-, energie- en momentumbehoudsvergeleikings te formuleer. Die tweefasige vogeffekte was gemodelleer deur gebruik te maak van die verhouding tussen warmte- en massaoordrag, wat verdamping en heterogeniese kondensasie (die kondensasie van damp teen die pypwand) voorspel as gevolg van die dampdrukgradient tussen die grootmaat damp en die versadigde damp by die oppervlak van die vloeistoffilm. Homogene kondensasie (die kondensasie van vloeistof in die vorm van druppels in die dampstroom) was ook in aanmerking geneem indien die grootmaatgas temperatuur onder die versadigingstemperatuur van die grootmaatdamp gedaal het.

’n Eksperimentele ondersoek was gedoen deur van twee enjins gebruik te maak, ’n 1.6 L Volkswagen Bora en ’n 1.6 L Ford RoCam, in die toetsselle van Cape Advanced Engineering Pty (Ltd). Om die gastemperature so akkuraat moontlik te meet, was spesiale radiasiegeskermde sensore met vinnige reaksietyd ontwerp en installer in die pypseksies van die uitlaatstelsels van beide enjins. Die geskermde sensore het temperature van tot 50 °C hoër as konvensionele termokoppels in dieselfde areas gemeet. Dit is in koers is met resultate wat deur die foutbeperkingsteorie, geassosieer met die meet van temperature in vloeïende gas in uitlaatstelsels, voorspel word.

Vergelyking van die numeriese simulasie met die eksperimenteel gemete temperature het aangedui dat in dele van die uitlaatstelsel voor die katalitiese-omsetter, die vog min uitwerking het op die termiese gedrag van die stelsel. In hierdie gedeeltes is die konveksie warmte-oordrag dominant. In die katalitiese-omsetter was die vogeffekte invloedryk. Die eksperimentele resultate toon ‘n duidelike vroeë toename in die gastemperature, gevolg deur ‘n tydperk van konstante temperature by nagenoeg die versadigingstemperatuur van die grootmaatdamp (verwys na as die temperatuurplato) by die katalitiese-omsetter se kern en uitlaat. Die numeries gesimuleerde gastemperature het ook hierdie gedrag getoon, maar ‘n baie hoë en skerp piek by die begin van die plato het voorgekom.

Hierdie piek was nie te sien by die eksperimentele resultate nie en is toegeskryf aan nie-ewewigstoestande in die verdampingsproses, wat aandui dat die tempo van verdamping wat deur die massa-oordragmodel voorspel word te hoog is vir die model en dat dit verfyn moet word. Verdere ondersoek van die invloed van die individuele massa-oordragprosesse het getoon dat die homogene kondensasie die dominante proses is in die vorming van vloeistof in die katalitiese-omsetter. Heterogeniese kondensasie het plaasgevind, maar ‘n kleiner massa vloeistof is produseer. Die maksimum hoeveelheid vloeistof wat voorspel is om in die katalitiese-omsetter te vorm was 12 g/cm wat gelykstaande is aan ‘n film van 0.05 mm dik indien eweredig versprei oor die binneoppervlak van die monoliet.

Daar was in die simulasie gevind dat beide verdamping en kondensasie benodig word om die temperatuurplato te simuleer, vanwaar die gevolgtrekking gemaak kan word dat beide prosesse wel plaasvind en dat die eerste stelling in die oorspronklike hipotese wel geldig is. Daar was egter teen die einde van die toetsperiode gevind dat beide temperature wat met en sonder vogeffekte simuleer was, die eksperimentele temperature nagevolg het, wat aandui dat die invloed van vog beperk is tot die vroeë stadiums van die katalitiese-omsetter se opwarmingstydperk. Die tweede gedeelte van die hipotese wat veronderstel dat die voggedrag ‘n vertraging in die tydsduur om omsetting te bewerkstellig veroorsaak, is dus bevind om ongeldig te wees.

Die wiskundige model wat opgestel is tydens die ondersoek is weens noodsaaklikheid ‘n vereenvoudigde simulasie van komplekse termo-vloei prosesse. Dit dien as nuttige grondwerk vir verdere in-diepte ondersoeke en afronding van die teorie met betrekking tot voggedrag en die uitwerking daarvan op die tydsafhanklike temperature in ‘n uitlaatstelsel.

Dedicated to my mother

# Acknowledgements

The author would like to thank the following people:

Dr Andrew Taylor, for all his advice and for making the CAE test facilities available for this research.

Dr Arthur Bell, for his advice and technical expertise during the experimental phase of this research.

All the CAE employees who assisted with the experimental work, in particular Bart de Rouw for his diligent response to all the questions sent his way long after the testing had been concluded.

Mr Cobus Zietzmann and the employees of the Mechanical Engineering Department workshop, for the manufacture of the shielded temperature sensors.

Mr Robert Dobson, the supervisor of this thesis, for his advice, support and patience during the course of the research.

# Table of Contents

# Nomenclature

**Roman Letters**

| | |
|---|---|
| $A$ | Area, $m^2$ or mass based air/fuel ratio |
| a | Molar air/fuel ratio |
| $C$ | Coefficient of friction |
| $C_p$ | Constant pressure specific heat, kJ/kg·K |
| $C_v$ | Constant volume specific heat, kJ/kg·K |
| $D$ | Diameter, m or diffusivity |
| $F$ | Force, N |
| $H$ | Total enthalpy, J |
| $h$ | Heat transfer coefficient, $W/m^2$, mass transfer coefficient, $kg/m^2$ or specific enthalpy, J/kg |
| $i$ | Control volume number |
| $k$ | Thermal conductivity, W/m or a constant used in the Runge Kutta numerical solution |
| $L$ | Length, m |
| $M$ | Molar mass, kg/kmol |
| $m$ | Mass, kg |
| $\dot{m}$ | Mass flow rate, kg/s |
| $n$ | Control volume at the end of a section of the numerical model geometry |
| $P$ | Pressure, Pa |
| $\dot{Q}$ | Heat transfer rate, W |
| $R$ | Gas constant, kJ/kgK |
| $r$ | Recovery factor of a thermocouple in a flowing gas |
| $T$ | Temperature, K or °C |
| $t$ | Catalytic converter channel wall half thickness, m |
| $v$ | Velocity, m/s |
| $X$ | Mass fraction |
| $y$ | Mole fraction or radial distance from pipe wall (in boundary layer), m |
| $z$ | Liquid film or channel thickness, m |

**Greek Letters**

| | |
|---|---|
| $\alpha$ | Absorbtivity or number of moles of *C* in a mole of hydrocarbon fuel |
| $\beta$ | Number of moles of *H* in a mole of hydrocarbon fuel |
| $\gamma$ | Insentropic expansion exponent or number of moles of *O* in a mole of hydrocarbon fuel |
| $\delta$ | number of moles of *N* in a mole of hydrocarbon fuel |
| $\varepsilon$ | Emissivity |

| | |
|---|---|
| $\lambda$ | Ratio of real to stoichiometric air/fuel ratios |
| $\mu$ | Viscosity, $N \cdot s/m^2$ |
| $\rho$ | Density, $kg/m^3$ |
| $\sigma$ | Stefan-Boltzmann constant, $5.67 \times 10^{-8}$ $W/m^2 \cdot K^4$ |
| $\tau$ | Shear stress, $N/m^2$ |

**Subscripts**

| | |
|---|---|
| $\infty$ | Bulk gas condition |
| *AB* | Diffusivity of species *A* in Species *B* |
| *amb* | Ambient conditions |
| *cond* | Conduction |
| *conv* | Convection |
| *cs* | Cross section |
| *evap* | Evaporation |
| *g* | Exhaust gas excluding water vapour |
| *gL* | At interface between gas and liquid |
| *gw* | At interface between gas and wall |
| *h* | Hydraulic |
| *High* | Experimental high load case |
| *i* | Inside, control volume number or referring to an individual gas component in a mixture |
| *Input1* | Simulation input value for Experimental Setup 1 |
| *Input2* | Simulation input value for Experimental Setup 2 |
| *L* | Liquid water |
| *Low* | Experimental low load case |
| *Lw* | At interface between liquid and wall |
| *Med* | Experimental medium load case |
| *mix* | Total exhaust gas mixture |
| *mt* | Mass transfer |
| *o* | Outside |
| *p* | Pipe |
| *rad* | Radiation |
| *s* | Stoichiometric, surface or sheath |
| *v* | Water vapour |
| *w* | Wall |

**Superscripts**

| | |
|---|---|
| *j* | Time step number |
| *m* | Mass |

**Dimensionless Variables**

| | |
|---|---|
| *CAF* | Convective augmentation factor |
| Nu | Nusselt number |
| Pr | Prandtl number |
| $Re_D$ | Reynolds number (internal or external pipe flow) |
| $Re_L$ | Reynolds number (flat plate flow) |
| Sc | Schmidt number |
| Sh | Sherwood number |

**Abbreviations**

| | |
|---|---|
| BDC | Bottom Dead Centre (piston position) |
| CAE | Cape Automotive Engineering (Pty) Ltd |
| CAF | Convective Augmentation Factor |
| cv | Control Volume |
| ES1 | Experimental Setup 1 |
| ES2 | Experimental Setup 2 |
| ETA | Engine Test Automation (software) |
| EVC | Exhaust Valve Closes |
| EVO | Exhaust Valve Opens |
| PLC | Programmable Logic Controller |
| TDC | Top Dead Centre (piston position) |
| 1D | One dimensional |

**Artwork**

| | |
|---|---|
|  | Mass Flow |
|  | Heat Transfer |
|  | Momentum Transfer |
|  | Force |
|  | Shear Force |

# List of Figures

# List of Tables

# 1 Introduction

Since automotive catalytic converters first came into commercial production in 1979, the regulations regarding allowable automobile emissions have become increasingly strict. This has resulted in a drive to improve the performance of the catalytic converter. The reduction in emissions produced by the catalytic converter only becomes significant after temperatures in the range of 200-300 ºC are reached. At these temperatures the rate of exothermic reactions increases rapidly, known as light-off. The time taken for the catalytic converter to reach light-off strongly influences the amount of emissions produced, so understanding the warm-up process of the catalytic converter is important. This thesis investigates condensation and evaporation of water vapour in the exhaust gases during a cold start in order to predict what effect these processes have on the transient temperatures in the exhaust system and the catalytic converter light-off time.

## 1.1 Motivation

The motivation for the research presented here is based on two observed phenomena in gasoline engine exhaust systems. The first phenomenon is the formation of substantial amounts of mist as well as the presence of a small liquid flow at the exhaust system outlet during a cold start. The concentration of water vapour in the exhaust gas is high due to water being one of the main combustion products in a gasoline engine. It is therefore not unexpected that condensation occurs at some point in the exhaust system, especially in the downstream sections and near the outlet where the exhaust gases have been significantly cooled. It is, however, not clearly defined at what position in the exhaust system this condensation begins to occur, or for how long it continues. The focus of this research is to determine if the moisture has any influence in the section of the exhaust system upstream of and including the catalytic converter.

The possibility of relevant moisture effects in the catalytic converter is suggested by the second observed phenomenon. This is a slight rise in the gas temperatures followed by an extended period of constant temperature (referred to as the ‘temperature plateau’) measured inside the catalytic converter in the early stages of warm-up. This plateau, observed in the experimental work of Marais (2004), Chan and Hoang (1999) and Clarkson and Benjamin (1995), is not satisfactorily reproduced by conventional theoretical models of the exhaust system in which only single phase mass transfer is included. Furthermore the plateau was found to occur at approximately the saturation temperature of the vapour in the exhaust gas, which implies its presence is a result of the moisture behaviour.

If liquid water is present on the catalytic converter walls, energy will be required to evaporate it, which would cause a delay in the warm-up of the system. Liquid water may be present in the catalytic converter if condensation of the water vapour in the exhaust gases occurs while the system is still cool. An initial amount

of water may also be present before start-up due to water being previously absorbed by the porous ceramic from which the catalytic converter is made (Clarkson and Benjamin, 1995).

From these two observed phenomena the hypothesis of this research is constructed. This hypothesis proposes that during a cold start the two-phase behaviour of the water influences the warm-up characteristics of the exhaust system in the section between the exhaust port and the catalytic converter outlet. Furthermore, the evaporation of liquid present in the catalytic converter requires energy and subsequently causes a delay in the time it takes for the catalytic converter to reach light-off. The goals of this research are set with the aim of determining the validity of this hypothesis.

## 1.2 Research Goals

The primary goal of this research is to develop a theoretical model of the state of the exhaust gases and water vapour in the exhaust system (from the exhaust port to the exit of the catalytic converter) during a cold start, including two-phase moisture effects. This model is then to be solved numerically by means of a computer simulation in order to predict the effects of the moisture on the transient temperatures in the exhaust system. The simulation should also predict the mass, position and duration of any liquid accumulation that occurs in the system.

The inclusion of these moisture effects in a model of exhaust gas flow is a subject that has received little attention in the literature. The numerical simulation therefore aims to be as comprehensive as possible while using simplified modelling methods. The results of this simple model will be used to determine which parameters are most influential to the moisture behaviour and how well the current two phase mass transfer theory performs in this application, in order to create a foundation for more complex models in future research.

An experimental investigation is also performed and measurements of the temperatures in the exhaust system taken in order for the relevance of the theoretical model to be assessed. As the true, transient gas temperatures are desired, a specialised temperature sensor with a fast time response and minimal measurement error is required. The design and manufacture of such a sensor for use in the experimental investigation are also goals of this project. It should be noted here that although the catalytic converter is to be included in the model, it is not a goal of this research to simulate the exothermic reactions and associated gas species interactions occurring in a reactive catalytic converter. For this reason the experimental investigation is limited to the low temperature period before light-off is expected to occur. In this way the moisture effects can be investigated individually, without being combined with the exothermic reaction effects.

## 1.3 Thesis Overview

This research initially presents a literature study in which relevant background, related work undertaken by others and applicable theory are discussed. The formulation of the mathematical model from the theory is discussed in Section 3. A diagrammatic representation of the solution method for the numerical simulation is provided in Section 3, while a more detailed discussion of the solution procedure is provided in Appendix C, along with a sample calculation.

The theory concerning temperature measurement errors in gas flows and the design of the specialised temperature sensor based on this theory is discussed in Section 4. Predictions are made of the temperature measurement error expected when using the specially designed sensor. This error is then compared to that expected when using conventional thermocouples so that the new design can be evaluated.

The experimental investigation is discussed in Section 5 and the results of both the numerical model and experimental investigation are presented in Section 6. Section 6 also includes brief discussions in which the general trends in the temperature behaviour of the experimental results are identified and compared to those in the simulated results. From this comparison points of interest that require further explanation are identified.

Detailed discussions of points of interest from the experimental investigation and the numerical simulation are provided in Section 7. In these discussions the performance of the experimental and numerical simulation methods is assessed. The effect of varying values in the moisture model is investigated in some detail so that the influence of the moisture model on the simulated temperatures can be understood. Conclusions regarding the actual behaviour of the moisture in the exhaust system are then drawn. General conclusions of the research and recommendations for future work are provided in Sections 8 and 9.

# 2 Literature Study

Before the mathematical model of the exhaust system can be developed it is necessary to gain background knowledge of the structure of and processes occurring in the exhaust system. Related work found in the literature is studied and the general theory governing the thermo-fluid behaviour in the system defined.

## 2.1 Background

The main components of a *generalised* automobile exhaust system are shown in Figure 2.1. The hot end of the exhaust system starts at the exhaust port and consists of the manifold, takedown pipe and catalytic converter. The remainder of the system, the tailpipe, contains the silencer and ends at the exhaust outlet.

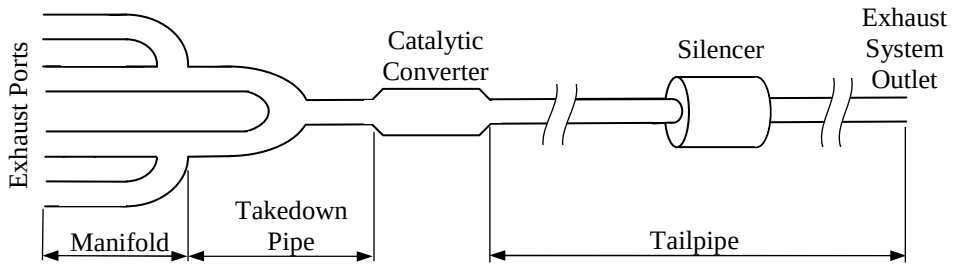


**Figure 2.1 Main Components of an Automobile Exhaust System**

The manifold is usually made of cast iron with thicker walls than the rest of the exhaust system in order to withstand the long term effects of the high temperature gas exiting the cylinder at the exhaust port. On a four cylinder engine the four pipes of the manifold will each experience gas flow during one of the four strokes of the cycle. These four gas flows are combined, out of phase, at the exit of the manifold into two flows (for a 2 into 1 takedown pipe, as shown in Figure 2.1). The gas exits the takedown pipe in a single, continuous flow with a mass flow rate of approximately the same magnitude as a single manifold pipe flow during the open valve period. The takedown pipe is usually made of thinner walled steel.

The gases enter the catalytic converter where the exothermic reactions which reduce the amounts of regulated emissions occur. A three-way catalytic converter is characterised by three main chemical reactions, namely the reduction of nitrogen oxides, the oxidation of carbon monoxide and the oxidation of un-burnt hydrocarbons. These reactions occur in the presence of a catalyst (usually platinum), so a large surface area for contact between the gas and the catalyst is desirable. A common structure for automobile catalytic converters is a ceramic monolith consisting of many small square channels. A thin layer of platinum is deposited onto the walls of these channels. The monolith is surrounded by a layer of heat resistant matting which provides mechanical insulation against vibration and some thermal insulation to the ceramic structure. This is then housed in a

stainless steel outer cylinder, which attaches the takedown outlet to the tailpipe inlet section. This structure is illustrated in Figure 2.2.

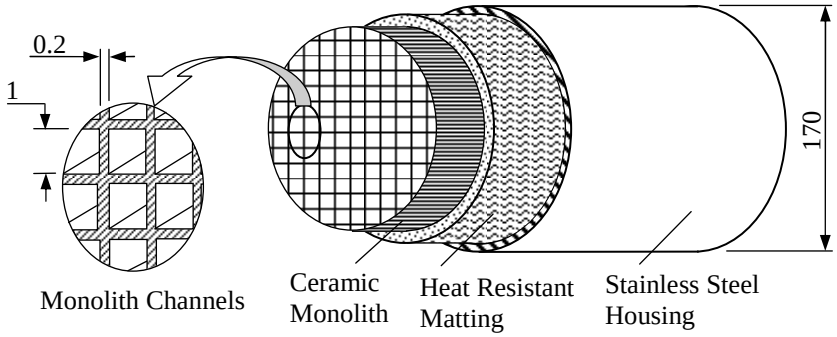


**Figure 2.2 Basic Structure of a Catalytic Converter with Typical Dimensions (mm)**

The exothermic reactions begin to occur as a function of the temperature in the catalytic converter. When the temperatures in the catalytic converter reach approximately 250-350 °C the reaction rate will approach half the maximum reaction rate that occurs in a fully warmed system (Chan and Hoang, 1999). This 50% reaction rate is defined as the *light-off* (Ferguson and Kirkpatrick, 2001) and after this point the exothermic heat generated by the reactions themselves causes the temperatures to rise quickly. Even though some reactions occur in the early stages of the warm-up, before light-off the catalytic converter does not produce a significant reduction in emissions. About 70% of the total emissions produced in a regulated emissions test cycle are produced in the time (approximately 150 s) before light off (Laing, 1994).

Reducing the time taken to light-off is therefore a very effective way of reducing emissions. Current methods of reducing this time are, for example, by pre-heating the monolith by means of electrical heating coils (Laing, 1994), by insulating the catalytic converter so that it remains warm for up to 24 hours after engine shutdown (Burch *et al.*,1996) or by diluting the pre-cat exhaust gases with air to produce secondary combustion which increases the temperature of the gases entering the catalytic converter (Blint and Haworth, 2000).

## 2.2 Related Work in Literature

Moisture effects inside the exhaust system, especially inside the catalytic converter, have been previously noted and investigated by a limited number of researchers in various levels of detail.

The significance of moisture effects on the transient thermal behaviour of an exhaust system was highlighted by Marais (2004). In his work the mathematical modelling of the thermal behaviour from exhaust port to catalytic converter outlet was undertaken and compared to experimental results. The model did not initially include moisture effects. In the experimental results of Marais's work the temperature plateau (discussed in Section 1.1) was observed, but was not reflected

in the model results. This was attributed to the absence of the moisture effects. The moisture effects were then accounted for by the addition of an approximated heat transfer term out of the gas, representing the heat required to evaporate liquid from the walls. This produced an improvement in the correlation between the theoretical and experimental results.

The effect of moisture on a catalytic converter warm-up and light-off was investigated by Clarkson and Benjamin (1995). In their work a one-dimensional model of the condensation and evaporation processes was formulated based on the concentration gradient between the vapour at the surface of a liquid layer and the bulk vapour, and the diffusivity of the vapour in the exhaust gas. This model was combined with an existing catalyst CFD model in order to simulate the thermo-fluid processes in the catalytic converter. In the experimental work on which their model was based the engine was pre-warmed (with the catalytic converter isolated from the rest of the system) and the exhaust gas temperature and composition was taken to be constant. The moisture content of the incoming exhaust gas was estimated as 0.076 kg/kg dry gas and an initial moisture content of 10 kg/m$^3$ in the monolith was accounted for. The inclusion of the moisture effects allowed the model to replicate the temperature plateau observed in their experimental results. It was concluded in their work that the moisture effects could produce a delay in the time taken for light-off to be reached, provided the light-off occurs towards the back of the monolith (downstream). This could occur, for example, when poisoning of the front portion of the converter occurs.

Heat transfer in the exhaust system of a cold start engine was investigated by Chan and Hoang (1999), including exhaust manifold and catalytic converter. The temperature plateau was also observed in their experimental work. A comparison of measured temperature values with those calculated when moisture effects were ignored showed a significant discrepancy during the first 100 s of warm up, as shown in Figure 2.3.

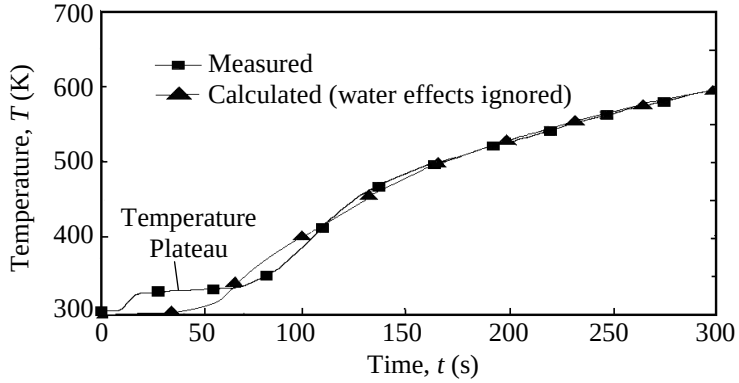


**Figure 2.3 Measured and Calculated Temperatures Downstream of the Catalytic Converter (Chan and Hoang, 1999)**

In order to model the moisture effects a dew point temperature for the vapour, defined as the temperature above which no condensation occurs, was estimated

from the gas composition. The rate of heat transfer was adjusted according to whether the wall temperature was below this dew point temperature, when it was assumed to be wetted by condensation, or above it, when it was assumed to be dry. The actual liquid-vapour two-phase phenomena were not considered in the study but the inclusion of the variable heat transfer rate improved the correlation of their experimental and numerical results.

## 2.3 Applicable Theory

The mathematical model of the exhaust system needs to include heat transfer and mass transfer processes. Simultaneous heat and mass transfer occur and various modes of condensation and evaporation are possible. In order to determine which theory is applicable the flow behaviour and conditions in the exhaust system must first be considered.

### 2.3.1 Basic IC Engine Theory

For the processes in the exhaust system to be modelled the state and composition of the gas must be determined by consideration of the combustion and exhaust processes.

#### 2.3.1.1 The Combustion Process

The chemical composition and hence the properties of the exhaust gasses is decided by the combustion processes that occur in the cylinder. The gas composition after combustion is effected by the ratio of fuel to air present, the type of fuel and how completely the fuel is burnt. If exactly enough air is present for the fuel to be completely burnt the air/fuel ratio is said to be stoichiometric. For gasoline ($C_7H_{17}O_0N_0$), the (mass based) stoichiometric air/fuel ratio is:

$$A_s = \left( \frac{m_{air}}{m_{fuel}} \right)_{stoichiometric} = 15.27 \qquad 2.1$$

For actual combustion processes the air/fuel ratio is never perfectly stoichiometric. The ratio of the real air fuel ratio $A$ to the stoichiometric air/fuel ratio $A_s$ is used in engine testing and control and is represented by:

$$\lambda = \frac{A}{A_s} \qquad 2.2$$

The overall mass flow rate into the system can be calculated from measured fuel flow rates and $\lambda$:

$$\dot{m}_{Total} = \dot{m}_{air} + \dot{m}_{fuel} = \lambda A_s \dot{m}_{fuel} + \dot{m}_{fuel} \qquad 2.3$$

Non-stoichiometric combustion processes produce various gas species, which remain in temperature dependent chemical equilibrium be represented by:

$$C_\alpha H_\beta O_\gamma N_\delta + a_s (O_2 + 3.76 N_2) \rightarrow n_1 CO_2 + n_2 H_2O + n_3 N_2 + n_4 O_2 + n_5 CO + n_6 H_2 \qquad 2.4$$

The values of the unknown constants $n_{1\text{-}6}$ are determined according to the value of λ. A sample calculation of this procedure is provided in Appendix B.

When the composition of the gas has been determined, the relevant gas properties can be calculated. For the purposes of this study the exhaust gas is treated as a mixture of water vapour and the combination of the remaining exhaust gases. In the interest of clarity the vapour will be referred to as the 'vapour' and the remaining constituent gasses as the 'gas'. The vapour properties are obtained from steam tables for the appropriate conditions, while the gas properties need to be calculated according to the mixture composition. The mole fraction of each component of the gas is converted to a mass fraction

$$X_i^m = \frac{y_i M_i}{\sum y_i M_i} \qquad 2.5$$

from which the gas properties $R_g = \sum R_i X_i^m$, $C_{pg} = \sum C_{pi} X_i^m$ and $C_{vg} = C_{pg} - R_g$ are calculated.

#### 2.3.1.2 The Exhaust Process

The velocity and the temperature of the gas entering the exhaust system are functions of the piston crank angle, which results in highly transient, cyclic behaviour. The exhaust stroke is illustrated in Figure 2.4. As the exhaust valve opens (EVO), usually at a crank angle of 45° before bottom dead centre (BDC) for conventional timing (Ferguson and Kirkpatrick, 2001), the gas in the cylinder is at a much higher pressure than the exhaust system. This results in a rapid outflow of the gas as it expands into the exhaust system. This is the blow-down stage of the exhaust stroke and produces the highest peak in the gas velocity. As the cylinder pressure drops the velocity decreases again.

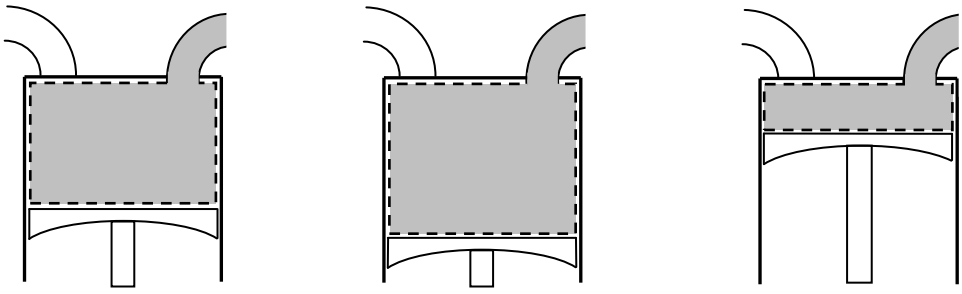


**Figure 2.4 Exhaust Process 45° before BDC, at BDC and at TDC**

The second stage of the exhaust process occurs when the piston passes through BDC and starts the upward exhaust stroke. This forces the remaining gas out and results in a second, lesser, peak in the gas velocity. This characteristic double peak

velocity behaviour of reciprocating engines between EVO and EVC (exhaust valve closes) is illustrated in Figure 2.5 (Abu-Qudais, 1997).

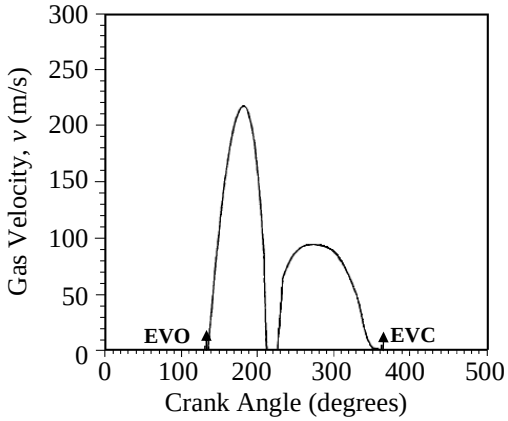


**Figure 2.5 Instantaneous Gas Velocity at the Exhaust Port between EVO and EVC (Abu Qudais, 1997)**

The exhaust temperature at the valve also exhibits an initial peak followed by a decrease associated with the expansion cooling of the gas. A stage of slow decrease in gas temperature (due to heat transfer losses) follows before the valve closes at 10° after top dead centre (TDC), for conventional timing. This behaviour is illustrated in Figure 2.6 (Abu-Qudais, 1997).

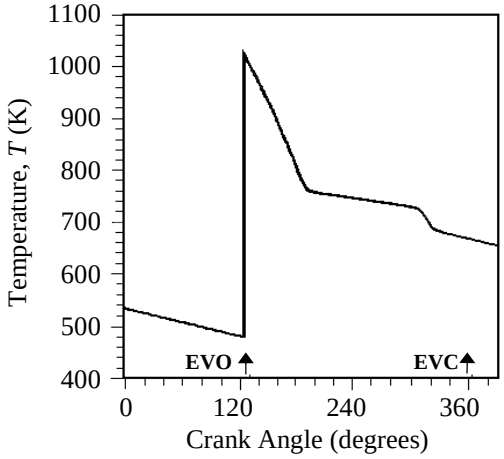


**Figure 2.6 Instantaneous Gas Temperature at the Exhaust Port between EVO and EVC (Abu Qudais, 1997)**

The effect of this transient behaviour is most marked in the exhaust manifold, as the flow from only a single cylinder is present, and flow only occurs during a single stroke of the 4 stroke cycle. In the takedown pipe the flow from the four cylinders is combined (out of phase), so a more even velocity occurs than in the manifold.

When attempting to measure and model exhaust flow behaviour it is often impractical to try to replicate the instantaneous flow properties. Extremely fast data logging rates and very small simulation time steps would be required to

capture the behaviour. If long time periods relative to the duration of the exhaust stroke are to be considered, this becomes computationally very expensive. Time averaged properties can be used to model the flow, but the instantaneous behaviour must be considered when correlations to model the flow are chosen. The most notable of these is the Nusselt correlation for convective heat transfer. The Reynolds number for the averaged flow velocity will not be a representative indication of the turbulence caused by the cyclic flow. So called 'Enhanced Turbulence' models must therefore be applied (Meisner and Sorenson, 1986), as will be discussed in Section 2.3.2.

### 2.3.2 Single Phase Heat Transfer

The single phase heat transfer modes to be considered are forced convection from the gas to the wall or the liquid film (if present), external convection from the outer surface of the walls to the surroundings, conduction of heat in the pipe wall and internal and external radiation effects. An energy balance for these heat transfer modes for a section *dx* of the exhaust pipe wall is shown in Figure 2.7.

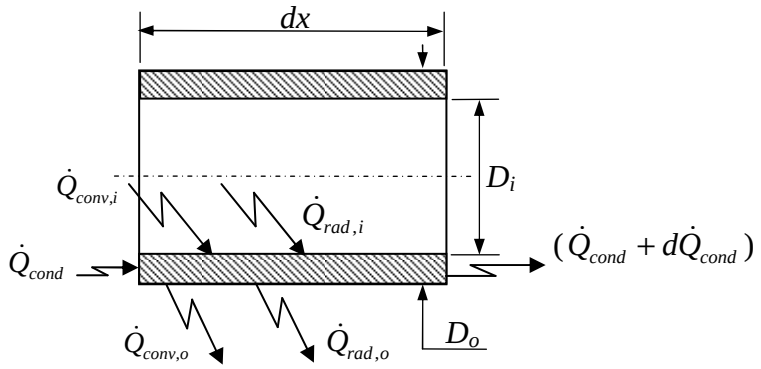


**Figure 2.7 Energy Balance on an Exhaust Pipe Wall Section**

#### 2.3.2.1 Convection

Internal forced convection heat transfer occurs from the hot gas to the cold wall in the absence of a liquid layer.

$$\dot{Q}_{conv,i} = h_c A_{w,i}(T_g - T_w) \qquad 2.6$$

with $h_c = \frac{\mathrm{Nu}k}{D_i}$ (where k is the thermal conductivity of the gas) and $A_{w,i} = \pi D_i dx$.

Nusselt correlations for forced convection in a pipe are used. The mass flow rate of the gas varies, so both laminar and turbulent flow conditions are considered. For laminar flow (Re < 2300), an average of the constant heat flux and constant wall temperature modes in a pipe is taken (Mills, 1995):

$$\mathrm{Nu} = (3.66 + 4.36)/2 = 4.0 \qquad 2.7$$

For turbulent flow (Re > 2300) a simple power law formula (Mills, 1995) is used:

$$\mathrm{Nu} = 0.023\,\mathrm{Re}_D^{\,0.8}\,\mathrm{Pr}^{0.4} \qquad 2.8$$

As discussed in Section 2.3.1, the pulsating flow occurring in the exhaust manifold due to the four stroke cycle is more turbulent than expected for a steady flow of the same bulk flow rate, resulting in an increased heat transfer rate in the manifold. Many correlations for the Nusselt number in exhaust gas flow are available in the literature. Most of these are empirically derived from experimental data specific to a single engine setup. A widely referenced example of a Nusselt correlation for the convective heat transfer in a real exhaust manifold is that of Meisner and Sorenson (1986), given as:

$$\mathrm{Nu} = 0.0774\,\mathrm{Re}_D^{0.769} \qquad 2.9$$

The above correlation concurs with that suggested by Depcik and Assanis (2002), who derived a general correlation for the Nusselt number from the theory of pulse combustion and correlated it to range of experimental data with the result:

$$\mathrm{Nu} = 0.07\,\mathrm{Re}_D^{0.75} \qquad 2.10$$

Another method of accounting for the highly turbulent conditions is the use of a Convective Augmentation Factor (*CAF*) (Kandylas and Stamatelos, 1999), also called a turbulence enhancement factor (*Fe*) (Cho *et al.*, 1997). This factor is used to calculate the effective Nusselt correlation for the real flow conditions:

$$\mathrm{Nu}_{effective} = CAF \cdot \mathrm{Nu}_{theoretical} \qquad 2.11$$

The *CAF* also accounts for the heat transfer effects of pipe bends and other physical features that are lost when using simplified straight pipe models and can be applied to the other parts of the exhaust system (Wendland, 1993). The magnitude of this enhancement factor will vary in each section of the exhaust system and is specific to a particular engine system. In this research the Nusselt correlation given in Equation 2.9 will be used in combination with a *CAF* for the manifold.

If a liquid film is present in the pipe (see Figure 2.8), it is assumed that the convection from the gas to the liquid occurs in the same manner as from the gas to the wall.

$$\dot{Q}_{conv,i} = h_c A_{w,i}(T_g - T_L) \qquad 2.12$$

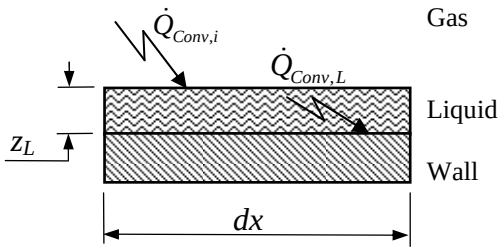


**Figure 2.8 Convective Heat Transfer between the Gas Mixture, Liquid Layer and Wall**

The additional heat transfer from the liquid to the wall must be included. For a thin film in contact with the wall heat transfer to the wall is approximated by means of the conduction thermal resistance of the film (Mills, 1995):

$$h_{c,L} = \frac{k_L}{z_L} \qquad 2.13$$

where $z_L$ is the thickness of the liquid film. This gives:

$$\dot{Q}_{conv,L} = h_{c,L} A_{w,i} (T_L - T_w) \qquad 2.14$$

Convective heat transfer on the outside of the pipe is accounted for using a heat transfer co-efficient of $h_{c,o}$ = 15 W/m$^2$K for natural convection (Batty and Folkman, 1983). The external convection is then:

$$\dot{Q}_{conv,o} = h_{c,o} A_{w,o} (T_w - T_{amb}) \qquad 2.15$$

where $A_{w,o} = \pi D_o dx$. This was deemed appropriate as experimental testing was performed in a closed engine test cell with no fans cooling the system.

#### 2.3.2.2 Conduction

Axial and radial conduction occur in the pipe wall. As the wall is thin and has a high thermal conductivity, a constant wall temperature in the radial direction is assumed. The axial conduction along the pipe is modelled using the unsteady heat conduction equation for one dimension:

$$d\dot{Q}_{Cond} = -k_w A_{cs} \frac{d^2 T_w}{dx^2} dx \qquad 2.16$$

where $A_{cs} = \frac{\pi\left(D_o^2 - D_i^2\right)}{4}$ and $k_w$ is the thermal conductivity of the wall.

#### 2.3.2.3 Radiation

Both internal and external radiation is accounted for. Radiation from the outside surface of the pipe to the environment is given by:

$$\dot{Q}_{rad,o} = \varepsilon_w \sigma A_{w,o} (T_w^4 - T_{amb}^4) \qquad 2.17$$

where $\varepsilon_w$ is the emissivity of the pipe wall.

The exhaust gases contain significant amounts of $CO_2$ and $H_2O$, both of which have strong radiation absorption properties. To evaluate the radiation heat transfer inside the pipe from the gas to the wall it is assumed that conditions of an isothermal non-grey gas in a single surfaced black enclosure hold. The governing equation for radiation from the gas to the wall under these conditions is given by Mills (1995) as:

$$\dot{Q}_{rad,i} = \alpha_g \sigma A_{w,i} T_w^4 - \varepsilon_g \sigma A_{w,i} T_g^4 \qquad 2.18$$

For a generalised combustion products composition at atmospheric pressure RAD3 (Mills, 2008) is used to estimate the emissivity and absorbtivity of the gas as $\varepsilon_g = 0.046$ and $\alpha_g = 0.061$ respectively.

### 2.3.3 Moisture Behaviour

This water produced during the combustion processes remains in the gaseous state in the high temperature conditions of the cylinder. As the exhaust valve opens the gas undergoes cooling due to expansion, followed by further cooling as the gas comes into contact with the cold walls of the exhaust system. These cooling processes give rise to the possibility of condensation occurring in either a *homogeneous* or *heterogeneous* manner.

#### 2.3.3.1 Homogeneous Condensation

The first mode of condensation to be considered is the *homogeneous* formation of liquid droplets in the gas flow due to the expansion cooling, and is independent of pipe wall temperature. To assess the likelihood that this type of condensation will occur, the following calculation is performed.

If the exhaust blow-down is considered to be an isentropic expansion (Ferguson and Kirkpatric, 2001) and the exhaust gas behaves as an ideal gas, the temperature to which the gas cools can be calculated using the relationship (Çengel and Boles, 2002):

$$\frac{T_2}{T_1} = \left( \frac{P_2}{P_1} \right)^{\left( \frac{\gamma - 1}{\gamma} \right)} \qquad 2.19$$

Typical values for engine operation are $T_1 = 1600$ K (cylinder temperature), $P_1 = 245$ kPa (cylinder pressure) and $\gamma = 1.3$ for exhaust gasses (Ferguson and Kirkpatrick, 2001). Assuming the gas expands to atmospheric pressure the new temperature is:

$$T_2 = T_1 \left( \frac{P_2}{P_1} \right)^{\left( \frac{\gamma - 1}{\gamma} \right)} = 1600 \left( \frac{100}{245} \right)^{\left( \frac{1.3 - 1}{1.3} \right)} = 1300 \text{ K}$$

The partial pressure of the water vapour at the new pressure is calculated from the vapour mass fraction, $X_v^m = 0.09$ kg $H_20$/kg dry gas, which results in a vapour

mole fraction of $y_v = 0.14$ (as shown in Appendix B1.2, for the experimental results of this research). The partial pressure of the vapour is then:

$$P_v = y_v P_2 = (0.14)(100) = 14 \text{ kPa} \quad 2.20$$

The saturated temperature for water vapour at $P_v$ = 14 kPa is 326 K (Çengel and Boles, 2002), which is much lower than the temperature of the vapour. It is therefore concluded that homogenous condensation is not likely to occur due to the initial expansion of the gas as it leaves the cylinder.

As the gas moves through the system it is further cooled by heat transfer to the pipe walls. The possibility of homogeneous condensation occurring in the downstream sections of the pipe exists if the gas temperature drops below the saturated temperature. As it is seen from experimental measurements (Clarkson and Benjamin, 2005) that temperatures below 326 K do occur in the catalytic converter, homogeneous condensation must be accounted for.

#### 2.3.3.2 Heterogeneous Condensation

The second mode of condensation considered is *heterogeneous* condensation, which is the condensation directly onto the pipe wall. The analogy between heat and mass transfer is used to model the rate of mass transfer at a liquid gas interface, in a moving medium. This mass transfer rate is given by (Çengel, 2003):

$$\dot{m}_{evap} = h_{mt} A_s \left( \rho_{v,s} - \rho_{v,\infty} \right) \quad 2.21$$

The subscript '*s*' refers to the liquid surface, and the subscript '$\infty$' refers to the bulk of the vapour. The mass transfer is driven by the density gradient between the vapour immediately at the liquid surface, which is assumed to be saturated at the liquid temperature, and the bulk of the vapour. If the vapour is assumed to be an ideal gas, Equation 2.21 can be converted (by substitution of the ideal gas equation) to:

$$\dot{m}_{evap} = \frac{h_{mt} A_s}{R_v} \left( \frac{P_{v,s}}{T_s} - \frac{P_{v,\infty}}{T_\infty} \right) \quad 2.22$$

where $P_{v,s}$ and $P_{v,\infty}$ are the partial pressures of the vapour at the liquid surface and in the bulk gas, respectively, and $h_{mt} = \frac{\text{Sh} D_{AB}}{D}$.

Using the heat and mass transfer analogy the Sherwood number Sh is evaluated in an equivalent manner to the Nusselt number for flow in a circular pipe.

For laminar flow (Re < 2300): $\text{Sh} = 4.012$ 2.23

For turbulent flow (Re > 2300): $\text{Sh} = 0.023 \text{Re}^{0.8} Sc^{0.4}$ 2.24

The diffusivity $D_{AB}$ of gas species $A$ in gas species $B$ is approximated as that of water in air (Çengel, 2003):

$$D_{AB} = 1.87 \times 10^{-7} \frac{T^{2.072}}{P} \qquad 2.25$$

where $T$ is the temperature in Kelvin and $P$ is the gas mixture pressure in atmospheres. A positive value for the mass transfer in Equation 2.21 indicates evaporation, while a negative value indicates condensation. Thus for condensation to occur the liquid temperature must be low enough for the surface saturated vapour pressure to be small in comparison to the bulk vapour pressure. If it is assumed that for a thin liquid layer the liquid temperature is close to the wall temperature, the surface vapour pressure is estimated as the saturated pressure at the wall temperature. Using the example bulk values from Section 2.3.3.1 and estimating a wall temperature as $T_s$ = 20 °C, with a corresponding saturated pressure $P_{v,s}$ = 2.339 kPa (Çengel and Boles, 2002) the gradient term is evaluated as follows:

$$\left( \frac{P_{v,s}}{T_s} - \frac{P_{v,\infty}}{T_\infty} \right) = \left( \frac{2339}{293} - \frac{14000}{1300} \right) = -2.8 < 0$$

It is therefore reasonable to assume that heterogeneous condensation is possible while the wall is cold and a sufficiently large bulk vapour pressure is maintained.

#### 2.3.3.3 Entrainment and Deposition

In two-phase flows it is also observed that liquid droplets move from the liquid layer into the bulk gas (entrainment) and from the bulk gas back into the liquid layer (deposition) (Carey, 1992).

The process of entrainment is hard to quantify but in annular flow models it has been determined that the dominant mode of entrainment is the undercutting of downward moving waves by an upward moving gas flow in a vertical pipe (Whalley, 1987). This undercutting causes the wave to form a *filament* which then breaks up into droplets in the flow. As this vertical counter flow situation is not applicable to the conditions in the exhaust system, and as there is expected to be only a small amount of liquid forming in the pipe, these entrainment effects will not be considered.

The process of deposition of droplets into the liquid layer is dependent on various factors, including the size of the droplets (Whalley, 1987). The formation of the droplets by nucleation and droplet growth by homogeneous condensation are complex processes which have been modelled by researchers such as Kelleners (2003). However, the inclusion of a comprehensive model of these processes in this study is considered beyond the scope of the research at this stage. A simplified model will be applied, in which it is assumed that if oversaturated conditions exist in the gas mixture, the excess vapour will form droplets by homogenous condensation and these droplets will collect on the pipe walls.

### 2.3.4 Friction and Momentum

The frictional effects in the exhaust flow will vary according to the amount of liquid present. In the simplest case of no liquid present, the exhaust gases are assumed to behave as a Newtonian fluid, for which the shear stress $\tau$ is defined as (Potter and Wiggert, 2002):

$$\tau = \mu \frac{\partial v}{\partial y} \qquad 2.26$$

where $\mu$ is the viscosity of the gas mixture, $v$ is the velocity in the direction of flow and $y$ is the distance from the wall. The shear stress in the gas at the wall is of most interest and can be expressed as (Whalley, 1987):

$$\tau_{gw} = \frac{1}{2} C_{gw} \rho v_g^{\,2} \qquad 2.27$$

The coefficient of friction $C_{gw}$ between the gas and the wall is correlated according to the bulk flow rate.

If Re < 1 $\quad C_{gw} = 16$

If 1 < Re < 1181 $\quad C_{gw} = \dfrac{16}{\mathrm{Re}}$

If Re >1181 $\quad C_{gw} = 0.079\,\mathrm{Re}^{-0.25}$ (Whalley, 1987) 2.28

The transition Reynolds number of Re = 1181 is chosen for the purposes of continuity in the value of the coefficient of friction. This is the projected point of intersection between the coefficient of friction curves for laminar flow and turbulent flow in a smooth pipe on the Moody diagram (Potter and Wiggert, 2002).

If a liquid film is present on the wall, the friction at the gas-liquid interface as well as that at the wall must be accounted for. According to Wallis (1970) the value of the coefficient of friction at the gas-liquid interface is given by:

$$C_{gL} = C_{gw}\left(1 + 360 \frac{z_L}{D_i}\right) \qquad 2.29$$

with $C_{gw}$ as before, $z_L$ the thickness of the liquid film and $D_i$ the pipe inside diameter. This reverts automatically to the dry gas coefficient of friction as the film becomes negligibly thin. The interfacial shear stress is now (Wallis, 1970):

$$\tau_{gL} = \frac{1}{2} C_{gL} \rho_g v_g^{\,2} \qquad 2.30$$

The liquid is assumed to be evenly distributed over the pipe wall. This thin annular liquid layer is modelled as flow over a flat plate. It is assumed that the liquid behaves in the manner of the viscous sub-layer in boundary layer flow

theory (White, 1991). In this region the flow is dominated by viscous shear, turbulence is damped out and the velocity profile is linear, as shown in Figure 2.9.

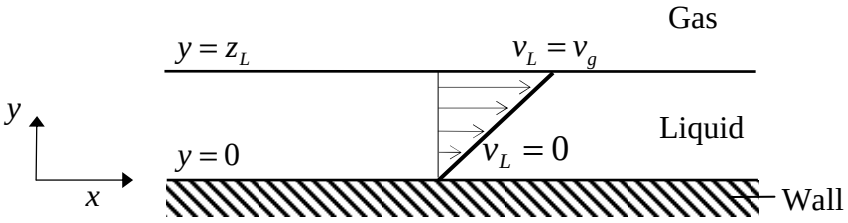


**Figure 2.9 Velocity Profile in a Newtonian Boundary Layer**

The shear stress in the liquid at the wall is:

$$\tau_{Lw} = \mu_L \left. \frac{\partial v_L}{\partial y} \right|_{y=0} \qquad 2.31$$

The condition of no-slip at the wall and at the liquid-gas interface is used to evaluate Equation 2.31. For a linear velocity profile the no-slip boundary condition (indicated in Figure 2.9) results in a liquid-wall shear stress as follows:

$$\tau_{Lw} = \mu_L \frac{v_g - 0}{z_L - 0} = \mu_L \frac{v_g}{z_L} \qquad 2.32$$

When modelling the pressure losses and momentum behaviour of the flow the transfer of mass across the liquid-gas interface during condensation or evaporation must also be considered. The effect of this mass transfer on the shear forces at the interface will not be included in the model, but the momentum transfer associated with the axial direction flow of vapour moving between the liquid and the bulk gas is included. The method of accounting for these momentum effects is discussed in Section 3.3.2, where the equations for the conservation of momentum for the gas and liquid layer are formulated.

The preceding theory can now be used to construct a mathematical model of the exhaust system so that the numerical solution algorithm can be formulated.

# 3 Mathematical Modelling

The exhaust system is simulated by means of a one dimensional, transient numerical model. The primary desired outputs of the model are the transient temperatures of the gas mixture, liquid film (if present) and pipe wall from start-up to the point when catalytic converter light off is be expected. The amount, position and duration of any liquid that forms must also be predicted. A simplified geometry is used and a number of assumptions are made in order to formulate the conservation equations of mass, energy and momentum for the system.

## 3.1 Geometry

The hot-end of an exhaust system consists of a manifold, with four pipes for gas flow, followed by a takedown pipe with either a 2-into-1 pipe or a single pipe. The gas flow therefore follows various flow paths during the four stroke cycle. For the one dimensional model this geometry is simplified to a single, straight pipe representing one continuous flow path from exhaust port to the exit of the catalytic converter. The flow path through a schematic representation of the exhaust system is shown in Figure 3.1.

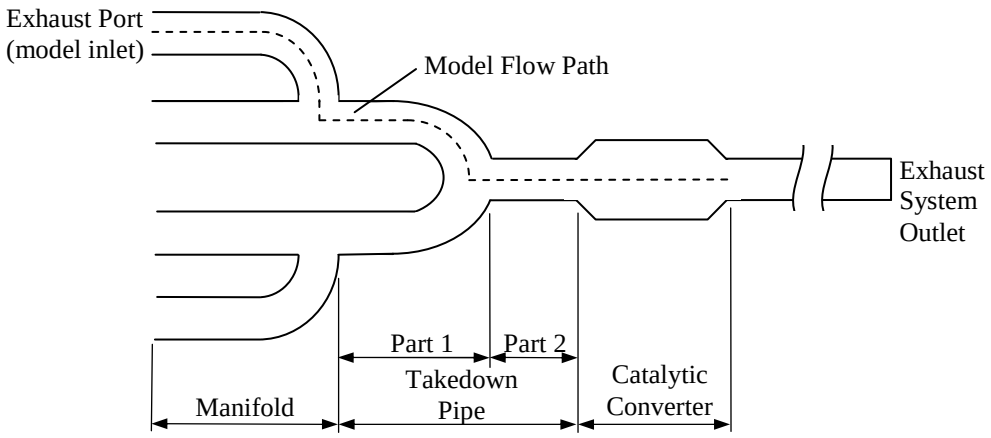


**Figure 3.1 Exhaust System with Model Flow Path**

The straight pipe is divided into sections, as shown in Figure 3.2, so that the representative physical properties, geometry and time averaged gas flow rates for each section can be accounted for.

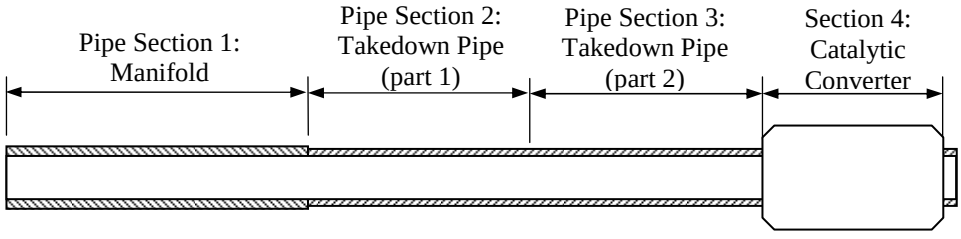


**Figure 3.2 Layout of 1D Model Exhaust System**

## 3.2 General Assumptions in the Mathematical Model

The primary simplifying assumption made in the model is that the system is one dimensional. One dimensional models representing exhaust gas flow have been used by a number of researchers in the literature, including Cho *et al*. (1997) and Siemund *et al*. (1996) and have been shown to produce satisfactory results. Due to this assumption only axial *x* direction flow effects are considered. The radial transfer of heat and mass from the gas mixture to the liquid layer and the wall is accounted for, but gas mixture velocity, temperature and concentration gradients in the radial direction are assumed to be zero. The gas mixture is thus assumed to be a fully developed (Siemund *et al*., 1996) homogenous mixture of gas and vapour, both at the same temperature. However, it is assumed that on the surface of the liquid layer or wall a film of gas mixture at the liquid/wall temperature is present.

Various assumptions are made concerning the axial gas flow. As it is impractical to either measure or model the instantaneous velocity variations, the time averaged total mass flow rate in the exhaust is used (Konstantinidis *et al*., 1997). The total flow rate was taken as equal to the sum of the experimentally measured intake air and fuel flow rates. In the manifold a quarter of the total mass flow moves through each of the 4 pipes, and in the first section of the takedown pipe the flow is divided evenly between the 2 pipes. The total mass flow moves through the second part of the takedown pipe and the catalytic converter. The gas is further assumed to be incompressible, which excludes the effect of pressure waves due to the flow velocity variations at the port from the model. This assumption was also made by Chan and Hoang (1999). Density variations occurring due to temperature and composition changes are accounted for.

The catalytic converter contains many small channels that form the honeycomb, as illustrated in Figure 3.3 (see also Figure 2.2).

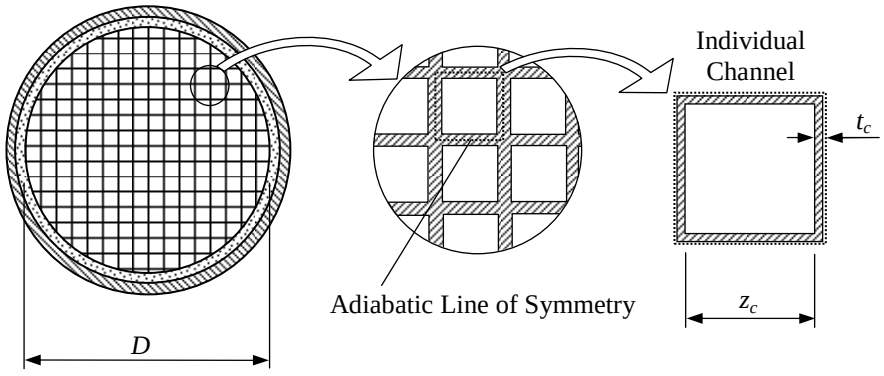


**Figure 3.3 Catalytic Converter Channel Structure**

It is assumed that the flow is evenly distributed over the channels and that the insulation surrounding the honeycomb results in negligible heat loss from the outer honeycomb surface (Koltsakis, 1997). These assumptions allow the channels to be considered identical. Heat transfer therefore also occurs identically

in each channel, with an adiabatic surface at the mid-plane of the honeycomb walls. The channel wall $t_c$ represents half the honeycomb wall thickness, and the gas mass flow in each channel represents the fraction of the total flow passing through the channel.

The liquid is assumed to deposit as an annular layer in the pipe and a layer of uniform thickness on the inner surface of the catalytic converter. The liquid temperature is assumed to be the same as that of the wall temperatures until a given mass is present (the value of this minimum 'independent' mass was chosen as the mass of liquid that would produce an even layer of 0.02 μm thickness over the inner surface of the pipe or catalytic converter). When the mass of liquid present is equal to or exceeds this minimum mass, the liquid temperature is calculated as a separate value.

With these assumptions taken in to account the mathematical modelling method can now be defined.

## 3.3 Modelling Theory

The exhaust system thermo-fluid behaviour is governed by the conservation equations for mass, energy and momentum. The theory discussed in the previous sections is used to formulate these equations for the exhaust system so that the resulting set of differential equations can be discretised and solved using a 4$^{th}$ order Runge Kutta numerical integration method.

### 3.3.1 Numerical Solution Methods

For the one dimensional model the system geometry is divided into control volumes (cv's) as shown in Figure 3.4.

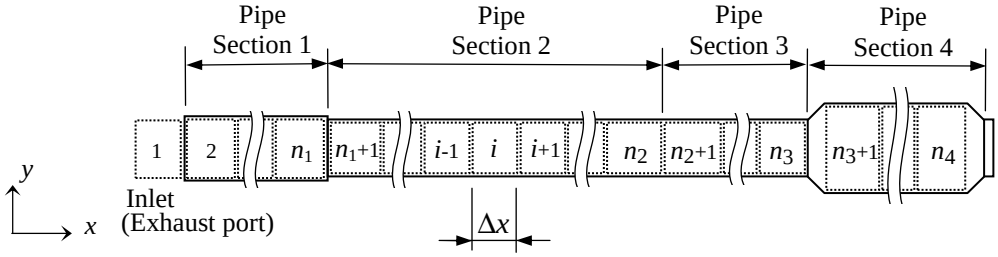


**Figure 3.4 1D Model of Exhaust System showing the Control Volumes**

Each control volume is further divided into a gas mixture, liquid layer and wall section. This division is illustrated in Figure 3.5.

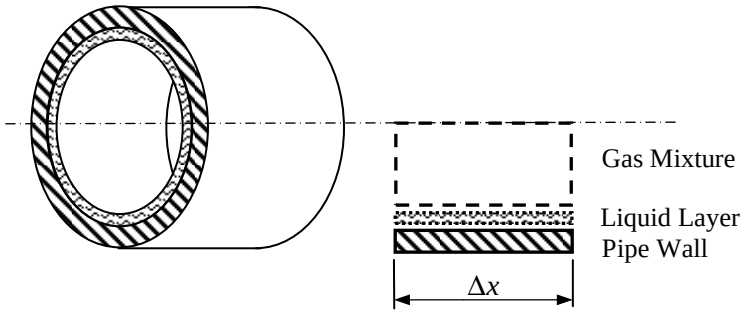


**Figure 3.5 Control Volume Sections Representing the Gas Mixture, Liquid Layer and Pipe Wall**

The gas mixture, liquid layer and wall sections of the catalytic converter are defined in the same manner as for the pipe sections, but for a single channel with wall thickness $t_c$ and an adiabatic outer surface (as in Figure 3.3). In order to avoid the very small values for mass flow and heat and mass transfer that occur in a single channel, these variables are calculated as the sum of each over all the channels. The flow dependent variables such as Reynolds and Nusselt numbers are still determined by the single channel flow and geometry.

A fourth order Runge Kutta numerical integration method was implemented in the model. The Runge Kutta method defines the differential change in a transient temperature *T* as:

$$\frac{dT}{dt} = f(t,T) \qquad 3.1$$

and the new temperature is obtained from the old value as follows (Wolfram Mathworld, 2009):

$$T_i^{\,j} = T_i^{\,j-1} + \frac{1}{6}\left(k_1 + 2k_2 + 2k_3 + k_4\right) + O\left(\Delta t^5\right) \qquad 3.2$$

with the factors $k_{1\text{-}4}$ defined as $k_1 = f(t_{j-1}, T_i^{\,j-1})\Delta t$, $k_2 = f(t_{j-1} + \frac{\Delta t}{2}, T_i^{j-1} + \frac{k_1}{2})\Delta t$, $k_3 = f(t_{j-1} + \frac{\Delta t}{2}, T_i^{j-1} + \frac{k_2}{2})\Delta t$ and $k_4 = f(t_{j-1} + \Delta t, T_i^{j-1} + k_3)\Delta t$.

In order for the Runge Kutta method to be applied to the conservation equations, these equations must be constructed in the format of Equation 3.1.

### 3.3.2 Conservation Equations

The governing equations for the flow behaviour are defined in this section. As in Section 2, the mixture of exhaust gases excluding the water vapour will be referred to as the *gas*, the water vapour as the *vapour*, and the mixture of the two as the gas *mixture*.

#### 3.3.2.1 Conservation of Mass

For the conservation of each mass species the non-steady continuity equation in one dimension is applied. The mass flows are illustrated in Figure 3.6, for the *i*th control volume. Upwind differencing (Versteeg and Malalasekera, 1995) is used for the flow.

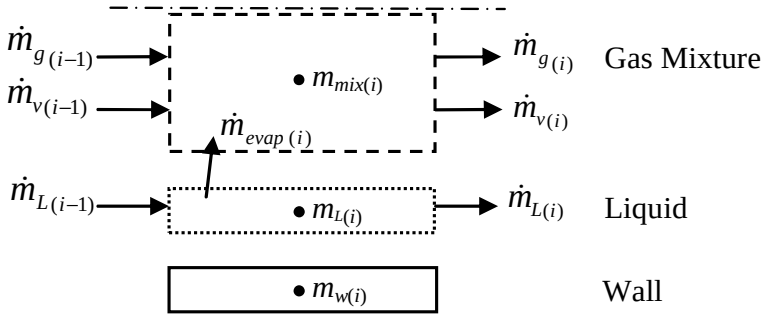


**Figure 3.6 Mass Conservation for the Gas Mixture, Liquid Layer and Wall Control Volume Sections**

The net rate of change of mass in the control volume for the gas, vapour and liquid respectively is:

$$\frac{dm_g}{dt} = \dot{m}_{g(i-1)} - \dot{m}_{g(i)} \qquad 3.3$$

$$\frac{dm_v}{dt} = \dot{m}_{v(i-1)} - \dot{m}_{v(i)} + \dot{m}_{evap(i)} \qquad 3.4$$

$$\frac{dm_L}{dt} = \dot{m}_{L(i-1)} - \dot{m}_{L(i)} - \dot{m}_{evap(i)} \qquad 3.5$$

The mass flow $\dot{m}_{evap}$ is the evaporative mass transfer given by Equation 2.22, which has a positive value when evaporation occurs and a negative value when condensation occurs.

#### 3.3.2.2 Conservation of energy

The non-steady, one dimensional energy equation is applied to each control volume (as indicated in Figure 3.7):

$$\frac{\partial}{\partial t}\left(mC_vT\right) = \sum \dot{E}_{in} - \sum \dot{E}_{out} \qquad 3.6$$

In Figure 3.7 and in the following discussions, the convective, conductive and radiation heat transfer terms are calculated as discussed in Section 2.3.

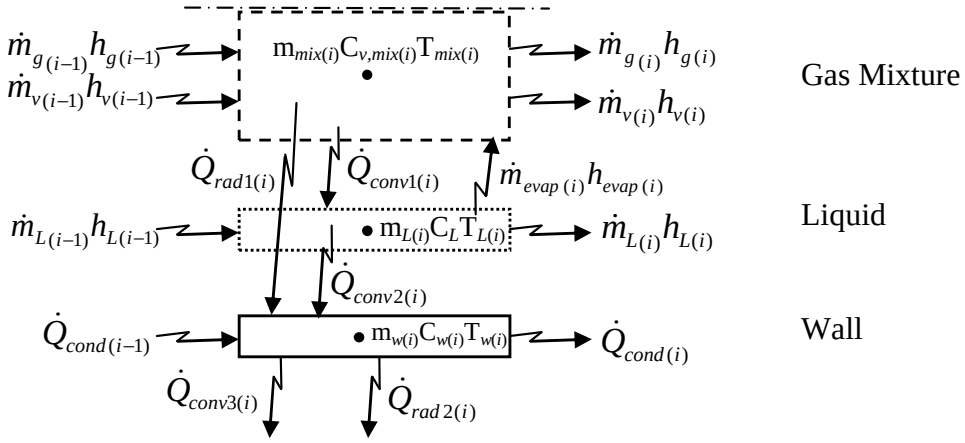


**Figure 3.7 Energy Conservation for the Gas Mixture, Liquid Layer and Wall Control Volume Sections**

Let the change in enthalpy due to the flow of the gas, vapour and liquid be defined as:

$$\frac{dH_g}{dt} = \dot{m}_{g(i-1)}h_{g(i-1)} - \dot{m}_{g(i)}h_{g(i)}$$

$$\frac{dH_v}{dt} = \dot{m}_{v(i-1)}h_{v(i-1)} - \dot{m}_{v(i)}h_{v(i)}$$

$$\frac{dH_L}{dt} = \dot{m}_{L(i-1)}h_{L(i-1)} - \dot{m}_{L(i)}h_{L(i)}$$

The energy equation for the gas mixture is now expanded to:

$$T_{mix(i)}\frac{\partial\left(m_{mix(i)}C_{v,mix(i)}\right)}{\partial t} + m_{mix(i)}C_{v,mix(i)}\frac{dT_{mix}}{dt} = \frac{dH_g}{dt} + \frac{dH_v}{dt} + \dot{m}_{evap(i)}h_{evap(i)} - \dot{Q}_{conv1(i)} - \dot{Q}_{rad1(i)}$$

where $\dot{Q}_{conv1(i)}$ is the convective heat transfer from the gas to the liquid layer (or to the wall if the liquid is absent) and $\dot{Q}_{rad1(i)}$ is the radiation from the gas directly to the wall. The value for the enthalpy associated with the mass transfer, $h_{evap(i)}$, will change according to the type of mass transfer. If heterogeneous condensation or evaporation occurs it is assumed that the mass transfer occurs between the liquid surface and the layer of saturated vapour at the surface, so $h_{evap(i)} = h_{g@T_L(i)}$. When homogeneous condensation occurs the bulk vapour condenses and the mass leaves the gas mixture as a saturated vapour at the gas mixture temperature, so $h_{evap(i)} = h_{g@Tmix(i)}$. Defining of the enthalpy associated with the mass transfer in this way causes the total enthalpy of the vapour (being the enthalpy in the condensate and the latent heat of condensation) to move into the liquid layer during condensation. The warming of the liquid due to the latent heat of

condensation is counteracted by the high rate of convection between the liquid and wall, allowing the condensation to heat the walls. During evaporation the total enthalpy leaves the liquid layer, which cools the liquid layer and counteracts the heating by convection from the gas mixture.

The gas mixture mass and specific heat can be written in terms of the gas and vapour properties:

$$m_{mix(i)}C_{v,mix} = \left(m_{g(i)} + m_{v(i)}\right)\left(\frac{m_{g(i)}C_{v,g(i)} + m_{v(i)}C_{v,v(i)}}{m_{g(i)} + m_{v(i)}}\right)$$
$$= m_{g(i)}C_{v,g(i)} + m_{v(i)}C_{v,v(i)}$$

So

$$T_{mix(i)}\frac{\partial\left(m_{g(i)}C_{v,g(i)}\right)}{\partial t} + T_{mix(i)}\frac{\partial\left(m_{v(i)}C_{v,v(i)}\right)}{\partial t} + m_{mix(i)}C_{v,mix(i)}\frac{dT_{mix}}{dt}$$
$$= \frac{dH_g}{dt} + \frac{dH_v}{dt} + \dot{m}_{evap(i)}h_{evap(i)} - \dot{Q}_{conv1(i)} - \dot{Q}_{rad1(i)}$$

If it is assumed that $C_{v,g}$ and $C_{v,v}$ do not vary significantly over the time step the energy equation can be written in terms of individual gas and vapour properties and the already defined differential changes in mass and enthalpy.

$$m_{mix(i)}C_{v,mix(i)}\frac{dT_{mix}}{dt} =$$
$$\frac{dH_g}{dt} + \frac{dH_v}{dt} - C_{v,g(i)}T_{mix(i)}\frac{dm_g}{dt} - C_{v,v(i)}T_{mix}\frac{dm_v}{dt} + \dot{m}_{evap(i)}h_{evap(i)} - \dot{Q}_{conv1(i)} - \dot{Q}_{rad1(i)}$$

The above is then solved for the differential change in gas mixture temperature in order for the Runge Kutta method to be implemented.

$$\frac{dT_{mix}}{dt} =$$
$$\frac{\frac{dH_g}{dt} + \frac{dH_v}{dt} - C_{v,g(i)}T_{mix(i)}\frac{dm_g}{dt} - C_{v,v(i)}T_{mix(i)}\frac{dm_v}{dt} + \dot{m}_{evap(i)}h_{evap(i)} - \dot{Q}_{conv1(i)} - \dot{Q}_{rad1(i)}}{m_{mix(i)}C_{v,mix(i)}} \quad 3.7$$

The energy equation for the liquid layer is obtained in a similar manner, starting by the expansion of Equation 3.6 for the heat transfer to the liquid:

$$T_{L(i)}\frac{\partial\left(m_{L(i)}C_{v,L(i)}\right)}{\partial t} + m_{L(i)}C_{v,L(i)}\frac{dT_L}{dt}$$
$$= \frac{dH_L}{dt} - \dot{m}_{evap(i)}h_{evap(i)} + \dot{Q}_{conv1(i)} - \dot{Q}_{conv2(i)}$$

where $\dot{Q}_{conv2(i)}$ is the convective heat transfer from the liquid to the wall.

Assuming that for the liquid $C_{v,L} \approx C_{p,L} = C_L$ and that this does not vary significantly over the time step the energy equation is expressed in terms of the differential mass and energy changes:

$$m_{L(i)}C_{L(i)}\frac{dT_L}{dt} = \frac{dH_L}{dt} - C_{L(i)}T_{L(i)}\frac{dm_L}{dt} - \dot{m}_{evap(i)}h_{evap(i)} + \dot{Q}_{conv1(i)} - \dot{Q}_{conv2(i)}$$

The differential temperature change for the liquid is thus given by:

$$\frac{dT_L}{dt} = \frac{\frac{dH_L}{dt} - C_{L(i)}T_{L(i)}\frac{dm_L}{dt} - \dot{m}_{evap(i)}h_{evap(i)} + \dot{Q}_{conv1(i)} - \dot{Q}_{conv2(i)}}{m_{L(i)}C_{L(i)}} \qquad 3.8$$

The conservation of energy is now applied to the wall section. Taking the mass and specific heat of the wall as constant the energy equation (Equation 3.6) expands to:

$$m_{w(i)}C_{w(i)}\frac{dT_w}{dt} = \dot{Q}_{conv2(i)} - \dot{Q}_{conv3(i)} + \dot{Q}_{rad1(i)} - \dot{Q}_{rad2(i)} + d\dot{Q}_{cond(i)}$$

with the net conductive heat transfer into the wall $d\dot{Q}_{cond(i)}$ calculated as follows:

$$\frac{d\dot{Q}_{cond}}{dx} = \dot{Q}_{cond(i-1)} - \dot{Q}_{cond(i)}$$

So

$$d\dot{Q}_{cond} = \left(\dot{Q}_{cond(i-1)} - \dot{Q}_{cond(i)}\right)dx$$

The differential temperature change for the wall section is now:

$$\frac{dT_w}{dt} = \frac{\dot{Q}_{conv2(i)} - \dot{Q}_{conv3(i)} + \dot{Q}_{rad1(i)} - \dot{Q}_{rad2(i)} + d\dot{Q}_{cond(i)}}{m_{w(i)}C_{w(i)}} \qquad 3.9$$

Equations 3.8 and 3.9 are applicable when the liquid layer is present. When the liquid mass is below the minimum mass discussed in Section 3.2, the convective heat transfer between the liquid and wall $\dot{Q}_{conv2(i)}$ falls away and the $\dot{Q}_{conv1(i)}$ is taken as the convection between the gas and wall. If condensation occurs when the liquid layer is absent, the total enthalpy in the condensing vapour is divided between the enthalpy remaining in the condensed mass of liquid, assumed to be at the temperature of the wall, and the latent heat of condensation which is assumed to move directly into the wall.

#### 3.3.2.3 Conservation of Momentum

The general conservation of momentum in one dimension is applied to both the gas mixture and liquid layer control volumes and can be expressed as (Bird *et al.*, 1960):

$$\frac{\partial(mv)}{\partial t} = \sum(\dot{m}v)_{in} - \sum(\dot{m}v)_{out} + \sum F \qquad 3.10$$

The acting forces and momentum transfer relevant to the three sections of a control volume are shown in Figure 3.8.

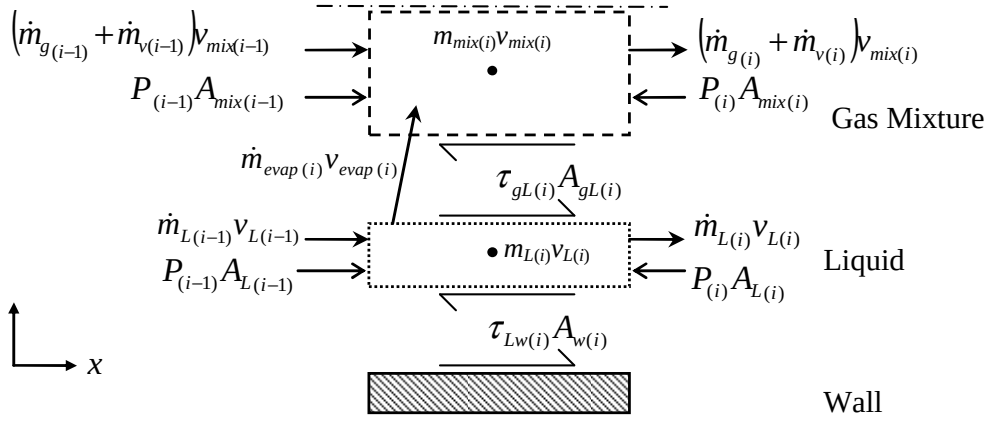


**Figure 3.8 Momentum Conservation for the Gas Mixture, Liquid Layer and Wall Control Volume Sections**

The last term in Equation 3.10 is the sum of the pressure and shear forces acting on the control volume. For the gas mixture these forces are as follows:

$$\sum F_{mix} = -\tau_{gL(i)}A_{gL(i)} + P_{(i-1)}A_{mix(i-1)} - P_{(i)}A_{mix(i)}$$

where $\tau_{gL(i)}$ is the gas-liquid interfacial shear stress, $A_{gL(i)} = \pi D_{gL}\Delta x$ is the gas-liquid interfacial surface area and $A_{mix(i-1)} = \pi D_{gL}^2 / 4$ is the gas mixture control volume cross sectional area.

The momentum equation (Equation 3.10) for the gas is expanded to:

$$v_{mix(i)}\frac{dm_{mix}}{dt} + m_{mix}\frac{dv_{mix}}{dt} = (\dot{m}_{g(i-1)} + \dot{m}_{v(i-1)})v_{mix(i-1)} - (\dot{m}_{g(i)} + \dot{m}_{v(i)})v_{mix(i)} + \dot{m}_{evap(i)}v_{evap(i)} + \sum F_{mix}$$

The momentum associated with the mass transfer depends on the direction of the mass transfer. If evaporation occurs the vapour moves into the gas flow with the axial velocity of the liquid, so $v_{evap(i)} = v_{L(i)}$. During condensation the opposite occurs, so $v_{evap(i)} = v_{mix(i)}$. The momentum associated with the radial movement of the vapour is neglected.

Using the relation $\frac{dm_{mix}}{dt} = \frac{dm_g}{dt} + \frac{dm_v}{dt}$ the above is written in terms of the differential changes in mass and vapour:

$$v_{mix(i)}\frac{dm_g}{dt}+v_{mix(i)}\frac{dm_v}{dt}+m_{mix(i)}\frac{dv_{mix}}{dt}$$
$$=\left(\dot{m}_{g(i-1)}+\dot{m}_{v(i-1)}\right)v_{mix(i-1)}-\left(\dot{m}_{g(i)}+\dot{m}_{v(i)}\right)v_{mix(i)}+\dot{m}_{evap(i)}v_{evap(i)}+\sum F_{mix}$$

This is then expanded so that it is expressed in terms of the incoming and outgoing mass flow rates of the gas and vapour.

$$v_{mix(i)}\left(\dot{m}_{g(i-1)}-\dot{m}_{g(i)}\right)+v_{mix(i)}\left(\dot{m}_{v(i-1)}-\dot{m}_{v(i)}+\dot{m}_{evap(i)}\right)+m_{mix(i)}\frac{dv_{mix}}{dt}$$
$$=\left(\dot{m}_{g(i-1)}+\dot{m}_{v(i-1)}\right)v_{mix(i-1)}-\left(\dot{m}_{g(i)}+\dot{m}_{v(i)}\right)v_{mix(i)}+\dot{m}_{evap(i)}v_{evap(i)}+\sum F_{mix}$$

By cancellation of like terms the momentum equation reduces to:

$$m_{mix(i)}\frac{dv_{mix}}{dt}$$
$$=\left(v_{mix(i-1)}-v_{mix(i)}\right)\left(\dot{m}_{g(i-1)}+\dot{m}_{v(i-1)}\right)+\dot{m}_{evap(i)}\left(v_{evap(i)}-v_{mix(i)}\right)+\sum F_{mix} \qquad 3.11$$

The desired variable to be calculated using Equation 3.11 is the total gas mixture pressure $P_{(i)}$. So $\sum F_{mix}$ is expanded and $P_{(i)}$ is made the subject of the equation, giving:

$$P_{(i)}=\frac{\left(v_{mix(i-1)}-v_{mix(i)}\right)\left(\dot{m}_{g(i-1)}+\dot{m}_{v(i-1)}\right)+\dot{m}_{evap(i)}\left(v_{evap(i)}-v_{mix}\right)-m_{mix(i)}\frac{dv_{mix}}{dt}}{A_{mix(i)}}$$
$$+\frac{-\tau_{gL(i)}A_{gL(i)}+P_{(i-1)}A_{mix(i-1)}}{A_{mix(i)}} \qquad 3.12$$

In order to solve Equation 3.12 the gas mixture velocity is required. This velocity is determined from the volumetric flow rate along the length of the system. The volumetric flow rate at the inlet of the system is a known from the experimental investigation. As the flow was assumed to be incompressible, this volumetric flow rate would remain constant along the length of each pipe section if no heat transfer or mass transfer due to phase change occurred. However, since both heat transfer and mass transfer do occur, the local volumetric flow rate, and hence velocity, in each control volume is adjusted to account for these processes. This is done by means of the continuity and ideal gas equations. The total mass of the gas mixture in each control volume is calculated by the continuity equation (Equations 3.3.and 3.4). The ideal gas equation is then used to predict the volume that this mass is expected to occupy under the conditions prevailing in the control volume, and a factor of expansion/contraction $K_{V(i)}$ is defined by the ratio:

$$K_{V(i)}=V_{ideal(i)}/V_{CV(i)} \qquad 3.13$$

where $V_{ideal(i)}$ is the volume predicted by the ideal gas equation and $V_{CV(i)}$ is the volume of the control volume. The volumetric flow rate out of the control volume is then approximated as:

$$G_{(i)} = K_{V(i)} G_{input(j)} \qquad 3.14$$

where $G_{input(j)}$ is the volumetric flow rate defined by the experimentally obtained, time dependent input function.

This method does not immediately force the mass in each control volume to be equal to the value predicted by the ideal gas equation, but instead causes the mass to strive towards this value by increasing or decreasing the local volumetric flow rate. The change in velocity with time $\frac{dv_{mix}}{dt}$ is also unknown and is approximated as the change in the known input velocity function. With the velocity and change in velocity now approximated, Equation 3.12 can be solved.

The momentum equation for the liquid control volume is used to determine the liquid film velocity. As for the gas mixture control volume the sum of the acting forces is first defined:

$$\sum F_L = \tau_{gL(i)} A_{gL(i)} - \tau_{Lw(i)} A_{w(i)} + P_{(i-1)} A_{L(i-1)} - P_{(i)} A_{L(i)}$$

where $\tau_{Lw(i)}$ is the shear force acting at the wall, $A_{w(i)} = \pi D_i \Delta x$ is the inner wall surface area and $A_{L(i)} = \pi\left(D_i^2 - D_{gL}^2\right)/4$ is the cross sectional area of the annular liquid layer. The pressure acting in the liquid is assumed to be equal to the pressure acting in the gas mixture.

For the liquid layer the momentum equation is:

$$v_{L(i)} \frac{dm_L}{dt} + m_{L(i)} \frac{dv_L}{dt} = \dot{m}_{L(i-1)} v_{L(i-1)} - \dot{m}_{L(i)} v_{L(i)} - \dot{m}_{evap(i)} v_{evap(i)} + \sum F_L$$

The above is expanded into individual incoming and outgoing liquid flow terms, like terms cancelled and solved for the differential change in liquid velocity:

$$\frac{dv_L}{dt} = \frac{\left(v_{L(i-1)} - v_{L(i)}\right)\dot{m}_{L(i-1)} - \dot{m}_{evap(i)}\left(v_{evap(i)} - v_{L(i)}\right) + \sum F_L}{m_{L(i)}} \qquad 3.15$$

The Runge Kutta solution method is applied to these conservation equations and solved by means of the numerical simulation computer algorithm.

## 3.4 Numerical Simulation of the 1D Mathematical Model

The numerical simulation used to solve the mathematical model that has been constructed from the theory in Section 3.3 is summarised diagrammatically in Section 3.4.1. The grid independence of the numerical simulation is discussed in Section 3.4.2.

### 3.4.1 Summary of Modelling Method

The solution method used in the numerical simulation is summarised diagrammatically in Figure 3.9.

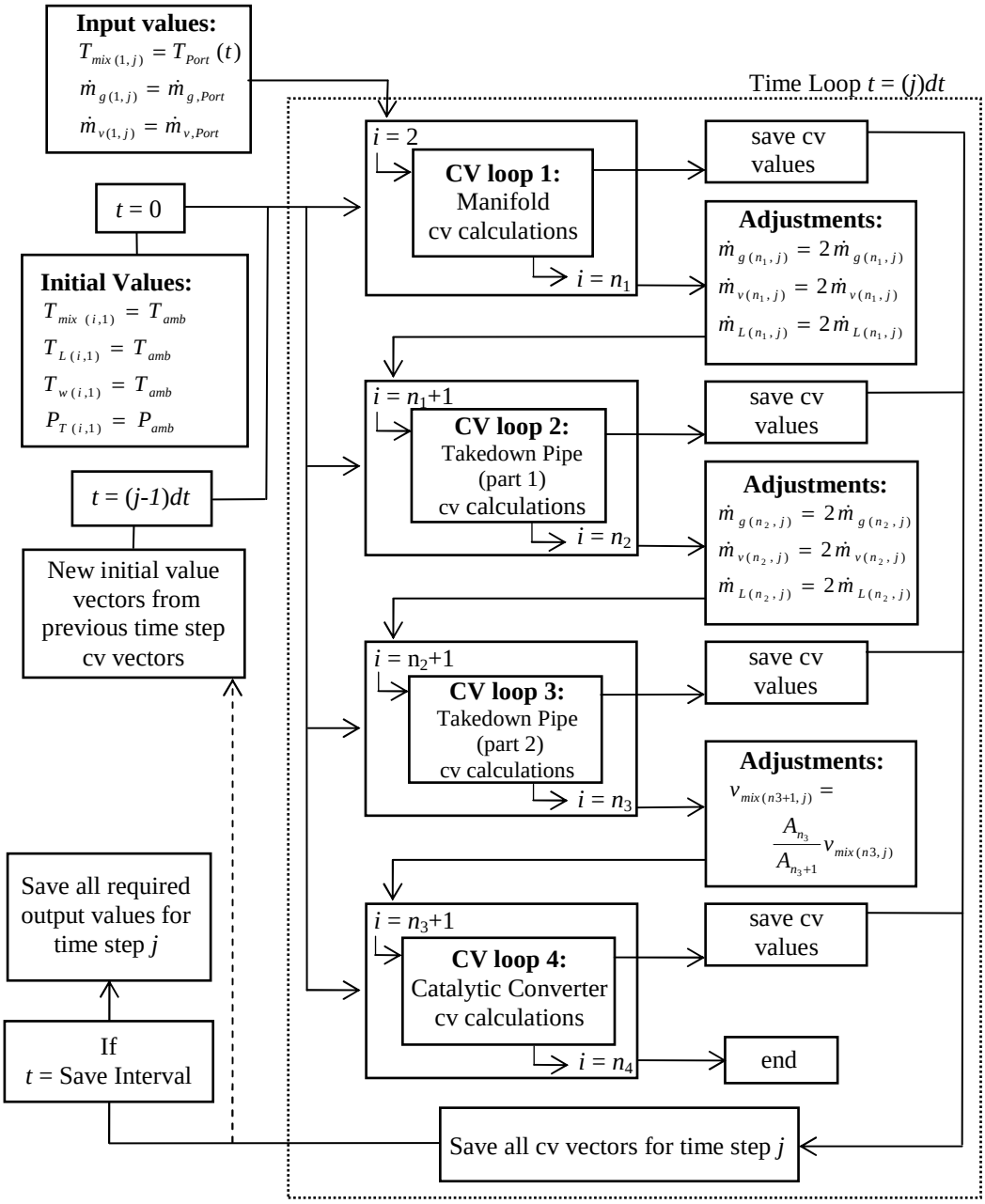


**Figure 3.9 Block Diagram of Numerical Simulation Solution Structure**

A discussion of the method and a sample calculation thereof are provided in Appendix C. (The algorithm code of the numerical simulation is supplied on the CD Addendum.)

### 3.4.2 Grid Independence

In order to ensure that grid independence was achieved in the simulation results, the time step and control volume lengths were systematically reduced and the change in the results observed. It was found that the deciding factor for the grid size was stability of the numerical simulation.

The mass transfer processes in the simulation were found to be prone to instability at any but very small time step values. A time step of $dt = 0.05 \times 10^{-3}$ s was required for stability to be maintained. A reduction in the length of the time step from $\Delta t = 0.05 \times 10^{-3}$s to $\Delta t = 0.01 \times 10^{-3}$s showed a general variation in results in the order of 1 °C. This indicates that once the stability criterion is met time step independence is also achieved.

The simulation stability was also influential in deciding the size of the control volumes used. A decrease in the control volume length from 10 mm to 5 mm produced a variation in the simulated temperatures in the order of 12 °C. This indicates that the simulation results are not fully grid independent for these control volume lengths. However, refining the grid further by decreasing the control volume length from 5 mm to 2.5 mm produced a variation in the order of 18 °C. Any reduction in the control volume length below 2.5 mm induced divergence in the simulation. This implies that the smaller control volume size produces instability induced errors, and for this reason the larger (10 mm) control volume was used.

It should be noted that the variations due to time step and control volume length reported above are indications of the difference between the results for the majority of the simulated time period. There was found to be a period of rapid two-phase mass transfer occurring in the catalytic converter section of the model that produced sharp peaks in the gas temperature. The alterations to the grid had some influence on the peaks, either by changing the maximum value or by changing the time at which the peak occurred (for example in the results obtained during the time step reduction the peak occurred approximately 5 s later with the smaller time step). The changes to the peaks did not, however, influence the results for the remainder of the time period. These peaks and the factors causing them are discussed in detail in the sections relating to the simulation results (Sections 6 and 7).

# 4 Shielded Sensor Design

As the performance of the numerical simulation is evaluated by comparison of the simulated results to experimentally measured results, and as the primary parameter for comparison is the temperature in the exhaust system, it is desirable for this temperature to be measured as accurately as possible. Engine testing performed in industry often requires very long test periods (from hours to weeks), which requires the use of robust thermocouples. This results in a trade off between the durability and the accuracy of the thermocouples and some discrepancy between the true and indicated gas temperatures is expected. For this reason a specialised sensor of improved accuracy and response time was developed.

The theory of temperature measurement in flowing gas is discussed in order to identify the expected errors associated with standard measurement methods. These errors are then mathematically modelled. Recommended methods for reducing the errors are used to design a new sensor, which is then also mathematically modelled. Using experimental results the expected errors for the two sensor types are compared and some predictions are made regarding the true gas temperatures at the exhaust port, where only the conventional thermocouples were used in the experimental investigation.

## 4.1 Standard Exhaust Temperature Measurements

Due to the high exhaust temperatures and long duration of most engine testing applications the sensors used must be robust and durable. Thermocouples with a stainless steel sheath of 3 mm outer diameter are typically used. The thermocouple is either inserted perpendicularly into the exhaust pipe wall to a distance of approximately ¾ of the pipe diameter, or bent at a right angle so that the junction faces into the gas flow, as illustrated in Figure 4.1.

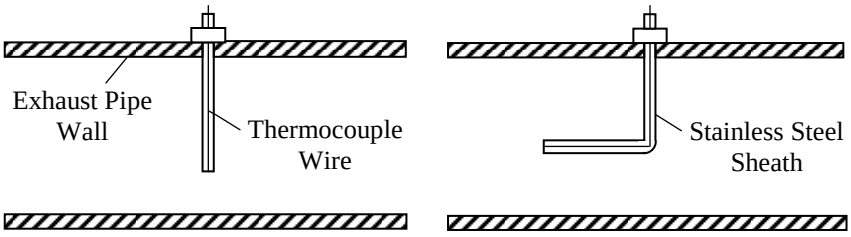


**Figure 4.1 Standard Thermocouple Installation Methods**

These methods provide reliable and repeatable results which can be usefully compared to other measurements taken in a similar manner, but do have some inherent errors which limit the accuracy of the measurements. The typical errors expected when using a thermocouple for gas measurement are the combined insertion errors, namely conduction errors, radiation errors and recovery errors (Bally *et al.*, 1993).

### 4.1.1 Sensor Error Theory

In an exhaust pipe, particularly just after engine start-up, the pipe walls are significantly colder than the gas. Conduction and radiation of heat from the thermocouple sheath to the pipe wall occur, which results in the thermocouple junction, and hence the measured temperature, being lower than the real gas temperature. In addition to this the convective heat transfer from the gas to thermocouple is not infinite, which also contributes to the measurement error.

In high velocity flow the gas is stopped by the probe and the kinetic energy lost due to the slowing of the gas is converted into heat on the upstream side of the sensor, while on the downstream side of the sensor no heat is generated. This results in the thermocouple experiencing a temperature between the higher, stagnation temperature and the static free stream temperature. The static temperature is related to the indicated temperature and the recovery error for the sensor as (Beckwith *et al*., 1993):

$$T_{static} = T_{indicated} - \frac{rV^2}{2C_p} \qquad 4.1$$

where the value of recovery factor $r$ varies between 1 and 0, is essentially constant for a specific sensor and is decided by the sensor construction. If $r$ = 0, the indicated temperature is the true static temperature, and if $r$ = 1 the indicated temperature is the stagnation temperature. However, this error is most relevant when the gas velocities are high. For the extreme case of a recovery factor of $r$ = 1, a 1 °C error is expected for a gas velocity of 40 m/s (Beckwith *et al*., 1993). As the experimentally obtained average gas velocities are all below 40 m/s, the recovery error will not be included in the analysis that follows.

In addition to the insertion errors, the thermal inertia of the sensor causes a transient error as the sensor takes time to warm up. This results in a further discrepancy between the real and measured gas temperature during the initial stage of testing.

### 4.1.2 Numerical Modelling of Standard Sensor Error

In order to quantify these errors in more detail an energy balance is performed on the thermocouple sheath. For a sheathed thermocouple with the junction welded into the sheath tip, the tip wall temperature is assumed to be the indicated temperature. The thermocouple sheath is illustrated in Figure 4.2.

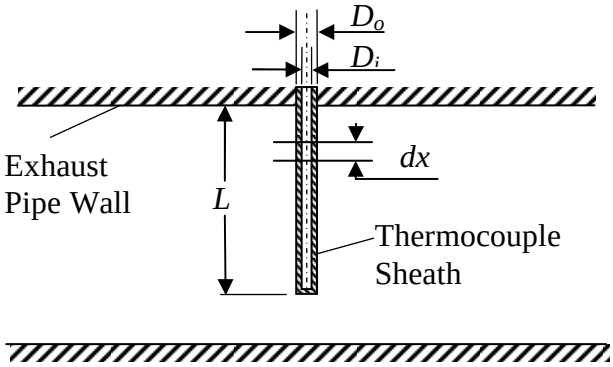


**Figure 4.2 Thermocouple Sheath Geometry**

A non-steady energy balance on an element of length *dx* along the sheath wall is shown in Figure 4.3:

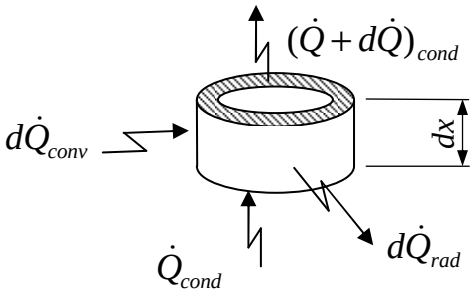


**Figure 4.3 Energy Balance on a Thermocouple Sheath Element**

The conductive, radiation and convective heat transfer rates, respectively, are given by:

$$d\dot{Q}_{cond} = -kA_{cs}\frac{d^2T_{w,s}}{dx^2}dx \qquad 4.2$$

$$d\dot{Q}_{rad} = \varepsilon\sigma\left(T_{w,s}^4 - T_{w,p}^4\right)dA_{surface} \qquad 4.3$$

$$d\dot{Q}_{conv} = h\left(T_g - T_{w,s}\right)dA_{surface} \qquad 4.4$$

where $T_{w,s}$ is the sheath wall temperature, $T_{w,p}$ is the exhaust pipe wall temperature, $T_g$ is the gas temperature, $h$ is the convective heat transfer coefficient, $\varepsilon$ is the emmisivity of the sheath, $\sigma$ is the Stefan-Boltzmann constant, $A_{cs} = \frac{\pi\left(D_o^2 - D_i^2\right)}{4}$ is the cross sectional area of the sheath and $dA_{surface} = \pi D_o dx$ is the outside surface area of the sheath element.

The unsteady energy balance for the element is then:

$$\frac{d(mC_PT)_{w,s}}{dt} = d\dot{Q}_{conv} - d\dot{Q}_{cond} - d\dot{Q}_{rad} \qquad 4.5$$

For an unchanging wall mass and constant thermal capacity this is expanded to:

$$\frac{m_{w,s}C_{Pw,s}dT_{w,s}}{dt} = h\left(T_g - T_{w,s}\right)dA_{surface} - kA_{cs}\frac{d^2T_{w,s}}{dx^2}dx - \varepsilon\sigma\left(T_{w,s}^4 - T_{w,p}^4\right)dA_{surface} \qquad 4.6$$

where $C_{Pw,s}$ and $m_{w,s}$ are the specific heat capacity and mass of the sheath element, respectively.

An explicit Euler integration method with centred spatial discretisation was used to solve this nonlinear differential equation. The thermocouple was divided into control volumes as indicated in Figure 4.4. Using this numerical method Equation 4.6 is written for each control volume from *cv*(2) to *cv*(n) as:

$$\frac{m_{w,s}C_{Pw,s}\left(T_{w,s(i,j)} - T_{w,s(i,j-1)}\right)}{\Delta t} = h\left(T_g - T_{w,s(i,j-1)}\right)A_{surface} - \frac{kA_{cs}}{\Delta x}\left(2T_{w,s(i,j-1)} - T_{w,s(i-1,j-1)} - T_{w,s(i+1,j-1)}\right) - \varepsilon\sigma\left(T_{w,s(i,j-1)}^4 - T_{w,p}^4\right)A_{surface} \qquad 4.7$$

where $A_{Surface} = \pi D_o \Delta x$, $m_{w,s} = \rho_{w,s}A_{cs}\Delta x$ and $\rho_{w,s}$ is the density of the sheath material.

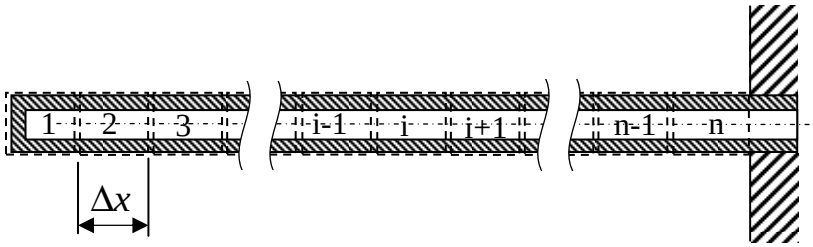


**Figure 4.4 Thermocouple Control Volumes**

For the first control volume (in which the thermocouple junction is located), the mass and area differ from the remainder of the sheath due to the tip surface, and there is no conduction into the control volume on the tip surface side. The discretised energy equation for *cv*(1) is therefore given by:

$$\frac{m_{w,s1}C_P w,s(T_{w,s(1,j)} - T_{w,s(1,j-1)})}{\Delta t} = h\left(T_g - T_{w,s(1,j-1)}\right)A_{surface1} - \frac{kA_{cs}}{\Delta x}\left(T_{w,s(1,j-1)} - T_{w,s(2,j-1)}\right) - \varepsilon\sigma\left(T_{w,s(1,j-1)}^4 - T_{w,p}^4\right)A_{surface1} \qquad 4.8$$

where $A_{Surface1} = \pi D_o \Delta x + \frac{\pi D_o^2}{4}$ and $m_{w,s1} = \rho_{w,s} A_{cs} \Delta x + \rho_{w,s}\left(\frac{\pi D_i^2}{4}\right)\Delta x$.

At the exhaust pipe wall the boundary condition $T_{w,s(n,j)} = T_{w,p}$ holds, and $T_{w,s(1,j)}$ is the temperature indicated by the thermocouple. These two values are known from the experimental investigation, so the above can be solved for the predicted real gas temperature $T_g$. The results of this analysis are discussed in Section 4.3.

## 4.2 Sensor Design to Minimise Errors

The various errors discussed in Section 4.1 can be reduced by changes to the design of the sensor, including decreasing the thermocouple diameter, increasing the insertion length and the application of radiation shields (Cavina, 2002). The effects of these changes are discussed and the new design is then mathematically modelled.

### 4.2.1 Methods of Reducing Errors

A small diameter thermocouple increases the convective heat transfer to the sensor and improves the transient response time of the sensor due to its low thermal mass. Therefore thin thermocouple wire with no sheath (other than glass fibre electrical insulation) is used.

The conduction loss is decreased by ensuring that a sufficiently long section of the thermocouple is inserted into the flow, so as to minimise the temperature gradient at the tip junction. A ratio of inserted wire length to wire diameter $(L/D) \geq 10$ is recommended for the conduction loss to be reduced enough for it to be neglected (Michalski *et al*., 1991). Radiation shields are applied to reduce the radiation heat loss to the walls. Two shields are used, as recommended by Mills (1995) for automotive exhaust applications. The basic design of the new sensor is shown in Figure 4.5 below. Manufacturing drawings of the radiation shield and support strut assembly are given in Appendix D.

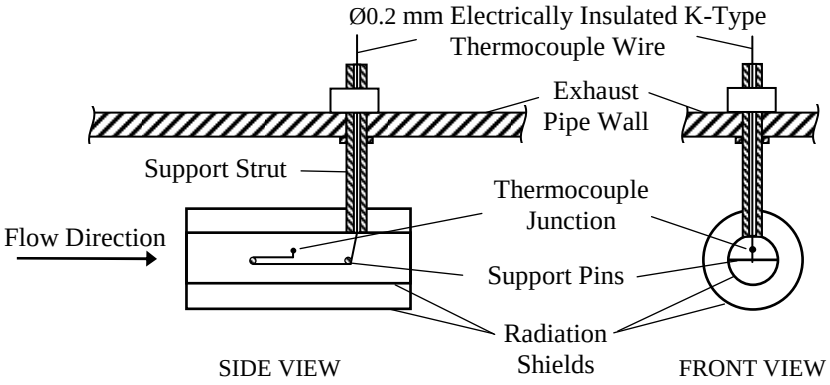


**Figure 4.5 Basic Geometry of Shielded Thermocouple**

As the thermocouple wire is very long and thin it requires structural support. In the sensor this support is provided by a pair of pins mounted horizontally in the inner shield, around which a single loop of the thermocouple wire is wound, as shown in Figure 4.5.

### 4.2.2 Numerical Modelling of the Shielded Sensor Error

To predict the total error an energy balance must be performed on the shielded sensor assembly. It is assumed that the conduction losses from the thermocouple junction are negligible due to the length of inserted wire. Convection and radiation heat transfer occur at the thermocouple junction and at each surface of the radiation shields. The energy balance is illustrated in Figure 4.6.

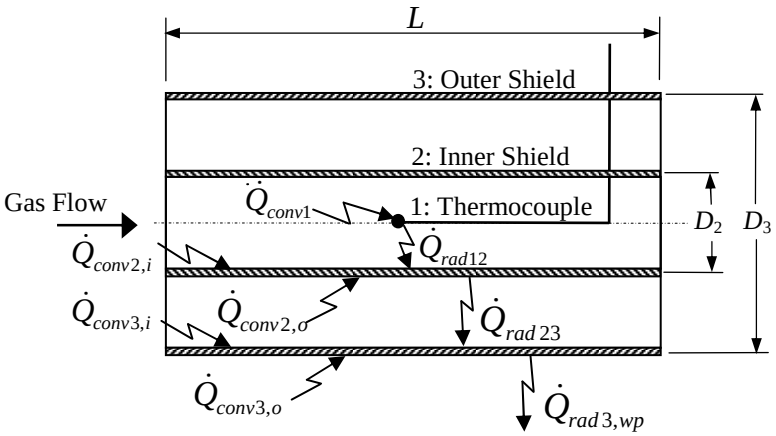


**Figure 4.6 Shielded Thermocouple Heat Transfer**

The convective heat transfer terms are determined by Nusselt correlations relevant to the geometry of the sensor. The thermocouple junction is modelled as a sphere, the inside of the inner shield is modelled as a short pipe, the space between the shields is modelled as a non-circular duct (annulus) and the outer surface of the outer shield is modelled as a flat plate. The subscripts 1, 2 and 3 refer to the thermocouple junction, the inner shield and the outer shield respectively.

For the junction, the Nusselt correlation for convective heat transfer for flow over a sphere (Incropera and DeWitt, 2002) is given by:

$$Nu_1 = 2 + \left(0.4\,\mathrm{Re}_{D1}^{0.5} + 0.06\,\mathrm{Re}_{D1}^{2/3}\right)\mathrm{Pr}\left(\frac{\mu}{\mu_s}\right) \qquad 4.9$$

where $\mu$ is the viscosity of the bulk gas and $\mu_s$ is the viscosity of the gas at the sheath temperature. The heat transfer co-efficient is then $h_1 = Nu_1 k_g / D_1$, where $k_g$ is the thermal conductivity of the gas and $D_1$ is the diameter of the thermocouple junction. The convective heat transfer at the junction is given by:

$$\dot{Q}_{conv1} = h_1 A_1 \left(T_g - T_1\right) \qquad 4.10$$

where $A_1 = \pi D_1^2$ is the surface area and $T_1$ the temperature of the junction.

As the shields are not long in comparison to their diameters, the flow is not considered to be fully developed and boundary layer Nusselt correlations (Incropera and DeWitt, 2002) are used. For the inner surface of the inner shield (flow in a short circular pipe) the Nusselt number is given by:

$$\mathrm{Nu}_{2,\mathrm{i}} = 3.66 + \frac{0.0668(D_2 / L)\mathrm{Re}_{\mathrm{D2}}\mathrm{Pr}}{1 + 0.04\left((D_2 / L)\mathrm{Re}_{\mathrm{D2}}\mathrm{Pr}\right)^{2/3}} \qquad 4.11$$

where $D_2$ is the diameter of the inner shield. As the shield wall is thin this diameter is used for both the inner and outer surface of the shield. The heat transfer co-efficient for the inner surface of the inner shield is $h_{2,i} = Nu_{2,i}k_g / D_2$ and the convective heat transfer is given by:

$$\dot{Q}_{conv2,i} = h_{2,i}A_2\left(T_g - T_2\right) \qquad 4.12$$

where $A_2 = \pi D_2 L$ is the surface area and $T_2$ the temperature of the inner shield.

The area between the shields is modelled as non-fully developed flow through a non-circular duct. The hydraulic diameter for the annulus is given by $D_{h2} = 4A_{wetted} / P_{wetted} = D_3 - D_2$. The same Nusselt correlation as that given by Equation 4.11 is used.

$$\mathrm{Nu}_{2,\mathrm{o}} = 3.66 + \frac{0.0668(D_{\mathrm{h2}} / L)\mathrm{Re}_{\mathrm{D_h}2}\mathrm{Pr}}{1 + 0.04\left((D_{\mathrm{h2}} / L)\mathrm{Re}_{\mathrm{D_h}2}\mathrm{Pr}\right)^{2/3}} \qquad 4.13$$

The heat transfer co-efficient for the outer surface of the inner shield and the inner surface of the outer shield, $h_{2,o} = Nu_{2,o}k / D_{h2}$, is used to determine the two convection terms:

$$\dot{Q}_{conv2,o} = h_{2,o}A_2\left(T_g - T_2\right) \qquad 4.14$$

$$\dot{Q}_{conv3,i} = h_{2,o}A_3\left(T_g - T_3\right) \qquad 4.15$$

where $A_3 = \pi D_3 L$ is the surface area and $T_3$ the temperature of the outer shield.

The Nusselt correlation for flow over a flat plate, for the outer surface of the outer shield, is (Incropera and DeWitt, 2002):

$$Nu_{3,o} = 0.680\,\mathrm{Re}_{L3}^{0.5}\,\mathrm{Pr}^{0.33} \qquad 4.16$$

The heat transfer co-efficient $h_{3,o} = Nu_{3,o}k / L$ is then used to determine the outer convection heat transfer:

$$Q_{Conv3,o} = h_{3,o}A_3\left(T_{gas} - T_3\right) \qquad 4.17$$

The radiation heat transfer terms must also be evaluated according to the relevant geometry. For the radiation heat transfer from the thermocouple junction to the inner shield, the junction is assumed to be a small body in comparison to the inner shield. The radiation heat transfer is then given by:

$$\dot{Q}_{rad12} = \varepsilon_1 \sigma A_1 \left(T_1^4 - T_2^4\right) \qquad 4.18$$

where $\varepsilon_1$ is the emissivity of the junction.

Ignoring the radiation from the ends of the shields, the shield to shield radiation is given by Mills (1995) as:

$$\dot{Q}_{rad23} = \frac{\varepsilon_2 A_2}{1 + \frac{\varepsilon_2 A_2}{\varepsilon_3 A_3}\left(1 - \varepsilon_3\right)} \sigma \left(T_2^4 - T_3^4\right) \qquad 4.19$$

where $\varepsilon_2$ and $\varepsilon_3$ are the emissivity values for the inner and outer shields, respectively.

The outer shield is assumed to be a small body in comparison to the exhaust pipe and the radiation heat transfer from this shield to the exhaust pipe wall is given by:

$$\dot{Q}_{rad3,wp} = \varepsilon_3 \sigma A_3 \left(T_3^4 - T_{w,p}^4\right) \qquad 4.20$$

The energy balances for the junction, inner shield and outer shield, respectively, are now performed:

$$m_1 C_{P1} \frac{dT_1}{dt} = \dot{Q}_{conv1} - \dot{Q}_{rad12} \qquad 4.21$$

$$m_2 C_{P2} \frac{dT_2}{dt} = \dot{Q}_{conv2,i} + \dot{Q}_{conv2,o} + \dot{Q}_{rad12} - \dot{Q}_{rad23} \qquad 4.22$$

$$m_3 C_{P3} \frac{dT_3}{dt} = \dot{Q}_{conv3,i} + \dot{Q}_{cond3,o} + Q_{rad23} - \dot{Q}_{rad3,wp} \qquad 4.23$$

The thermocouple temperature function $T_1(t)$ (and from this $dT_1/dt$) is known from experiment, which allows these equations to be solved simultaneously for the gas temperature. The *true* gas temperature predicted from this analysis can now be compared to that predicted from the analysis in Section 4.1.

## 4.3 Comparison of Predicted True Gas Temperatures

The solution methods laid out in Sections 4.1 and 4.2 are applied to a set of preliminary experimental results obtained using the shielded and unshielded (standard) sensor, and the true gas temperatures predicted. The temperature was measured simultaneously by both types of sensor at the same position in the

takedown pipe of the exhaust system. The measured and predicted gas temperatures for both sensors are shown in Figure 4.7.

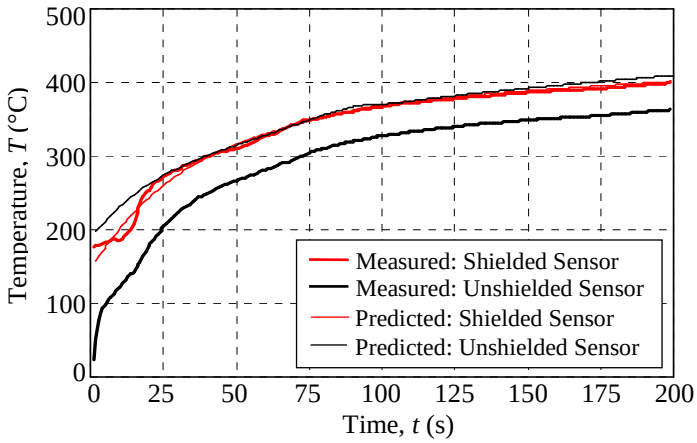


**Figure 4.7 Measured and Predicted Exhaust Gas Temperatures at the Takedown Pipe Inlet**

The difference between the measured and predicted temperatures for the unshielded thermocouple is in the order of 150 °C at the start, due to the thermal inertia of the thermocouple. At the 'steady state', when the thermocouple has had time to warm up, the discrepancy decreases to approximately 50 °C. It was found by comparison of the individual errors that this steady error is mainly due to the effect of radiation.

The gas temperature predicted from the shielded sensor measurement is almost identical to the measured value, indicating a significant reduction in the sensor error. It is also noted that the temperature predicted from the unshielded sensor measurement shows a very good correlation to the measured and predicted temperatures from the shielded sensor. From this result it is concluded that the shielded sensor indicates a temperature sufficiently close to the true gas temperature for the purposes of this research. The theory can now also be used to make predictions regarding the errors expected for measurements taken at the port, where only the unshielded sensor was present.

## 4.4 Prediction of True Exhaust Port Gas Temperatures

While the design of the shielded sensor improved the measurement accuracy, the robustness of the sensor was reduced by the use of the thin thermocouple wire. This prevented the shielded sensors from being used at the exhaust port, as the high temperatures at this position would damage them. The port gas temperature is used as an input to the numerical simulation, so the error for these measured temperatures must be estimated.

The error calculation algorithm described in Section 4.1 was applied to the port temperatures measured during the preliminary experiment of Section 4.3. The resulting predicted true port gas temperature is as shown in Figure 4.8.

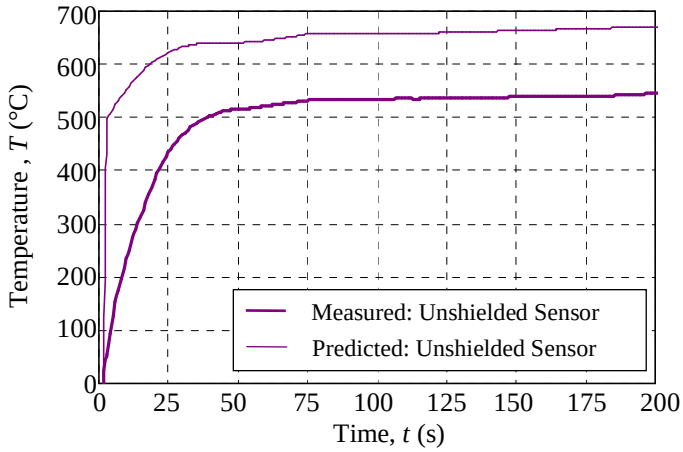


**Figure 4.8 Measured and Predicted Gas Temperatures at the Exhaust Port**

The difference between the measured and predicted temperatures at this position is in the order of 100 °C for the steady state section, and as much as 400 °C at the start of the experiment. Both errors are significantly larger than those obtained for the measurements in the takedown pipe. The increased steady state error can be attributed to the increased radiation heat transfer due to the higher gas temperatures while the wall temperatures still remain low by comparison. The initial error is due to the slow response of the unshielded sensor to the high temperature gradient at the start of the test.

Although the true gas temperature prediction algorithm used here provided good results for temperatures in the takedown section of the exhaust system, there are some characteristics of flow at the port that may not be accurately represented by the model used. The most significant of these is the highly pulsating nature of the flow exiting the port, as was discussed in the literature study (Section 2.3). The high gas speeds occurring as the port opens are not represented by the averaged flow rate model. These speeds would increase the convective heat transfer significantly, which is likely to decrease the measurement error to some degree. The assumption of negligible recovery errors would also not be valid during these pulses of high velocity, which would potentially increase the error. The effect of the higher temperatures on parameters such as the emissivity of the sensor sheath is also difficult to gauge without some means of comparison.

Because of the abovementioned effects it was decided to use both the measured port temperatures and predicted true port temperatures as input functions to the numerical simulation. A comparison was made between the numerical simulation results using each temperature function and the experimental results, in order to determine which input temperature produced a better correlation. The final decision made was to use the measured temperatures. The comparison of the results for the two inputs and the factors determining the final choice are included in the discussions (Section 7), after the experimental and numerical results have been given in Section 6.

# 5 Experimental Investigation

In order to evaluate the quality of the results obtained by the numerical simulation, an experimental investigation was undertaken. The aim of the experimental investigation was to obtain the transient gas and wall temperatures at various points in an exhaust system during cold start operation. A range of data sets was desired so more than one experimental configuration was used, as well as a range of operational speed/load combinations.

## 5.1 Experimental Setup

The experimental investigation was performed in the automotive engine test cells at Cape Advanced Engineering Pty (Ltd) (CAE), Atlantis. Testing was performed using two separate engines, a Ford RoCam and a Volkswagen Bora.

### 5.1.1 General Test Cell Equipment

The general test cell equipment remained the same for both engine configurations and the main components are indicated in Figures 5.1 and 5.2.

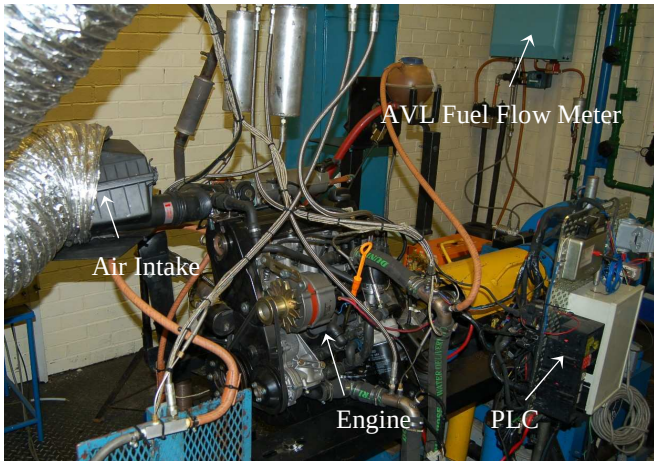


**Figure 5.1 CAE Test Cell – Side View**

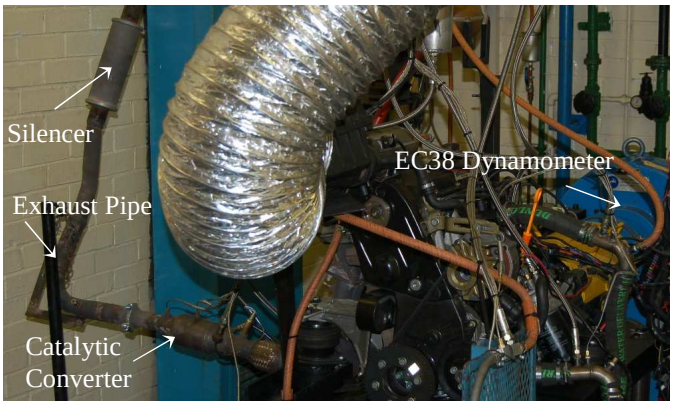


**Figure 5.2 CAE Test Cell – Front View**

The test cell consisted of an engine on a test bed, loaded by an EC38 dynamometer and controlled by the engine testing software program Engine Test Automation (ETA) developed at CAE. Various properties were measured (a list of which is provided in Appendix B) and recorded by ETA. The shielded sensors discussed in Section 4 were manufactured in the workshop of the Department of Mechanical Engineering at the University of Stellenbosch and two were installed in the takedown pipe of each test setup.

### 5.1.2 Experimental Setup 1: Bora with Catalytic Converter

This experimental setup consisted of a 1.6 L Volkswagen Bora engine. The exhaust system was composed of a standard cast iron manifold, a 2-into-1 stainless steel takedown pipe and a catalytic converter. As it was the intention of this research to model the warm-up behaviour of the monolith without the influence of exothermic reactions, an old and partly poisoned catalytic converter was used. In this way the exothermic reactions occurring in the experiment were restricted. (A discussion regarding the assumption that these reactions were negligible is provided in Section 7). The system dimensions and physical properties are listed in Appendix A.

Gas temperature measurements were taken at each of the four manifold inlets, at one of the two takedown pipe inlets and at the takedown pipe outlet. The catalytic converter temperature was measured at the midpoint (mid-bed) and outlet. The takedown pipe inlet and outlet pipe wall temperatures were also measured, using the same K-type thermocouple wire as was used in the shielded sensors, with the junction bonded to the outer surface of the pipe. The positioning of both types of sensor is shown in Figure 5.3. The thin thermocouple wire required by the design for the shielded sensor has an upper operational limit of 500 °C. The shielded sensors were therefore not used at the manifold inlets as the temperatures experienced at these points exceed the allowable temperature before the desired test duration has passed.

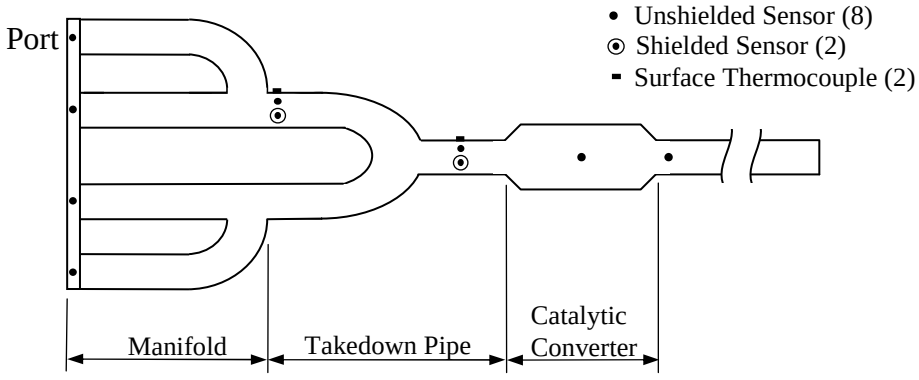


**Figure 5.3 Sensor Positions for Experimental Setup 1**

The position of the temperature sensors (and the back pressure and air/fuel ratio (lambda) sensors) on the catalytic converter section of the exhaust is shown in Figure 5.4.

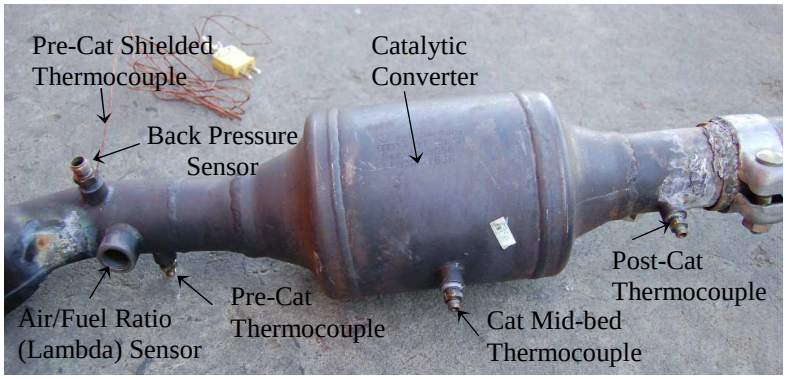


**Figure 5.4 Sensor Positioning in and around the Catalytic Converter**

### 5.1.3 Experimental Setup 2: Ford RoCam with Variable Manifolds

The engine used in this experimental setup was a 1.6 L Ford RoCam. The exhaust system had the option of three manifolds with different thermal properties, leading into a single pipe takedown pipe. It did not have a catalytic converter. Testing was performed using all three manifolds in order to obtain a range of experimental data. The manifolds were the cast iron manifold standard to the engine, a cast stainless steel manifold with the same dimensions, and a cast stainless steel manifold with reduced wall thickness. The three manifolds were made to have identical internal flow paths, in order to ensure comparable flow properties. Again the dimensions and physical properties are given in Appendix A.

Temperatures were measured at the manifold inlets and the takedown pipe inlet and outlet, as shown in Figure 5.5. The actual manifold and takedown pipe section of Experimental Setup 2 is shown in Figure 5.6, with the positions of the shielded and unshielded thermocouples indicated.

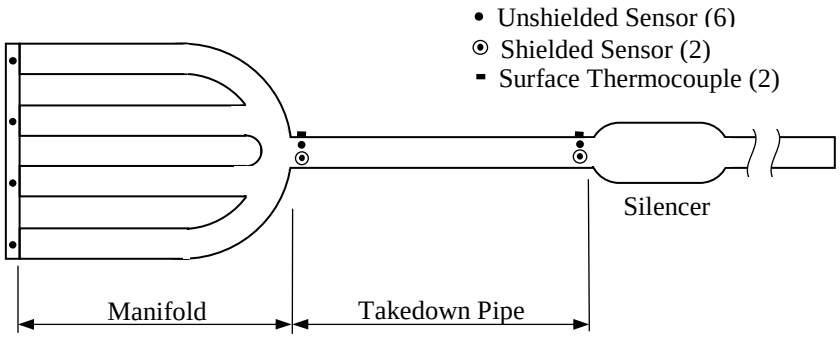


**Figure 5.5 Sensor Positions in Test Setup 2**

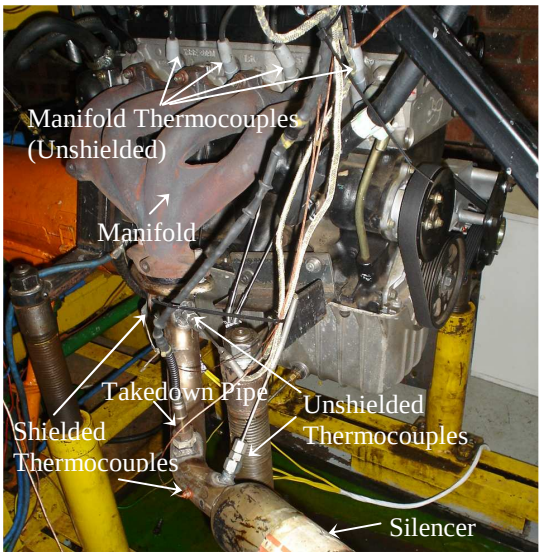


**Figure 5.6 Manifold and Takedown Pipe of Experimental Setup 2**

Even though this test setup had no catalytic converter it was useful in order to obtain data for the three available manifolds. This was of value when assessing the sensitivity of the numerical model to changes in geometry and physical properties of the exhaust system.

## 5.2 Experimental Method

The experimental investigation was divided into a preliminary phase, in which the performance of the shielded sensors (as discussed in Section 4) and the response of each of the engines were assessed, and a main testing phase from which the experimental results were generated.

### 5.2.1 Preliminary Testing

The test cell was set up by CAE technicians and an initial power-curve test was performed in order to verify that the engine performance was within its original specifications. A system calibration check procedure was also performed (the documentation of this is provided in Appendix A). During this preliminary testing it was also confirmed that the shielded sensors measured the same values as the unshielded sensors (to within 2.5 $^{o}$C) before ignition, since no insertion errors are expected when the entire system is at ambient temperature and no gas flow through the engine is occurring. The data used to compare the performance of the two types of temperature sensors in Section 4 was also generated in this preliminary testing phase.

The engine was then run at various speeds and loads in order to choose appropriate low, medium and high operating points. The chosen operating points produce a slow, medium and fast warm-up characteristic of the exhaust system and are given in Table 5.1. The same operating points were used for both experimental setups and will be referred to as the low, medium and high load cases for the remainder of this text.

**Table 5.1 Low, Medium and High Load Cases for Experimental Setups 1 and 2**

| Load Case | Engine Speed (rpm) | Engine Load (Nm) |
|---|---|---|
| Low | 1000 | ~0 (idle) |
| Medium | 1300 | 20 |
| High | 1500 | 40 |

Having set up the test cell and defined the required load cases, the main experimental investigation was performed in order to generate the results to be compared to the results of the numerical simulation.

### 5.2.2 Main Experimental Procedure

The primary considerations for the experimental investigation were that the testing had to be done with a cold engine for each test run and multiple runs had to be performed for each test configuration in order for the repeatability of the results to be assessed. This requires the individual runs of each test configuration (ie, each load case for Experimental Setup 1, as well as each load case for each manifold of Experimental Setup 2) to be comparable to each other.

In order for the individual test runs to be comparable to each other a pre-programmed test cycle was used. This cycle consisted of 5 stages:

1. Log data for 10 seconds with the engine off
2. Engine ignition
3. 3 second idle
4. Ramp up to the desired speed/load point
5. Maintain the speed/load point for the remainder of test

The total duration of a test run for Experimental Setup 1 was 120 s, as this was the time it took for the catalytic converter to reach temperatures at which the exothermic reactions would start to become significant in a real engine application. In the case of Experimental Setup 2, which had no catalytic converter, the test was run until the unshielded thermocouple at the takedown pipe outlet measured a gas temperature at which light-off would have occurred if a catalytic converter had been present, while not exceeding the safe operational temperature of the shielded thermocouples. These criteria resulted in a 270 s duration for Experimental Setup 2. The reason for the much shorter duration of the run for the first setup is that the Bora engine has been specifically designed to be used in conjunction with a catalytic converter and therefore heats up more quickly than the RoCam.

In order for a true cold start to be achieved only 3 test runs were performed per day; in the morning, at midday and in the late afternoon. A minimum of 3 hours was waited between test runs, during which time two large fans and a blower were used to cool the equipment. This proved to be sufficient time to bring the engine and exhaust system back to room temperature. (The fans and blower were not used during the testing itself.) At least three test runs were performed for each test

configuration. The large amount of data generated was then processed to obtain a single set of results for each test configuration.

## 5.3 Processing of Experimental Results

In order to obtain the final gas and wall temperature profiles for each test configuration, the data from the individual test runs of each was averaged and an error analysis was performed. These temperature profiles are the output to which the numerical simulation results are compared. The input functions for each version of the numerical simulation (corresponding to each test configuration) are also generated from the experimental results.

### 5.3.1 Error Analysis

The error analysis was performed in order to asses the repeatability and accuracy of the experimental results. Factors influencing these properties and the methods used to quantify them are discussed here.

#### 5.3.1.1 Repeatability

Although the experimental procedure was carried out in such a way as to provide as much repeatability in the data as possible (by means of the identical pre-programmed test runs discussed in Section 5.2) fluctuations in the engine response and other variables such as the ambient conditions still occur.

The engine does not respond identically in every test run. This is particularly apparent in the brief idle period just after ignition, where a significant amount of instability occurs before the engine starts running smoothly. Variations from test to test also occur due to the engine control system, which can maintain the speed and load of the engine close to, but not perfectly at, the desired operating point. Even within a single test the individual exhaust port temperatures differ from each other. This can be attributed to the engine tuning and perhaps the engine cylinders receiving different amounts of fuel.

The ambient temperature and humidity conditions also fluctuate from one test run to another. The ambient temperatures were all in the range of 17 to 25 °C, except on one particularly hot day with an ambient temperature of 31 °C. The measured relative humidity values ranged from 13% to 60%. However, the contribution of the environmental moisture in the intake air to the total vapour mass in the exhaust gasses is small (typically in the range of 10%), so these humidity fluctuations do not have a large impact on the test results.

The overall effect of these variations is evaluated by determining the probability distribution of the measured data, from which the 95% confidence interval is calculated. The full error analysis procedure is provided in the form of a sample calculation in Appendix A. The averaged values of the gas and wall temperatures are provided in Section 6, with the 95% confidence interval of each value represented by error bars on each curve.

#### 5.3.1.2 Accuracy

Deviation of the measured values from the true value of the quantity being measured occurs due to possible bias errors in the measurement system, as well as to limitations of the sensors themselves. The factors influencing the accuracy are reduced where possible.

In order to minimise any system bias errors a calibration check procedure was performed by the CAE technicians. (The documentation of this procedure is given in Appendix A.) This procedure ensured that all the test cell equipment operates from a specified initial reference condition during the testing.

The ability of the thermocouples themselves to indicate the true gas temperature in flowing gas and for a transient condition is limited by the combined insertion errors discussed in Section 4.2.1. The radiation shielded thermocouple was designed with the purpose of increasing the accuracy of the measurements by reducing these errors. The temperature correction algorithm for the unshielded sensors allowed assessment of the accuracy of these sensors to be made.

The ability of the thermocouple to accurately indicate the temperature experienced by the junction is defined by the SABS 1488 standard allowable tolerance for a K-type thermocouple, as used for this testing. This tolerance is 2.5 °C (for the range -40 to 1100 °C), which is small when compared to both the deviation in the measured data and the errors produced by the insertion errors. The temperatures of boiling water at local atmospheric pressure and an ice bath were measured as a check on the performance of the shielded sensors that were manufactured. This confirmed that these sensors measure within this required tolerance.

### 5.3.2 Definition of Inputs for the Numerical Simulation

In order for the numerical simulation to represent each of the test configurations, input functions and initial values specific to the test configuration must be determined from the experimental data.

The average ambient temperature from all the test runs of a given configuration is used as the initial value for the temperature of the whole exhaust system. This temperature is used to determine the initial mass of gas in each control volume by means of the ideal gas equation. The flow into the exhaust system is defined by time dependent input functions for the gas mass flow rate, the vapour mass flow rate and the input temperature of the gas mixture. These functions are generated by curve fits of the experimental data using the Microsoft Excel Solver function to minimise the absolute error between the curve fit function and the experimental data. The exhaust gas composition and properties are calculated by a combustion analysis using the measured air/fuel ratio.

The method used to determine these inputs is described in Appendix B, with sample calculations where relevant. The input and initial values generated for use in each simulation configuration are also listed in Appendix B.

# 6 Experimental and Numerical Results

The results of the experimental investigation and numerical simulation are now laid out and briefly discussed. In this section the general trends in the results are observed and points requiring more detailed discussion (to follow in Section 7) are identified.

## 6.1 Experimental Results

The measurements of gas and wall temperatures were taken at four positions in Experimental Setup 1 (ES1) and two positions in Experimental Setup 2 (ES2). For the sake of clarity in the discussions the temperature measurement positions are numbered as shown in Figure 6.1. The port temperature is not numbered as it is used as an input value in the numerical simulation, so there is no corresponding simulation result to which will be compared. Gas temperatures measured using the unshielded thermocouple are labelled a, those measured by the shielded thermocouple are labelled b and the wall temperatures labelled w.

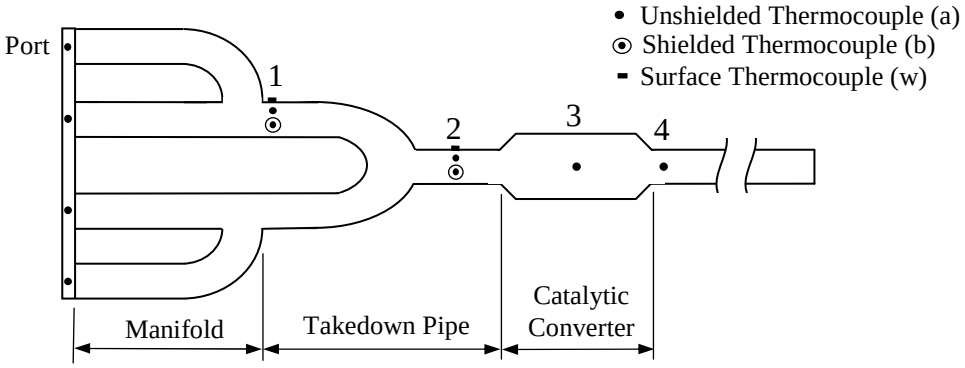


**(i) Experimental Setup 1**

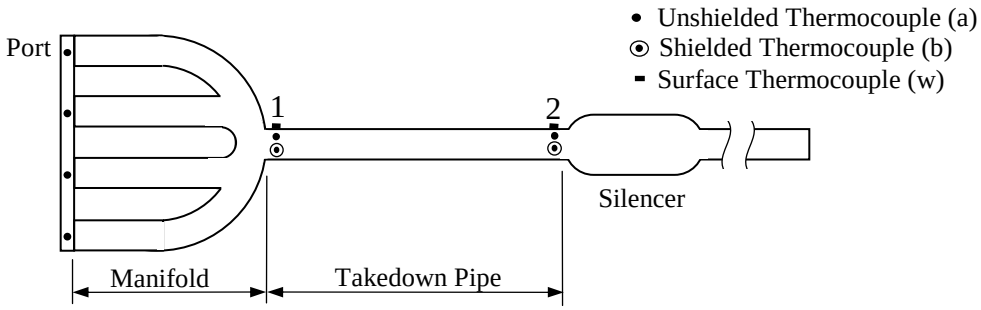


**(ii) Experimental Setup 2**

**Figure 6.1 Sensor Positions for (i) Experimental Setup 1 and (ii) Experimental Setup 2**

### 6.1.1 Experimental Setup 1

The gas temperatures for the three load cases of ES1, the Bora engine, are given in Figure 6.2. The error bars on each curve are an indication of the 95% confidence interval of the measurement, as discussed in Appendix A.

The port temperature at the low load (idle condition) is higher than those for the two higher loads of ES1. This occurs because the engine automatically retards the timing at an idle load start up in order to increase the exhaust temperature. This decreases the time it takes for the catalytic converter to light-off at idle loads. At the medium and high loads the timing is advanced again, in order to achieve greater efficiency in the engine, so the port temperatures are slightly lower.

There are fluctuations in the medium load port temperature between 20 and 80 s, and a drop in the high load port temperature at approximately 70 s. These phenomena are both associated with the engine's response to being maintained at the chosen speed/load condition. Both phenomena were closely repeated over a number of test runs (as indicated by the narrow error bars on these port temperatures). The low load result has the most regular curve, but a wider confidence interval is noted in the port and especially downstream temperatures. This is due to the fact that the idle condition is most difficult to control precisely, and therefore had lower repeatability.

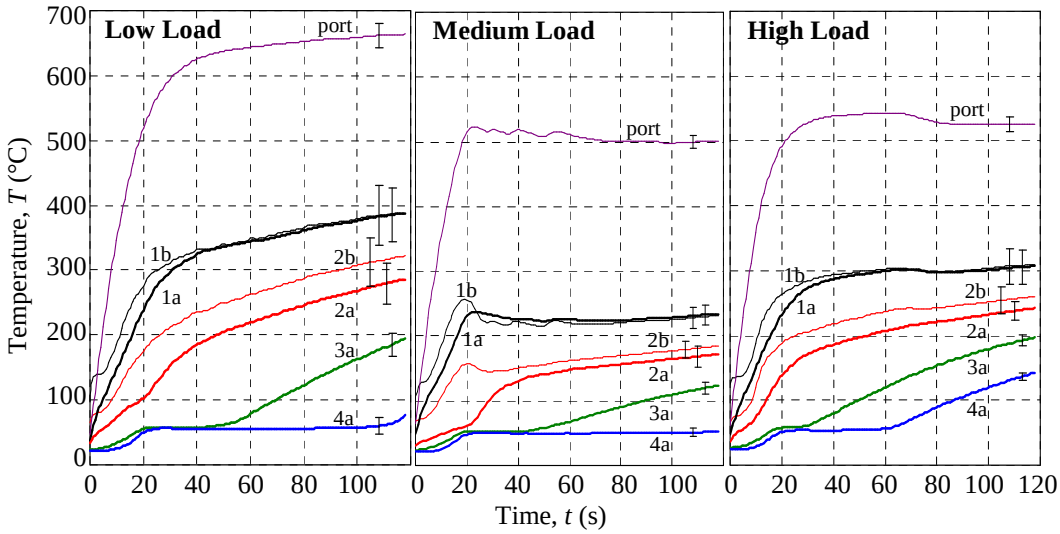


1: (a) Takedown Inlet (Unshielded Sensor), (b) Takedown Inlet (Shielded Sensor)
2: (a) Takedown Outlet (Unshielded Sensor), (b) Takedown Outlet (Shielded Sensor)
3: (a) Catalytic Converter Mid-Bed (Unshielded Sensor)
4: (a) Catalytic Converter Outlet (Unshielded Sensor)

**Figure 6.2 Gas Temperatures vs Time for Experimental Setup 1 at Low, Medium and High Loads**

The relative magnitudes of the temperatures measured at 1 and 2 for each load follow the trend of the port temperatures, being highest for the low load and lowest for the medium load. Comparing the two types of thermocouples, it is seen that the shielded thermocouple has a faster response to the early temperature rise, as expected due to its thinner wire diameter. Fluctuations in the medium load temperature at 1 are also captured by the shielded sensor. The first and largest of these fluctuations, with a peak of 250 °C at 20 s, has a higher amplitude than the corresponding peak measured in the port temperature. However, the port

temperature was measured by the less responsive unshielded sensor, so it is likely that the actual fluctuations in this value were larger than shown.

As the temperature gradient decreases (after about 40 s) the response time of the sensor becomes less influential. In this period the difference between the measurements of the two types of sensors indicates the magnitude of the combined ‘steady state’ error caused by radiation, conduction along the sensor and imperfect convection. At position 1 the two sensors measure approximately the same and at 2 maintain a fairly steady offset for each load case. The result at position 1 is unexpected, as the theory suggests that there should be an offset between the measurements at both positions. Reasons for this sensor behaviour and a general assessment of the sensor design will be discussed in more detail in Section 7.

The temperatures measured at positions 3 and 4, the catalytic converter mid-bed and outlet, exhibit the plateau that was observed by Marais (2004), Chan and Hoang (1999) and Clarkson and Benjamin (1995), on which the original hypothesis of this research is based. It is seen that the plateaux at both positions and for all three loads begin at approximately the same time (20 s), and occur at the same temperature (≈53 °C). A comparison of the plateaus at position 3 for each load shows the longest duration at the low load, and the shortest at the high load, despite the incoming gas temperatures at the low load being the highest. Once the plateau ends the temperature rises more rapidly at the low and high load conditions than for the medium load.

At position 4 the plateau lasts almost the whole duration of the test for the low and medium loads. At the high load the plateau ends after 60 s due to the combined influence of the high mass flow rates and high temperatures at this load. These results show a strong dependence on the mass flow rate of gas through the catalytic converter, which increases as the load increases and causes higher rates of convection. The retarded timing that produces the high temperatures at the low load compensates for the low mass flow rate at this load to some extent, but still does not achieve the speed of warm up that occurs due to the high temperatures and mass flow rate produced at the high load.

The wall temperatures measured at positions 1 and 2 are shown in Figure 6.3. The wall temperatures are higher at position 1, which is expected as this is closer to the exhaust port than 2. Both temperatures are higher for the low power case than for the other two cases due to the higher gas temperatures. The measured wall temperatures at both positions for the high load are slightly lower than those measured for the medium load. This is unexpectedly low for this load case. Both cases had similar ambient temperatures and no fans were used in the tests of either load case, but the high load condition consistently measured these slightly low values for all of the individual test runs.

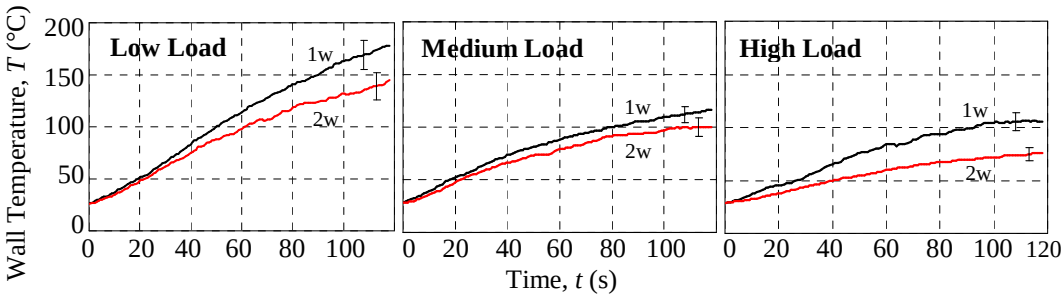


1w: Takedown Pipe Inlet Wall, 2w: Takedown Pipe Outlet Wall

**Figure 6.3 Wall Temperatures vs Time for Experimental Setup 1 at Low, Medium and High Loads**

### 6.1.2 Experimental Setup 2

The gas and wall temperatures for all three load cases for all three manifolds used in ES2 are shown together in Figure 6.4 (overleaf). The adjusted timing applied to the Bora engine at the idle condition is not applied to the RoCam, as this engine has no catalytic converter. The port temperature is therefore lowest at the low load and highest at the high load. The downstream gas and wall temperatures follow this trend and increase from the low to the high loads.

It is noted that the port temperatures for each load differed very little with the change in manifold. This is expected since the manifold should not influence the temperatures upstream of itself. Any differences between the downstream temperatures obtained using different manifolds at a given load can therefore be attributed to the manifold properties. As the manifolds have identical inner dimensions the only change experienced by the exhaust system due to the use of one manifold or another is the change in wall thermal mass.

The difference between the results for the cast iron and standard wall thickness stainless steel manifolds is minimal for both gas and wall temperatures. This indicates that the small change in thermal mass caused by the different materials is not very influential on the temperature behavior of the system. The larger reduction in thermal mass achieved by the use of the thin walled stainless steel manifold produces noticeably higher temperatures for all gas and wall measurements. The most noticeable increase is observed in the wall temperatures at the high load.

In ES2 the shielded sensors measured consistently higher gas temperatures at both measurement positions, as expected from the theory. The shielded sensors also capture the temperature fluctuations caused by the initial torque peak at ignition, which are absent from the unshielded sensor outputs, due to the slower response of the latter.

Having gained a general understanding of the behaviour of the two experimental systems, the gas and wall temperatures are now compared to the numerical simulation results.

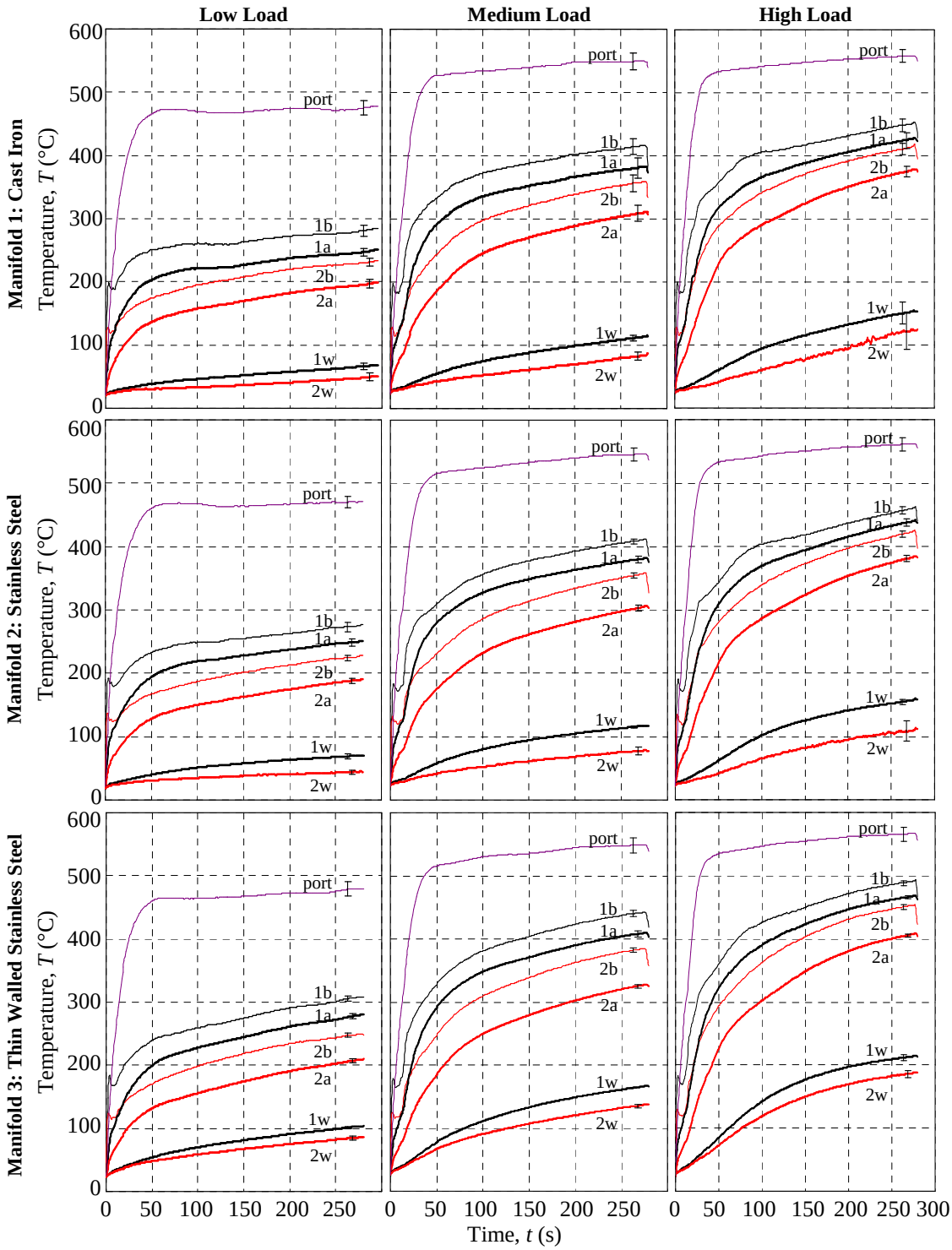


1: (a) Takedown Inlet (Unshielded Sensor), (b) Takedown Inlet (Shielded Sensor)
2: (a) Takedown Outlet (Unshielded Sensor), (b) Takedown Outlet (Shielded Sensor)
1w: Takedown Inlet Wall, 2w: Takedown Pipe Wall

**Figure 6.4 Gas and Wall Temperatures vs Time for Experimental Setup 2, All Manifolds at Low, Medium and High Loads**

## 6.2 Numerical Simulation Results

The numerical simulation was run using the experimentally generated input functions for each experimental configuration. This was done so that the experimental and numerical simulation results would be comparable in each case. The simulation results corresponding to the sensor positions are plotted alongside the experimental results in the figures that follow. The same position numbers and labels are used as in Section 6.1, with the added label 'n' indicating the numerical simulation results at each position. In addition to the comparison of the measured and simulated temperatures, the liquid mass predicted for ES1 is also shown.

### 6.2.1 Numerical Simulation Results for Experimental Setup 1

The numerical simulation results for the three load cases of ES1 are shown in Figure 6.5 (for the gas temperatures) and Figure 6.6 (for the wall temperatures). The simulation results show good correlation to the experimental results at some positions, and exhibit discrepancies at others.

Considering first the results at point 1, it is seen that for all three load cases the gas temperature is higher than the measured temperature. The difference decreases towards the end of the test period at the low load and is fairly constant at the high and medium loads after 20 s. The shapes of the simulation results at each load are similar to each other, and closely follow the shapes of the input temperature functions. It is noted that the simulation results for the medium load did not reflect the fluctuations seen in the measured temperature because the port temperature input function was a smoothed curve. (See Appendix B for the method of generating of the input temperature functions).

The simulated gas temperatures were found to be sensitive to the fluctuations in the flow rate, as taken into account by the Convective Augmentation Factor (*CAF*) defined in Section 2.3. An increase in the *CAF* causes increased heat transfer and hence a reduction in the gas temperature and a corresponding increase in wall temperature. The choice of *CAF* is decided by the trade-off between these two temperatures. The numerical results shown in Figure 6.5 and 6.6 were generated using the Nusselt correlation of Mesiner and Sorenson (Equation 2.9), in combination with a *CAF* specific to each load. The *CAF* values found to produce the best correlation were 1.1 for the low load, 1.5 for the medium load and 1.2 for the high load.

Even though this choice of *CAF* for each load resulted in slightly high gas temperatures at position 1, it is seen from Figure 6.6 that the wall temperatures are already higher than those measured. An increase in *CAF* to reduce the gas temperatures is therefore undesirable. Furthermore this choice of *CAF* produces a gas temperature at position 2 that correlates well with the experiment at all three loads. The *CAF* is a very influential parameter in the numerical simulation and the factors influencing the choice of the values will be discussed in detail in Section 7.

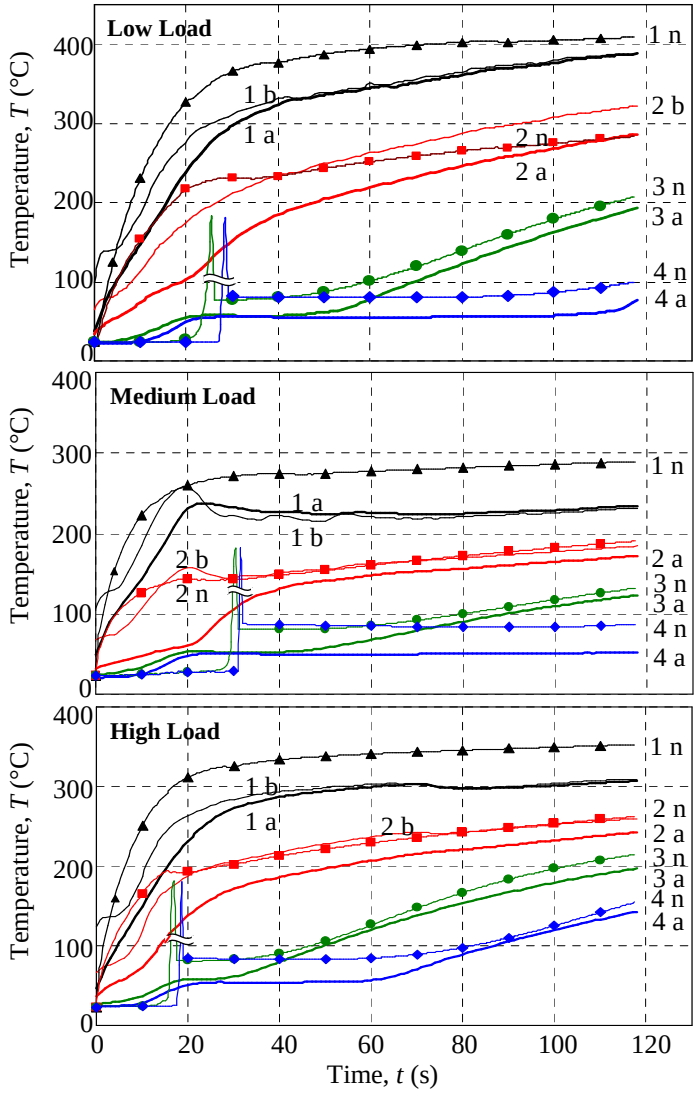


1: Takedown Inlet (a) Measured, Unshielded Sensor, (b) Measured, Shielded Sensor, (n) Simulated
2: Takedown Outlet (a) Measured, Unshielded Sensor, (b) Measured, Shielded Sensor, (n) Simulated
3: Catalytic Converter Mid-Bed (a) Measured, Unshielded Sensor, (n) Simulated
4: Catalytic Converter Outlet (a) Measured, Unshielded Sensor, (n) Simulated

**Figure 6.5 Measured and Simulated Gas Temperatures for Experimental Setup 1 at Low, Medium and High Loads**

As mentioned, the experimental and simulated gas temperatures at point 2 correlate very well. For both the medium and high loads the simulated gas temperature falls almost exactly on the experimental result from the shielded sensor (after 30 s). At the low load the gradient of the simulated temperature is slightly low, resulting in a temperature falling between the measurements from the two sensors.

Before 30 s the simulated gas temperatures show a slight initial overshoot, more noticeable at the low and high loads than at the medium load. This is the first observable effect of the moisture model in the simulations. The convection

governed heterogeneous condensation model causes a small amount of condensation (in the order of 5 to 15 mg/cm) to occur, which promotes warming of the wall. As the incoming gas temperature continues to rise, this moisture then evaporates. The evaporation causes the internal energy of the liquid mass to move out of the liquid layer and into the gas stream, which causes a slight increase in the gas temperature. Once all the moisture has evaporated the warming effect stops and the vapour rich gas moves downstream. This causes a slight drop in temperature. After this no more two-phase mass transfer occurs at position 2.

In the low load case the lower mass flow rates produce lower rates of convection, resulting in a low, smooth 'bump' in the gas temperature. At the high load the process is accelerated and a brief, slightly uneven peak is seen at 15 s. At the medium load a slight 'bump' occurs as it did for the low load, but it does not exceed the measured temperature due to the fluctuation occurring in the measured temperature at position 2.

It is noted that this moisture effect actually causes the simulation to deviate from the experimental results. This could be due to the choice of parameters used in the moisture model or due to assumptions made during the modelling of the heat transfer during mass transfer. The effect of adjusting the moisture model is discussed in more detail in Section 7. The result obtained here does indicate that the moisture effects in this section of the exhaust system are less significant than the current model predicts.

The wall temperatures at points 1 and 2 are shown in Figure 6.6. As mentioned previously in this section, the choice of *CAF* resulted in simulated temperatures that are higher than the measured values. The difference between the measured and simulated values was greatest for the high load case, and the best correlation was obtained at the medium load. The difference in temperature between positions 1 and 2 has a similar magnitude for the simulated results as for the experimental results. This implies that the heat loss along the pipe between these points is well simulated, but the overall warm-up rate of the system is overestimated

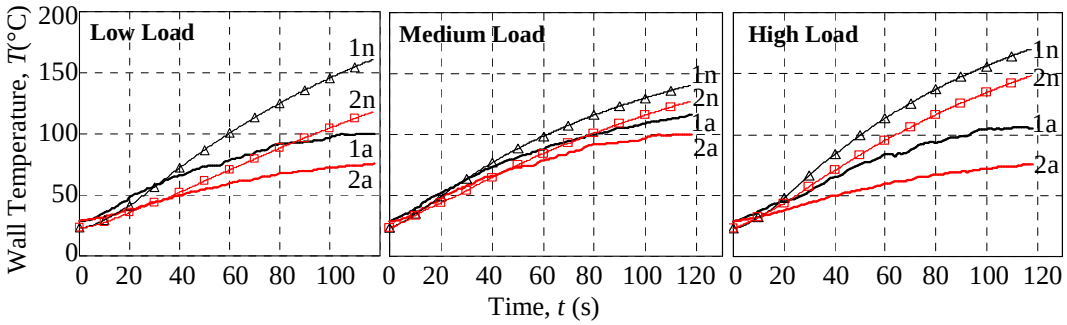


1: Takedown Inlet (a) Measured, Surface sensor, (n) Simulated
2: Takedown Outlet (a) Measured, Surface sensor, (n) Simulated

**Figure 6.6 Measured and Simulated Pipe Wall Temperatures for Experimental Setup 1 at Low, Medium and High Loads**

That both the gas and wall temperatures are higher at position 1 implies that either the total thermal mass of the wall or the external heat loss is underestimated. Both these values were set at the upper limit of what is reasonable under the test conditions. However, the thermal mass due to the three dimensional geometries of the system, such as connecting flanges, may not have been accurately represented in the one dimensional model, particularly in the manifold. This is a point of further discussion in Section 7.

Referring back to Figure 6.5, the simulation results at the catalytic converter mid-bed and outlet, positions 3 and 4, are now considered. These temperatures exhibit the most noticeable deviation from the experimental results, namely a brief but very high temperature rise seen in both temperatures between 20 s and 30 s. (This rise will be referred to as the gas temperature *spike* for the remainder of the text.) Note that in Figure 6.5 the height of the spikes has been reduced. The maximum peak values reached are in the order of 500 °C. This spike initiates the plateau period of the simulation results. The plateau starts slightly later than the measured plateau for the low and medium loads, but at the same time as the measured plateau for the high load.

These spikes are a result modelled rates of condensation and evaporation. The model implemented to account for homogeneous condensation when the gas temperature drops below the saturated temperature of the vapour assumes that all excess vapour immediately condenses onto the wall until a perfectly saturated condition is reached. This model results in the sudden formation of a large amount of liquid. This liquid rapidly evaporates when the gas is no longer saturated. This rapid evaporation causes the gas mixture to exceed the equilibrium saturation condition, resulting in a sharp rise in temperature.

The gas temperature spike was mentioned in Section 3 during the discussion of the grid independence of the numerical simulation. During grid independence analysis it was found that a reduction in the size of the time step did not significantly reduce the peak value obtained in this spike, but did cause the spike to occur approximately 5 s later. The elimination of this spike must therefore be brought about by refinement of the modelling method rather than the grid. Factors in the model influencing this spike are investigated in Section 7. It is noted however that although the spike itself is not fully time-step independent, the reduction of the time step by a factor of 10 did not produce a significant difference in the temperature to which the simulation plateaus settled after the spike.

In all three load cases, the simulation plateau occurs at a higher value than the experimental result, with the greatest offset occurring at the medium load. This is attributed to the mass of vapour in each control volume being underestimated by the simulated model, resulting in a higher saturation temperature. The factors in the model that cause this underestimation are investigated in Section 7.

Despite the initial spike and the higher plateau level, the shapes of the simulated temperature curves at both position 3 and 4 correlate very well to the experiment. The temperatures start to rise at almost exactly the same time, and at approximately the same rate, as the experimental temperatures at both positions and for all three loads. The result at the low load illustrates this the most clearly, with the initial offset in temperature after the spike remaining almost perfectly constant for the duration of the test. The warm up characteristics of the catalytic converter are therefore being well captured by the simulation.

The simulated results for the wall temperatures at positions 3 and 4 followed the gas temperatures very closely, as expected due to the relatively large heat transfer surface. The gas and wall differed by less than 6 °C at all times, except at the spike in the gas temperature. At this point the peak in the wall temperature was limited to an amplitude of approximately 10 °C above the corresponding plateau temperatures due to the thermal inertia of the wall. This following of the gas and wall temperatures in the catalytic converter was observed for all three load cases.

### 6.2.2 Numerical Simulation Results for Experimental Setup 2

The numerical simulation results for the gas and wall temperatures obtained at the three loads for each of the three manifolds of ES2 are given in Figure 6.7, alongside the experimental results. The simulated gas temperatures are strongly influenced by the shape of the input temperature functions. An initial overshoot followed by a lower gradient than the measured temperatures is observed at both points.

This results in the best correlation at the low loads of manifolds 1 and 2, due to the relatively low temperature gradient in the experimental results. As the load increases, and when the thin walled manifold is used, the temperature gradients of the experimental results increase more than the gradients of the simulation do. However, the simulated temperatures still tend to remain in the same range as the measured temperatures, falling mostly between the measurements from the two types of sensors.

The magnitude of the changes in the measured temperatures due to the increasing load is followed well by the simulation. The simulation shows the same insensitivity to the slight change in thermal mass between manifolds 1 and 2, as a comparison of the simulation results for these manifolds shows no significant differences. The increase in temperature when the thin walled manifold is used is also fairly well reflected by the simulation, although with a slightly higher result at position 2 for the high load case.

The effect of the condensation and evaporation is again observed at position 2. This is most noticeable at the low load where it produces a slight rise in the gas temperature between 50 s and 100 s for manifolds 1 and 2. A shorter peak just before 50 s is observed in the hotter conditions of manifold 3.

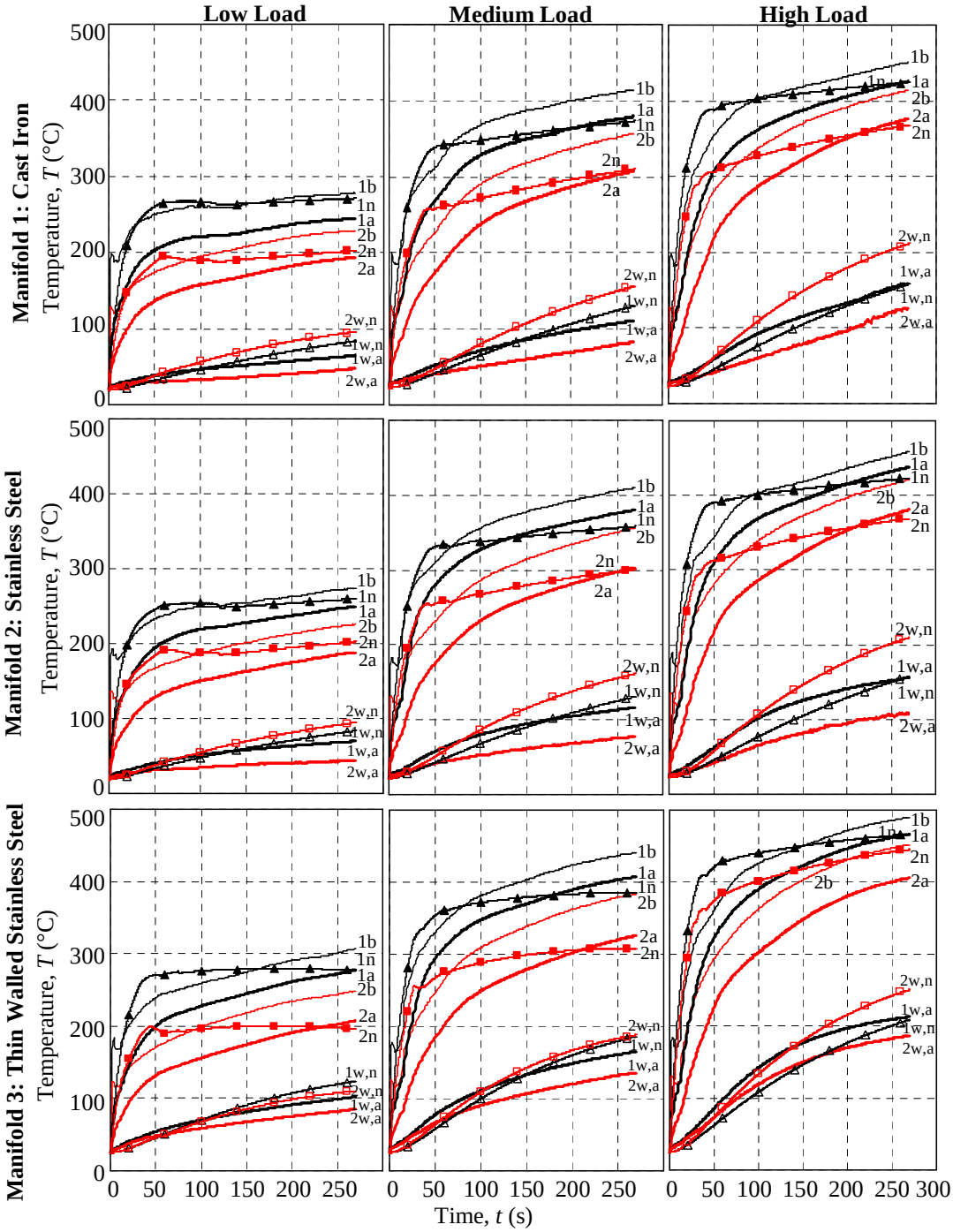


1: Takedown Inlet (a) Measured, Unshielded Sensor, (b) Measured, Shielded Sensor, (n) Simulated
2: Takedown Exit (a) Measured, Unshielded sensor, (b) measured, Shielded Sensor, (n) Simulated
1w: Takedown Inlet Wall (a) Measured, Surface Sensor, (n) Simulated
2w: Takedown Exit Wall (a) Measured, Surface Sensor, (n) Simulated

**Figure 6.7 Measured and Simulated Gas and Wall Temperatures for Experimental Setup 2, All Manifolds at Low, Medium and High Loads**

For this experimental setup the moisture effect is also noticeable at position 1 for the low load, due to the lower mass flow rates and slower warm-up of this setup compared with ES1. The moisture effects also occur at the higher loads, but are less noticeable due to the rising gas temperatures. It is again observed that these simulated moisture effects are not reflected in the experimental results and so the moisture model may need to be re-evaluated for this exhaust system.

The simulated wall temperatures at position 1 show a good correlation for all three manifolds although slightly high gradients are observed at the low and medium loads. The high load wall temperature attains a value close to the experimental value at 300 s, but with a more linear gradient than the experimental curve.

The simulated wall temperatures at position 2 are consistently higher than both the experiment and the simulated temperatures at position 1. As for the wall temperature results in ES1, these results are at least partly attributed to the three dimensional geometry of the wall not being realistically accounted for in takedown pipe. It was also found that the simulation was sensitive to the rate of axial conduction out of the final control volume of the takedown pipe section of the simulation (cv(*n*) in Figure 3.4). The boundary condition governing the conduction rate is the temperature of the silencer pipe wall (and the catalytic converter outer housing for ES1), which is not definitively known. The wall temperature model and the choice of the boundary conditions at the end of the takedown pipe section for both experimental setups will be discussed in detail in Section 7.

The comparison of the experimental and numerically simulated results has highlighted a number of points that require further discussion. Before these points are addressed in the general discussions, the liquid mass formation predicted by the numerical simulation of ES1 is reported.

### 6.2.3 Liquid Accumulation Predicted by the Numerical Simulation

In addition to modeling the temperature behavior, it was a goal of the simulation to determine the amount, position and duration of liquid accumulation in the exhaust system. The liquid mass present at selected positions along the length of the system with time, for ES1, is shown in Figures 6.8 and 6.9. The masses indicated are the total amount of liquid in a 1 cm section of the system at each position. The position is indicated by a distance from the exhaust port, where 0 m is immediately after the port and 0.95 m is the catalytic converter exit. The positions corresponding to the experimental points of measurement (as shown in Figure 6.1) are also indicated.

Figure 6.8 shows the liquid accumulation in the manifold and takedown pipe sections of the exhaust system for ES1. It is seen that the mass of liquid at all positions in the pipes changes in a roughly parabolic manner with time. The initial increase is due to heterogeneous condensation occurring against the cold walls. As

the gas temperatures rise, the rate of condensation slows until a turnaround point is reached. Evaporation then begins and continues until no more moisture is present.

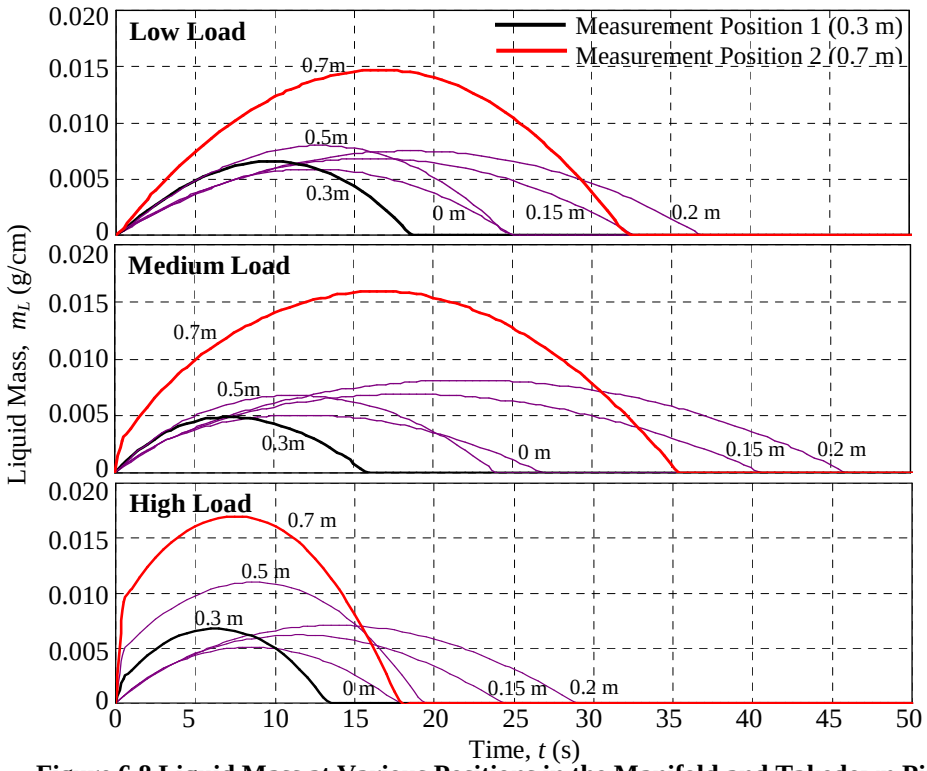


**Figure 6.8 Liquid Mass at Various Positions in the Manifold and Takedown Pipe of Experimental Setup 1**

The peak moisture mass achieved is strongly influenced by the vapor mass flow rate, with higher peak masses at higher mass flow rates due to the larger amount of vapor available for condensation. This effect is illustrated at all three loads by the large liquid mass observed at 0.7 m (the takedown pipe outlet). At this position the mass flow rate is higher because the total flow is combined into a single pipe, compared to the upstream sections where the flow is divided between 2 or 4 pipes. The peak at 0.7 m also increases as the load (and corresponding total flow rate) increases.

Higher mass flow rates also increase the rate at which both condensation and evaporation occur. This happens because the heterogeneous mass transfer equation is partly governed by convection (due to the dependence of the coefficient of mass transfer on the Reynolds number of the flow). The total duration for which liquid is present is therefore decreased by a higher mass flow rate. This results in the liquid at the high load forming and evaporating in almost half the time it does at the low load, where comparable temperatures but much lower mass transfer rates occur.

The response of the mass transfer to gas temperatures is as expected, with an increasing temperature tending to decrease both the peak liquid mass achieved

and the duration of the liquid presence. This effect is illustrated at the medium load, where the liquid is present for longer periods than at the other loads. The mass flow rate is higher than that at the low load, but the gas temperatures occurring at the medium load are significantly lower than for either of the other loads.

The change in liquid mass at each position in a given load is a result of the combination of the effects of mass flow rate and temperature. In the manifold pipes, the temperatures are high, resulting in a low peak liquid mass. The low flow rate in the manifold also contributes to this low peak, but tends to increase the time for which liquid is present. At the outlet of the takedown (0.7 m), the opposite holds. Low temperatures and high mass flow rates result in a much higher peak liquid mass, but the higher flow rate causes the liquid to form and evaporate at a higher rate than at the upstream positions.

The moisture accumulation in the catalytic converter is shown in Figure 6.9. It is immediately noted that the moisture masses show much more sudden changes than were seen in the pipe sections. At the inlet the same roughly parabolic change in mass is seen, but towards the outlet of the catalytic converter liquid peaks of increasing height and decreasing duration occur. These peaks are due to the cumulative effect of evaporating liquid upstream adding vapor to the gas flow. The increased vapour pressure in the gas causes a larger amount of condensation to occur downstream. This liquid then also evaporates, causing more vapour to enter the gas. As the vapour rich gas mixture moves down the catalytic converter, this phenomenon becomes more severe. The sudden evaporation occurring during this process is the cause of the high spikes seen in the gas temperatures.

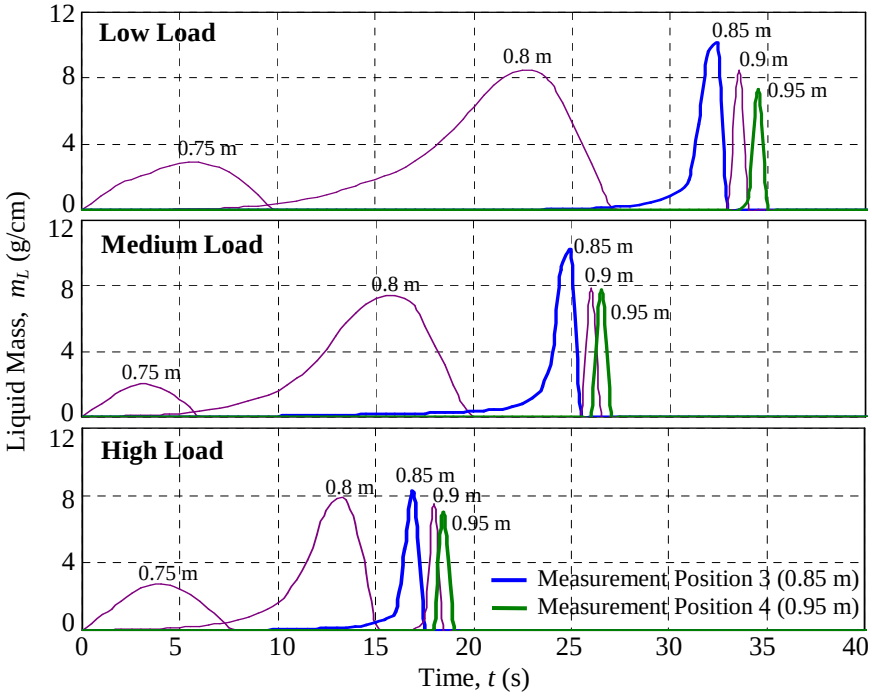


**Figure 6.9 Liquid Mass at Selected Positions in the Catalytic Converter**

In contrast to the trends observed in the pipe sections, the highest mass peaks are observed in the low load case. This is attributed to the lower mass flow rate causing the vapour rich gas to linger for longer in the system. The low mass flow rate also causes the peaks to form later than at the higher loads. At the high load the vapour is expelled from the system much more quickly, resulting in the lowest peaks and all liquid being evaporated before 20 s.

The spiking temperatures associated with the evaporation of the liquid mass peaks are not observed in the experimental results, but the unshielded sensors used in the catalytic converter have been shown to be poor at capturing fast changes in temperature. This was illustrated by the initial gas temperature peak at ignition in ES2 (shown in Figure 6.7) which was indicated by the shielded sensor, but not by the unshielded sensor. It is therefore possible that the actual rise to the plateau temperature is more sudden than the smooth rise observed in the experimental results. However, it is not considered likely that the real temperatures would exhibit such severe spiking behaviour.

It is suggested that in the numerical simulation the heat transfer effects of the moisture are confined to a shorter time period than in the actual exhaust system. The same amount of heat being transferred in a shorter time would result in an exaggeration of the temperature spikes compared to any that may occur in reality. Refinement of the mass transfer modelling and solution method to smooth this behaviour are required.

It is noted that although the predicted peaks in liquid mass are probably higher than in reality, they remain within a realistically plausible range. To illustrate this, the highest peak observed has a value of 12 g/cm (at 0.83 m for the low load). This has a volume of $12.1 \times 10^{-6}$ $m^3$ which is in the order of 20% of the volume available for gas mixture flow in a 1 cm section of the catalytic converter. If this mass was spread evenly over the surface of all the channels in the same section it would result in a film of 0.05 mm thick.

From the comparisons of the numerical simulation to the experimental results in the preceding sections it is apparent that the moisture models used still require some refinement before the results regarding the liquid formation can be regarded as conclusive. However, the results obtained give a prediction of timeframe and positions for which the liquid is present. They also provide insight into the effects of the moisture on the temperature behavior of the model, which is needed in order to implement improvements to the simulation method and results.

# 7 Discussion

The experimental investigation and numerical simulation are now discussed with the intention of clarifying the areas highlighted for further discussion in Section 6. These discussions begin with an overall assessment of the experimental investigation (Section 7.1), from which recommendations for future experimental work are made (Section 7.2). The numerical simulation is then discussed in some detail, both in response to the brief discussions in Section 6, and in order to determine how the moisture model influenced the results (Section 7.3). In light of both the experimental and numerical results conclusions regarding the influence of moisture on the temperatures in the exhaust system are drawn. Using these conclusions the original hypothesis of this research is revisited (section 7.4). Finally, recommendations regarding future numerical modelling are made (Section 7.5).

## 7.1 Assessment of the Experimental Investigation

The experimental investigation is assessed with regard to the performance of the shielded sensors. The general advantages and disadvantages of the experimental setups used are also discussed, so that recommendations can be made for future work.

### 7.1.1 Shielded Sensor Performance

The theory of errors associated with temperature measurement in flowing gas predicts that the shielded sensors will measure temperatures higher than the unshielded sensors, as discussed in Section 4. The temperature difference between the measurements of the two sensors should initially be higher because the fast time response of the shielded sensor allows it to warm up quickly. The difference then settles to an almost steady offset determined mainly by radiation losses experienced by the unshielded sensor. The shielded sensor experimental results presented in Section 6 are generally in agreement with this theory. The exception is the measurements obtained at position 1, for all three loads of ES1.

In order to understand this result the parameters governing the error calculation algorithm, including emissivity values, heat transfer coefficients and the thermal capacity of the materials used, were systematically varied. It was found that the algorithm used showed a high sensitivity to the value of the emissivity of the sensor. For the stainless steel thermocouple sheath the expected emissivity range is between a minimum of 0.2 (for a clean surface) and a maximum of 0.87 (for a stably oxidised surface) (Incropera and DeWitt, 2002). In the initial prediction of the sensor errors an emissivity of $\varepsilon = 0.4$ was used for both the shielded and unshielded sensors, as this is roughly the average for the expected range. This emissivity produced predicted true gas temperatures that correspond well with each other and with the data measured by shielded sensor, as is shown in Figure 4.7.

The range of the expected error corresponding to the minimum and maximum emissivity values is illustrated in Figure 7.1. The gas temperatures shown are predicted from a curve fit of the unshielded sensor reading at position 1 (for the low load of ES1). If the clean surface emissivity of 0.2 is used, the expected error is significantly reduced. This is a possible explanation of the gas temperature measurements at position 1 for ES1, where both sensor types measured approximately the same value after the initial fast temperature rise. The thermal inertia of the unshielded sensor still produces a noticeable error during the initial period where the temperature gradient is high. From this it is concluded that if a new or cleaned thermocouple was used at position 1, the insertion errors at the 'steady' temperature period will be less than the same errors if an oxidized thermocouple is used. This is the most likely cause for the results obtained, since the same thermocouple measured the small error at position 1 in all runs of each load case.

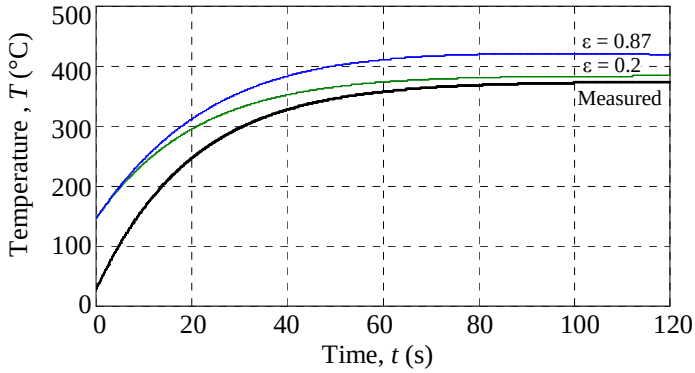


**Figure 7.1 Variation in Predicted Gas Temperatures due to a Change in Sensor Emissivity**

The observation regarding the effect of emissivity is interesting as it implies that the need for radiation shields on the sensor can be almost eliminated by properly cleaning or polishing the surface of the industry standard, unshielded thermocouple. However, the surface will deteriorate over time in the exhaust system, so the use of a new sensor in tests that require long test durations may produce a gradually increasing error. Such an error would be more difficult to quantify than the more constant errors associated with an oxidized/sooty surface on either an unshielded or shielded sensor.

Overall, the new design for a temperature sensor produced the desired increase in accuracy and decrease in response time, and the shielded sensors performed well. Although they are designed for use in a very limited temperature range, the increased accuracy obtained makes the use of the shielded sensors in more general applications desirable. If the thin unsheathed wire was replaced by a sheathed thermocouple the robustness of the sensor would be improved. This modification would cause the response time to increase, but if a thin sheathed thermocouple was used (1.5 mm diameter is listed as available in the Unitemp product catalogue, 2008) it would still be faster than the 3 mm diameter sensor. The conduction losses would also be increased, but it was found that even in the

extreme case of the wall at ambient temperature the conduction loss is small compared to the radiation loss, so this would be tolerable.

The modification of the shielded sensor design to increase its robustness while still maintaining the accuracy would allow the sensor to be used at the exhaust port. This would be beneficial to the research approach presented here as it would provide a more reliable value for the input temperature function used in the numerical simulation.

### 7.1.2 Advantages and Disadvantages of the Experimental Setups

The use of engine test cells to perform the experimental investigation has both advantages and disadvantages for the type of research being performed. The advantage of the use of an engine on a test bed is that the conditions in the exhaust system will be almost identical to the conditions in an actual vehicle exhaust system. The warm-up behaviour will therefore be a good representation of reality.

The use of the two types of sensors simultaneously is also advantageous. The unshielded sensors provide a set of measurements that can be compared to experimental work by others, since this is the established method of temperature measurement. The shielded sensors provide a set of more accurate measurements that are compared to those obtained by the unshielded sensors. This allows the insertion errors experienced by the unshielded sensors to be experimentally quantified.

The disadvantage of the comprehensiveness of using an actual exhaust system for the experimental setup is that it introduces a large number of variables whose effects must be accounted for. Many of these variables are difficult to control or quantify, such as the effect of the pressure waves and flow velocity variations caused by the valve cycle. These make accurate modelling of a real engine system extremely challenging.

In this research the moisture mass transfer is modelled using the analogy between heat and mass transfer and assuming the vapour to be an ideal gas (Cengel, 2003). This theory is previously untried in this application and so needs to be verified. The verification of the theory is hampered by the effects of the uncontrolled parameters because these are difficult to separate from the effects of the moisture model. Clarkson and Benjamin (1995) overcame this problem by means of a simplified experimental system in which the engine was fully warmed with the catalytic converter isolated. This allowed warm up of the catalytic converter to be investigated in the absence of the flow rate and temperature variations of the incoming gas.

As the moisture model used in this research needs refinement, the elimination of the uncontrolled variables by means of a simplified experimental approach would be beneficial.

## 7.2 Recommendations for Future Experimental Investigations

In order to verify the theory used in the moisture model, a simplification of the experimental system is recommended. In this simplified experiment as many of the uncertain or uncontrollable variables in the real exhaust system need to be quantified, fixed at a known value or eliminated from the system. In order to achieve this it is recommended that an initially highly simplified system, consisting of a single straight pipe connected to a non-reactive catalytic converter monolith, is used as a starting point. A constant, known input of gas with a constant composition and flow rate and a controlled amount of vapor should be applied. The effects of flow pulsing and pressure waves would thus be eliminated. If the input temperature, moisture composition and mass flow rates are carefully controlled and chosen to represent the actual exhaust conditions, this simple experiment can be effectively represented by a one-dimensional pipe flow model. Using this model the applicability of different moisture mass transfer models, for example homogeneous droplet formation, growth and deposition models (Kelleners, 2003) can be investigated.

Once a basic groundwork for an applicable model has been established the complexity of the experimental system and the numerical model can be simultaneously increased. The systematic introduction of parameters such as the pulsing flow rate, for example by the use of a pulse combustor (Depcik and Assanis, 2002) should be performed until the desired complexity of the simulation is reached. The moisture model can then be applied with more confidence to a model of an actual engine system.

The experimental investigation performed in this research is a useful starting point for the simplified experimental setup suggested here. It provides a set of realistic conditions in terms of temperature, mass flow rates and system geometry which must be represented by the simplified system if the verification of the theory is to be regarded as useful. Once the influence of the individual parameters in the real system on the moisture model is better understood the moisture model used in the numerical simulation created in this research can be refined and elaborated.

In the absence of the simplified experimental setup described here, the effects of individual parameters in the model must be investigated theoretically by making changes in the numerical simulation and observing the effect on the results.

## 7.3 Assessment of the Numerical Simulation

According to the original goals of this research, the numerical simulation included the effects of moisture in the exhaust system by calculating the two phase mass transfer processes along the length of the system. The inclusion of both condensation and evaporation effects, albeit in a highly simplified manner, and the prediction of liquid formation makes the moisture model presented here more comprehensive than the others reported in literature. However, the use of established two phase mass transfer theory in this particular application has not

been verified in the literature and so a detailed assessment of the numerical simulation is required.

The discussions that follow are divided into three main sections. In the first, Section 7.3.1, some of the simplifying assumptions made during the construction of the numerical model are assessed. In Section 7.3.2 the influence of variables in the parts of the model not related to the moisture modelling, is investigated. The variables discussed include the choice of *CAF*, the physical properties of the exhaust system walls and the input temperature function used. In Section 7.3.3 a detailed investigation of the influence the moisture model on the simulation results is performed. The individual influences of evaporation, heterogeneous and homogeneous condensation and a potential initial liquid mass present in the catalytic converter are investigated.

The discussions in this section are detailed in order to fully understand the various influences on the simulation results, and as a result are lengthy. These discussions, particularly those relating to the moisture effects, will be summarised in Section 7.4 so that conclusions regarding the moisture model can be drawn. Recommendations for future numerical simulations are made in Section 7.5.

### 7.3.1 Validity of Modelling Simplifications

Most of the assumptions made during the construction of the numerical simulation have been established in the literature as reasonable when modelling the flow in the exhaust system (as discussed in Section 3.2) and so will not be discussed further here. Two simplifications made that do need to be reconsidered in light of the results obtained are the assumption of negligible effect of exothermic reactions in the catalytic converter, and the method of approximating the local gas mixture velocity along the length of the model.

#### 7.3.1.1 Neglecting of the Catalytic Converter Exothermic Reactions

As it was not a goal of this research to model the exothermic reactions in the catalytic converter the experimental method was designed to deliberately limit these reactions in two ways. Firstly, the tests were performed only in the period before the gas temperatures increased to the point where light-off is expected, and secondly by using an old catalytic converter which had been poisoned by extensive use in R&D applications. However, in a functional catalytic converter some reactions do occur before light-off and furthermore the extent of the poisoning of the catalytic converter used was not certain. The validity of the neglecting these reactions must therefore be assessed by comparison of the experimental results obtained in this research with those obtained by others.

Previous research using the same Bora engine as was used in ES1 was performed by Marais (2005). Figure 7.2 shows the gas temperatures measured at the port and at positions equivalent to positions 2, 3 and 4 of this research. The test shown below cannot be directly compared to the experimental results of this research

because it was performed at a higher speed and load, and had a longer initial idle period, but some features regarding the temperature profiles are noted.

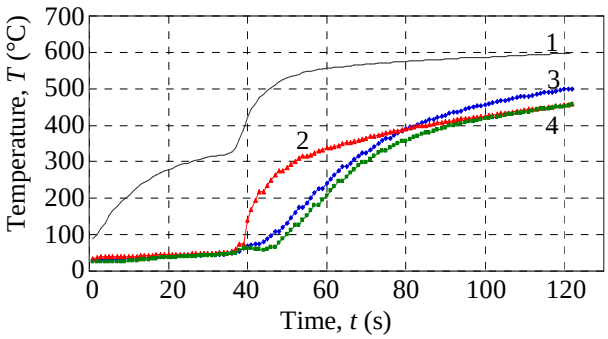


1: Port, 2: Takedown Pipe Outlet
3: Catalytic Converter Mid-Bed, 4: Catalytic Converter Outlet

**Figure 7.2 Experimental Gas Temperatures Obtained by Marais (2005) for a Reactive Catalytic Converter**

It is seen that the gas temperature at the catalytic converter inlet reaches 300 °C within 10 s after the load is applied (at 40 s). This is hot enough for a rapid warm up of the catalytic converter and significant exothermic reactions to be expected. This expected warm-up behaviour is observed in the two downstream temperatures, which not only rise rapidly but exceed the incoming temperatures due to the heat added by the exothermic reactions. The rapid warm-up associated with the exothermic reactions is also illustrated in the work of Benjamin (2003) and Siemund *et al.* (1996), but is not observed in the experimental results obtained in this research. Furthermore, experiments by Clarkson and Benjamin (1995) using a monolith with no catalyst present showed very similar behaviour to the experimental results of this research.

The moderate temperature gradients measured in the catalytic converter were well represented by the numerical simulation without the effect of exothermic reactions being included in the model (as illustrated in Figure 6.5). It is therefore concluded that the low gas temperatures and full or partial poisoning of the catalytic converter resulted in the exothermic reactions occurring at a low enough rate for them to be neglected.

#### 7.3.1.2 Approximation of the Gas Mixture Flow Rate

The gas mixture flow rate along the system was calculated by assuming that the input volumetric flow rate increased or decreased in proportion to the expected change in volume predicted by the ideal gas equation. The volume changes are caused by changes in the temperature and mass composition of the gas at each position in the exhaust system. A factor of expansion/contraction $K_V$, as defined in Section 3.3 was used to calculate the flow rate in each control volume. The principle behind this use of this factor is the assumption that for the conditions prevailing in the control volume the continuity equation (given by the sum of

Equations 3.3 and 3.4) and the ideal gas equation should predict the same mass in the control volume. The true volumetric flow rate out of the control volume is therefore such that allows the mass predicted by the continuity equation to agree with the mass predicted by the ideal gas equation. If both equations predict the same mass $K_V$ will be equal to unity.

In order to assess the success of this method the value of $K_V$ was observed over the length of the system for the whole time period. The value was found to fluctuate close to unity for the most part, with an average value of 0.9. The value slightly less than unity is consistent with the contraction of the gas along the system as heat is lost to the walls. A peak value was observed at the time and position of the highest gas temperature spike (for the high load of ES1 this value reached 2.7). This is consistent with the excess amount of mass in the gas mixture control volume due to the high rate of evaporation. The high $K_V$ value causes the flow rate to increase significantly in order to reduce the mass to what is physically realistic according to the ideal gas equation.

As the mass moves downstream the $K_V$ value in the next control volume increases, resulting in a front of high moisture content gas moving down the system. If the high mass flow rate out of the control volume coincides with a high evaporation rate in the following control volume, the mass accumulation effect of the evaporation will be compounded.

Since the flow rate is only adjusted after a discrepancy between the masses predicted by the continuity and ideal gas equations is detected, a ‘lag’ in the correction of the flow rate occurs. As a consequence the gas mixture mass in each control volume tends to be slightly lower than the ideal gas equation predicts. This is suggested as a cause of the discrepancy between the measured and simulated plateau temperatures. The lower vapour mass results in a lower partial pressure of vapour and so a higher saturation temperature to which the system tends to settle after the evaporation of the liquid.

The method of approximation of the volumetric flow rate maintains gas mixture masses in the control volumes close to the values predicted by the ideal gas equation. If the model had only single phase effects included, this method would be a simple yet effective way to estimate the gas velocity. In the model with the two-phase effects included, the high sensitivity of the moisture model to the vapour pressure discrepancies results in deviations from the experimental temperatures, particularly at high evaporation rates. A different approach to the method of solving the momentum equation laid out in Section 3.3 should therefore be considered if moisture effects are to be included in a model.

### 7.3.2 Discussion of Individual Parameters in the General Numerical Simulation

In the discussion of the results in Section 6 it was noted that the gas and wall temperatures in the numerical simulation results showed a strong dependence on the value of *CAF* and input temperature function used. It was further observed that the simulated wall temperatures were generally higher than those obtained from the experimental investigation.

The value of the *CAF* is defined by comparison of numerical and experimental results for a specific system (Wendland, 1993). The choice of values used in this research is assessed by comparison of the values for the two experimental setups to each other and to values reported in literature. The *CAF* and other factors influencing the pipe wall temperatures are then discussed in order to determine possible reasons for the high wall temperatures obtained from the numerical simulation. This allows the relation between the *CAF* and the gas and wall temperatures to be more clearly understood, so that the choice of input temperature function can be discussed.

#### 7.3.2.1 Assessment of Choice of *CAF*

In order to account for the increased turbulence occurring in the exhaust system due to the pulsing flow fluctuations the Nusselt correlation proposed by Meisner and Sorenson (1986) was used in combination with a *CAF*. The values of the *CAF* used to produce the results given in Section 6 are listed in Table 7.1

**Table 7.1 Convective Augmentation Factor Values for Experimental Setups 1 and 2**

| Load | *CAF* | |
|---|---|---|
| | ES1 | ES2 |
| High | 1.2 | 0.7 |
| Medium | 1.5 | 1.0 |
| Low | 1.1 | 1.1 |

The values show the general trend of decreasing with an increase in temperature. The medium load for ES1 has the lowest gas temperatures measured at positions 1 and 2 and the highest *CAF* (1.5). The lowest *CAF* (0.7) is applied to the high load of ES2, where the measured gas temperatures are the highest.

The temperatures at the high load of ES2 are only slightly higher than those at the low load of ES1 (which had the highest temperatures for ES1). At first glance one would therefore expect the *CAF* to have a similar value. This is not the case and is attributed to two observations regarding the temperatures. Firstly, the time taken to reach a maximum gas temperature of approximately 400°C at position 1 is 300 s for ES2 compared to the 120 s for ES1. Secondly, the measured port temperatures are higher for ES1, while the downstream temperatures are higher for ES2. The larger temperature drop occurring in a shorter period in the experimental results of ES1 indicates a much higher heat transfer rate for this

exhaust system. This is consistent with the higher *CAF* values required in the numerical simulations of ES1.

The required *CAF* values of 0.7 to 1.1 for ES2 indicate that the Nusselt correlation proposed by Meisner and Sorenson over-estimates the heat transfer for this exhaust system at the high load, produces a good result for the medium load and slightly underestimates the heat transfer at the low load. This correlation must be increased at all loads to produce a reasonable result for ES1.

It is noted that in comparison to values reported in literature the *CAF* values used here are low. Depcik and Assanis (2002) compared the methods used by a number of researchers in regard to the exhaust system turbulence and found that the *CAF* values used ranged on average between 2 and 3. Cho *et al.* (1997), however, reported a value of 1.4 in their research, which is comparable to the values used here. Higher values of the *CAF* would be required if a more conventional Nusselt correlation such as the simple power law correlation given by Equation 2.8 was used instead of the Meisner and Sorenson correlation.

Overall the upper value of the CAF used in the numerical simulations was limited less by the results for the gas temperatures than by the wall temperatures, as the latter temperatures were found to be higher than expected. An increase in *CAF* would further increase the wall temperatures and so is undesirable.

#### 7.3.2.2 Influence of the Physical Properties of the Walls

The wall temperatures are dependent on a number of parameters including the wall dimensions and the density, thermal capacity and thermal conductivity of the exhaust pipe materials. The factors governing the rates of heat transfer to and from the wall by internal and external convection, radiation and axial conduction also influence the wall temperatures. In order to determine the dependence of the wall temperature on these parameters they were individually varied and the effect on the simulation results investigated.

It was found that the wall temperatures were not strongly dependent on the external radiation and convection when these were varied within a physically reasonable range. This range was defined by the outside emissivity of the pipe, ranging from 0.4 to 1.0 for a polished or oxidised surface respectively, and the heat transfer coefficient due to natural convection which was varied between 5 and 20 $W/m^2K$. The simulated wall temperatures also showed little dependence on the internal gas-radiation and variations in the wall heat capacity due to a material change. Factors that strongly influenced the wall temperatures were the internal convection heat transfer rate (and hence the choice of *CAF*), the wall mass and the axial thermal conduction. These three parameters are not completely fixed in the simulation due to uncertainty surrounding the physical exhaust system.

The *CAF*, as mentioned, is an unknown factor whose value is inherent to each exhaust system individually, so a wide range of potential values exists. As the

wall temperatures were higher than those experimentally measured, the *CAF* values were chosen to be as low as possible while still producing an acceptable gas temperature result. It should be mentioned here that the gas temperature was more strongly influenced by a change in *CAF* than the wall temperatures were, so a change in the *CAF* to produce a small improvement in the wall temperatures would create a larger deterioration in the gas temperature correlation.

The mass of the wall is determined by the density, which is known for the materials used, and the dimensions of the pipe walls. The wall dimensions are difficult to accurately represent due to the continuously changing wall profile in the manifold casting. The two-dimensional wall profile was represented in the simulation by a constant average wall thickness. Other three-dimensional geometries of the manifold, including the change in wall mass as the pipes join together, as well as flanges at the joint between the manifold and takedown pipes, are difficult to accurately represented using the one-dimensional model.

A thermal image of the cast iron manifold for ES2 is shown for qualitative purposes in Figure 7.3, with the cooler flange clearly visible. Added masses such as this flange act as local heat sinks on the pipe wall in the experiment. This is believed to be a contributing factor to the higher wall temperatures in the simulation, especially since the takedown pipe inlet wall temperature was measured close to the connecting flange shown in the figure.

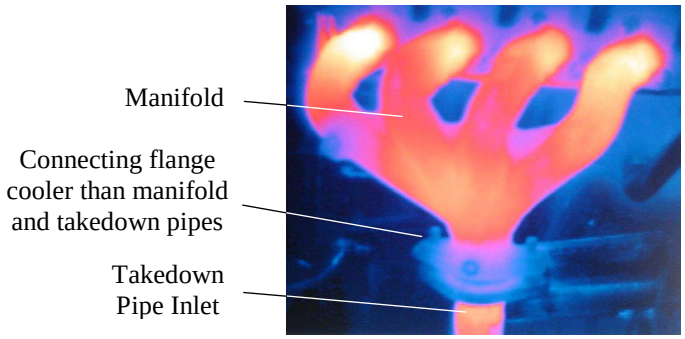


**Figure 7.3 Thermal Image of the Cast Iron Manifold of Experimental Setup 2 with Cool Connecting Flange**

The total mass of the system could be accounted for more accurately by weighing each system component and obtaining an average wall thickness from this, rather than the wall profile. This should improve the correlation to some degree, but would still not reflect local temperature variations due to the three-dimensional geometry of the system.

The axial conduction was determined by the thermal conductivity, fixed for the given wall materials, and the boundary conditions at the manifold inlet and the takedown pipe outlet. At the manifold inlet the boundary condition for the conduction into the system is the temperature of the engine housing to which the manifold is connected. At the exit of the takedown pipe the boundary condition is

the temperature of the catalytic converter housing for ES1 and of the silencer pipe for ES2. None of these temperatures were known from the experiments, nor were these sections of the exhaust system included in the numerical simulation.

In the absence of known boundary temperatures the conduction at the boundaries was approximated. For the results reported in Section 6 this was done by linearly projecting the gradient of change in conductive heat flux from the adjacent control volumes. At the takedown pipe exit (cv = *n*) this is defined as:

$$\dot{Q}_{cond\,(n)} - \dot{Q}_{cond\,(n-1)} = \dot{Q}_{cond\,(n-1)} - \dot{Q}_{cond\,(n-2)} \qquad 7.1$$

which is solved for the unknown net conductive heat flux from cv(*n*), $Q_{cond\,(n)}$. This boundary condition assumes that there is no sudden change in wall temperature after cv(*n*), that is, that the drop in wall temperature from cv(*n*) to the undefined cv(*n*+1) is comparable to that from cv(*n*-1) to cv(*n*).

The influence of changing the boundary condition on the simulated wall temperatures was investigated. It was found if the conductive flux out of the last control volume is increased a significant drop in wall temperature was achieved. A wall temperature much more in agreement with the measured values at the takedown pipe exit was obtained if the boundary condition was defined by setting the wall temperature of cv(*n*+1) as the average of the ambient temperature and the temperature of cv(*n*). This is given by:

$$T_{wall\,(n+1)} = \frac{T_{wall\,(n)} + T_{amb}}{2} \qquad 7.2$$

This boundary condition assumes a sudden drop in temperature from cv(*n*) to cv(*n*+1). At this position in both exhaust systems the pipe diameter increases, causing an increase in wall thermal mass. Furthermore, in the case of ES2, the catalytic converter housing is insulated to a certain degree from the gas flow by the matting around the monolith. A lower in wall temperature in these sections of the pipe is therefore not an unreasonable assumption. However, the temperature drop is unlikely to be as severe across a single control volume length as the condition in Equation 7.2 would require. The lack of a reliable boundary condition is particularly problematic because the wall temperature measurement at the takedown pipe exit is compared to the simulated temperature in a control volume close to the boundary.

The boundary condition could be more clearly defined by measurement of the wall temperatures at a position adjacent to that at which the numerical simulation ends. Alternatively, the numerical simulation could be extended to include enough of the adjacent pipe for the boundary condition to have less influence on the control volume of interest (being that corresponding to measurement position 2). If the model is extended the two-dimensional geometry of the silencer or catalytic converter housing will have to be accounted for. Cho *et al*. (1997) countered the

problem of uncertain boundary values for conduction by applying gaskets, assumed to be perfect insulators, to both ends of the modelled section of the exhaust system. Such an approach could be applied to the future experimental setup suggested in Section 7.2.

#### 7.3.2.3 Influence of the Input Temperature Function

The results obtained from the numerical simulation show a very high dependence on both the range and shape of the input temperature function used. From the theory of temperature measurement, discussed in detail in Section 4, it is expected that the temperatures measured by the unshielded thermocouples at the exhaust port are lower than the true port temperatures. The simple algorithm written to predict the true gas temperatures using the general theory produced good results in the takedown section of the exhaust system (where shielded sensor measurements were also taken for comparison to the theory). The same algorithm was then used to predict the true port temperatures.

It is difficult to confirm the validity of using this algorithm at the port, since no shielded thermocouple was present at this position. Temperature dependent factors such as surface emissivity are likely to differ between the takedown section and the exhaust port where the temperatures are significantly higher. The flow also fluctuates most severely at port due to the valve cycle, creating dissimilar convective heat transfer conditions between the port and takedown. One of the decisions that had to be made during the formulation of the numerical simulation was whether to use the measured port gas temperatures as the input temperature, or whether to use the theoretically predicted true gas temperatures.

Considering first the results obtained using the measured values directly (as shown in Figures 6.2 to 6.4), it is seen that the gas temperatures show a strong dependence on the shape of the input curve. This is not a very good representation of the shape of the measured temperature curves, with the most notable discrepancies being the initial overshoot and the low ‘steady state’ gradient. However, the average range of the simulated gas temperatures generally correlates well to the experiment (as discussed in Section 6).

If the theoretically predicted true port temperatures were used, with the same turbulence enhancement as the case discussed above, higher gas and wall temperatures occurred at both measuring points. The gas temperatures could be reduced to a level representative of the measured values by increasing the turbulence augmentation factor to $CAF = 2$ in the manifold convection equations. The results obtained for this simulation are shown in Figure 7.4 (ii), alongside the result obtained using the measured port temperature and a $CAF = 1.1$ (as was previously shown in Figure 6.4).

The increased *CAF* results in a good correlation for the gas temperatures at position 1 and a slightly low gas temperature at position 2. The advantage that this configuration has over that using the measured port temperatures is an

improvement in the gradients of the simulated gas temperatures at positions 1 and 2. The wall temperatures are, however, even higher than the previously obtained wall temperatures due to the higher input temperature and the increased rate of convection. As the wall temperatures are a relevant parameter to the moisture behaviour model, the high wall temperatures obtained in the simulation using the theoretical port temperatures are regarded as more detrimental to this application than the shape of the gas temperature curves. It was therefore decided to use the measured temperatures directly.

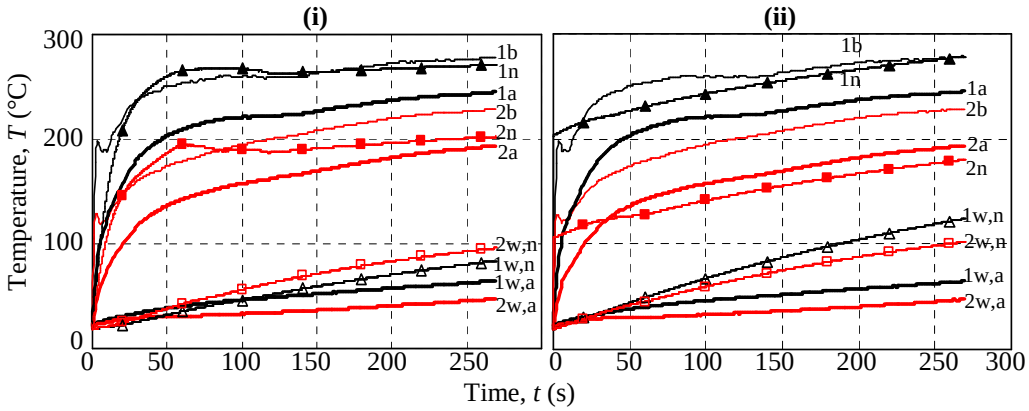


1: Takedown Inlet Gas (a) Measured, Unshielded Sensor, (b) Measured, Shielded Sensor, (n) Simulated
2: Takedown Exit Gas (a) Measured, Unshielded Sensor, (b) Measured, Shielded Sensor, (n) Simulated
1w: Takedown Inlet Wall (a) Measured, Surface Sensor, (n) Simulated
2w: Takedown Exit Wall (a) Measured, Surface Sensor, (n) Simulated

**Figure 7.4 Results for Experimental Setup 2, Cast Iron Manifold, Low Load with (i) Measured Input Temperature and *CAF* = 1.1 and (ii) Theoretically Predicted Input Temperature and *CAF* = 2**

As the simulation results show such sensitivity to the input function used, improvement of this parameter is a key area for improvement of the numerical model. The results of this investigation imply that the sensor theory over-estimates the error experienced by the thermocouple at the port. The convective heat transfer to the sensor may need to be adjusted by means of a *CAF* specific to the region immediately after the port, due to the high gas flow rate fluctuations at this point. Like the *CAF* used for the general manifold flow, this value would have to be experimentally determined. The modifications to the design of the shielded sensor recommended in Section 7.1 would allow the shielded sensor to be used at the port itself. This would provide both a more accurate port gas temperature measurement and a method of verifying the error theory at this point in the exhaust system.

### 7.3.3 Discussion of Individual Parameters in the Moisture Model

In order to gain a better understanding of the effects of moisture and the behaviour of the model, the rates of evaporation and homogeneous and heterogeneous condensation in the model were varied. The effect of including an initial liquid mass in the catalytic converter was also investigated. In this way the influence of each phenomenon being modelled could be isolated and assessed.

#### 7.3.3.1 'Dry' Gas Numerical Simulation

The first comparison made was between the results obtained for the model as shown in Section 6, and the same model with no moisture mass transfer. The results for this 'dry' model, for the low load case of ES1, are shown in Figure 7.5, alongside the results for the same case with the moisture effects included.

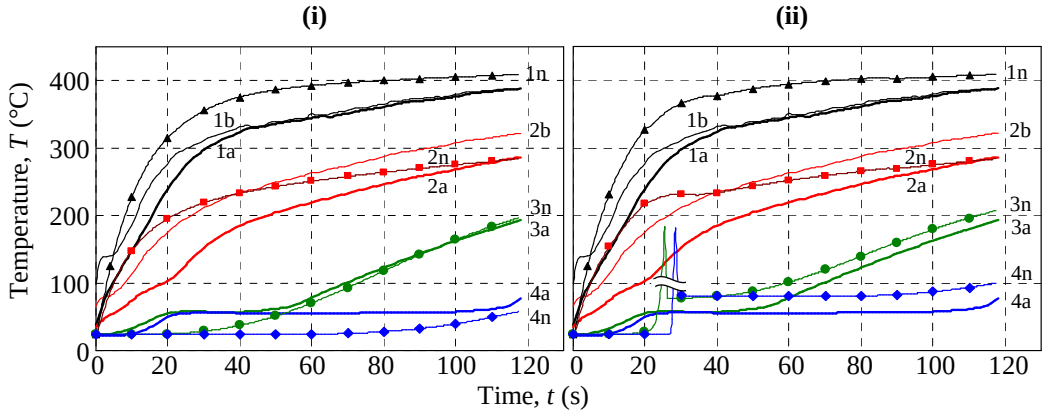


1: Takedown Inlet (a) Measured, Unshielded Sensor, (b) Measured, Shielded Sensor, (n) Simulated
2: Takedown Exit (a) Measured, Unshielded Sensor, (b) Measured, Shielded Sensor,(n) Simulated
3: Catalytic Converter Mid-Bed (a) Measured, Unshielded Sensor, (n) Simulated
4: Catalytic Converter Outlet (a) Measured, Unshielded Sensor, (n) Simulated

**Figure 7.5 Gas Temperatures for Experimental Setup 1, Low load with (i) Moisture Effects Omitted and (ii) Moisture Effects Included**

At position 1 the moisture is seen to have had little effect, other than the dry model curves being slightly smoother. At position 2 the 'hump' in the temperature between 20 and 40 s is absent, but the temperature curves are otherwise very similar. At positions 3 and 4, in the catalytic converter, the removal of the moisture causes a significant change. The sharp spike in gas temperature caused by the rapid evaporation is, of course, absent from the 'dry' model results and the gas temperature does not step up to a plateau temperature. Instead a smooth and initially very slow temperature rise is seen. As the thermal inertia of the monolith walls is overcome the gas temperatures start to rise more rapidly, and by 50 s the 'dry' model results at position 3 correspond very closely to the experimental results. At position 4 the simulated temperatures only start to show a noticeable increase at 80 s. By 120 s the temperatures begin approach the experimental result, which is just starting to rise from the plateau temperature.

The initial slow increase seen in the 'dry' results concurs with the results obtained by Chan and Hoang (1999) for their model when moisture effects were neglected (as shown in Figure 2.3 in the literature review). The 'dry' version of the numerical simulation is therefore regarded as a good foundation to be used to investigate the effects of individual parameters in the moisture model.

#### 7.3.3.2 Influence of the Moisture Mass Transfer

As mentioned in the literature study, the moisture model includes heterogeneous and homogeneous mass transfer. Heterogeneous mass transfer governs the evaporation as well as the condensation that occurs at the wall while the wall

temperature is below the saturation temperature of the bulk vapour. The homogeneous mass transfer is the condensation of vapour from the gas when the bulk gas mixture temperature drops below the saturation temperature of the vapour. The individual influences of these processes in the moisture model are now investigated in the pipe sections upstream of the catalytic converter, and in the catalytic converter itself.

The slight temperature fluctuations seen in the pipe sections, as well as in the catalytic converter before the temperature spike, are due to heterogeneous condensation and subsequent evaporation. It was found that if the heterogeneous mass transfer is omitted, the temperatures in the pipe sections take the form of those from the dry model. It is therefore concluded that only heterogeneous condensation and evaporation occur in these sections. This agrees with the simple example calculation performed in Section 2.3, which predicts that the gas in the pipe sections will remain above the vapour saturation temperature despite the initial expansion cooling at the valve. Homogeneous condensation therefore does not occur at the port. The absence of homogeneous condensation in the remainder of the pipe sections indicates that the cooling rate in the pipe sections is insufficient to reduce the bulk gas temperatures to below the saturation temperature of the vapour.

If the rate of heterogeneous mass transfer is decreased in the pipe sections the moisture induced fluctuations observed in the temperatures are reduced. Figure 7.6 illustrates this for the low load case of ES1, in which it is seen that the moisture induced fluctuations take the form of an uneven 'hump' between 30 and 100 s. The height of the 'hump' is lowered by approximately 10 °C when the mass transfer rate is halved (curve b in the figure). The 'hump' is eliminated in the 'dry' case (curve c).

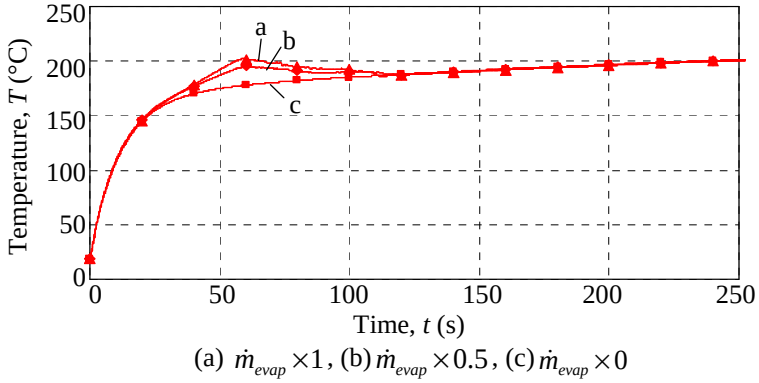


**Figure 7.6 Simulated Gas Temperature at Takedown Pipe Outlet of Experimental Setup 2, Low Load for Different Evaporation Rates**

It is noted that although the heterogeneous mass transfer model predicts the occurrence of these moisture induced gas temperature fluctuations, these fluctuations are not observed in the experimental results. In the pipe sections the gas temperatures are in fact better represented by the 'dry' model. It may be that

the mass transfer, like the heat transfer, is accelerated by the high turbulence in the pulsing gas flow. It is likely that a factor analogous to the *CAF* is required in the calculation of the coefficient of mass transfer. A large acceleration of the mass transfer rate due to the high turbulence could limit the moisture effects to the period immediately after ignition. At this point in the test any temperature fluctuations caused by moisture effects would be indistinguishable from the temperature fluctuations caused by the initial instability in the speed and load as the engine starts up. That the experimental results are better represented by the 'dry' model does suggest that the moisture effects in the pipe sections of the exhaust system have little influence on the transient gas temperatures upstream of the catalytic converter.

In the catalytic converter the moisture effects are much more pronounced. The dominant processes are the homogeneous condensation and the evaporation. Heterogeneous condensation occurs but is less influential. The homogeneous condensation produces a significant amount of liquid which rapidly evaporates. This evaporation process occurs too quickly for an equilibrium saturation condition to be maintained in the gas, which causes an increase in the gas mixture temperature. The higher gas temperature further increases the evaporation rate eventually resulting in the gas temperature spike. The effects of the two types of condensation and evaporation in the catalytic converter are now considered individually.

It was found that although the temperature profiles in the catalytic converter were not very sensitive to the heterogeneous condensation rate, a significant reduction or removal of the heterogeneous condensation caused a delay in the time at which the gas temperature spike occurred. This delay is due to the reduction in the heat transfer (associated with the heterogeneous condensation) to the wall. The resulting cooler wall delays the evaporation of the liquid.

In the catalytic converter the bulk gas temperatures reach low enough levels for the homogenous condensation to become the dominant cause of liquid formation. The model used for this type of condensation assumes that when a super-saturated condition is reached due to cooling in the bulk gas, all excess vapour condenses into droplets. These condensate droplets then move immediately onto the wall. In reality the condensation mass transfer rate is likely to be lower as the condensate droplets will take a finite time to reach the walls.

In order to investigate the effect of the rate of condensation, the rate was adjusted by reducing the amount of excess vapour that condensed. As observed with the heterogeneous condensation, the reduction in the homogeneous condensation rate delays the onset of the plateau. A decrease in the temperature at which the temperature plateau occurred was also observed. For example, at position 3 in the low load case of ES1, a reduction of the homogeneous condensation rate by a factor of 100 lowered the plateau temperature from approximately 75 to 65 °C.

The onset of the plateau was also delayed, occurring at 30 s instead of the 25 s seen in Figure 6.5. The lowering of the plateau temperature at low condensation rates is due the higher vapour concentration remaining in the gas mixture. The higher vapour pressure has a lower saturation temperature, so a lower plateau temperature is observed. If the homogeneous condensation was removed completely, the gas temperatures did not step up to the plateau temperature due to the reduction in the rate of heat transfer to the walls. The gas temperature spike was also eliminated because the liquid mass available for evaporation was too low. Instead the same gradual rise as was seen in the 'dry' case occurred.

In order to try to reduce the non-equilibrium nature of the evaporation process, the influence of varying the rate of evaporation was investigated. It was found that a reduction of the evaporation rate by half produced only a minor change in the results, being that the spike occurred slightly later and was lower and broader. The temperature at which the plateau occurred was unaffected by this change. This implies that the peak value of the temperature spike does not influence the plateau temperature if the total mass of liquid moving into the gas mixture remains unchanged. A reduction of the evaporation rate by a factor of 10 eliminated the gas temperature spike completely, but as was observed when the condensation was reduced, no step up to the plateau temperature occurred.

Both condensation of vapour and evaporation of liquid are therefore needed in order to model the step up to the plateau. The challenge when numerically modelling the moisture effects is to accurately predict the amount of condensation occurring and the subsequent rate of evaporation that produces the smooth but rapid step up to the plateau temperature observed in the experimental results.

#### 7.3.3.3 Effect of an Initial Mass of Liquid in the Catalytic Converter

The results discussed previously were all generated using simulations that had an initially dry catalytic converter monolith. However, due to the natural affinity of the ceramic for absorbing moisture from atmospheric air, it is likely that there will be some water initially present in the monolith material during a cold start. Clarkson and Benjamin (1995) determined an approximate initial water mass of 10 kg-water/$m^3$ in the ceramic monolith by measuring the weight change in a monolith that had been dried by heating and was then allowed to stand for 24 hours in atmospheric air.

The effect of the presence of an initial mass of liquid on the numerical simulation results was investigated, but was found to be small compared to the moisture effects due to condensation. The temperature effect due to the presence of the initial moisture mass was isolated by removing condensation from the simulation, thereby allowing only the evaporation of the moisture already present. The gas and wall temperatures obtained from this simulation at positions 3 and 4 are shown in Figure 7.7, with the experimental results also plotted.

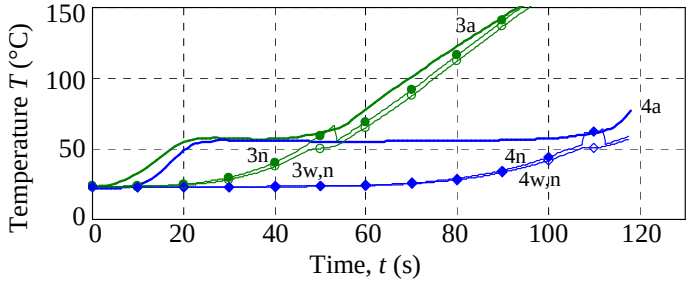


3: Catalytic Converter Mid-Bed (a) Measured, Unshielded Sensor, (n) Simulated
4: Catalytic Converter Outlet (a) Measured, Unshielded Sensor, (n) Simulated
3w,n: Catalytic Converter Mid-Bed Wall, Simulated
4w,n: Catalytic Converter Outlet Wall, Simulated

**Figure 7.7 Gas and Wall Temperatures in the Catalytic Converter for the Evaporation of an Initial Mass of Liquid**

The gas temperatures are very similar to the results obtained from the 'dry' model shown in Figure 7.5 (i). As the initial liquid mass evaporates the gas temperature rises slightly, causing a small peak at 50 s at position 3 and at 110 s at position 4. In this case the rate of evaporation is lower than in the full moisture model simulation because the vapour content of the gas mixture has not been reduced by condensation processes. It is still sufficient to cause the slight rise in the gas temperature. As the vapour rich gas moves downstream the temperature at each position decreases again. During the approximately 5 s period of evaporation, the wall temperatures at both positions exhibit brief plateaus (also lasting approximately 5 s).

The plateaus at both positions occur at the same temperature (50 °C), which is lower than those in the simulation with the full moisture model and even slightly lower than the experimentally measured plateau temperatures (at 53 °C). This is consistent with the earlier observation made that a higher vapour pressure causes a lower plateau temperature, since the vapour pressure has not been reduced at all by condensation and the addition of vapour as the initial liquid mass evaporates also occurs. The plateaus are reached much later than those in the simulation with all moisture effects included, as well as in the experimental results, which is consistent with the delay in rise to plateau temperature observed when the rates of both types of condensation and the evaporation are reduced.

From these discussions it is apparent that the early rise to the plateau temperature will not occur unless a significant amount of condensation occurs. This condensation produces a higher rate of heat transfer to the wall, and facilitates the rise in the gas temperature when the liquid later evaporates into the gas mixture.

## 7.4 Conclusions Regarding Moisture in the Exhaust System

The lengthy discussions of Section 7.3 were performed in order to try to fully understand the complex phenomena occurring in the exhaust system and the way in which they are captured by the numerical simulation. In this section the core observations regarding the moisture behaviour from Section 7.3 are summarised

and used to draw conclusions regarding the actual behaviour of the moisture in the exhaust system. The original hypothesis of this research, as stated in the introduction, is then assessed in light of these conclusions.

### 7.4.1 Conclusions Regarding the Actual Moisture Behaviour

In summary of Section 7.3, it was observed that both types of condensation cause warming of the system walls. In the catalytic converter the increased heat transfer caused by condensation contributes to the step up to the plateau temperature, but is not sufficient to produce the step if evaporation is not also present. In the model the evaporation process occurs in a non-equilibrium manner and causes warming of the gas. The effect of this warming is minor in the pipe sections but produces the severe temperature spike in the catalytic converter at the onset of the plateau.

It was further observed that the level at which the plateau occurs is determined by the vapour pressure in the gas mixture. In the general numerical simulation results the plateau temperatures were higher than the experimental plateaux due to the under-prediction of the vapour mass by the volumetric flow rate approximation method. In the variation of the simulation in which condensation was omitted and an initial mass of liquid was evaporated the bulk vapour pressure was higher. In this case a brief plateau was observed at a lower level then the experimental results.

In the actual exhaust system the combined effects of condensation and evaporation can be explained by the gas mixture striving towards an equilibrium saturation condition, which is reached when the plateau temperature is achieved. While the bulk gas temperatures are low, the condensation increases the rate of heat transfer to the walls and decreases the vapour content of the gas. The lower vapour pressure and rising incoming gas temperature combine to create conditions favourable for evaporation. If this occurs at a higher rate than required to produce a perfectly saturated condition, the gas will be warmed slightly. As the gradient of the incoming gas temperature begins to decrease, the system approaches the equilibrium condition, and the temperature settles at the saturated temperature of the incoming vapour.

The moisture behaviour in the actual catalytic converter is therefore concluded to be a combination of condensation and evaporation occurring simultaneously and in a non-equilibrium manner, during the early stages of the warm–up of the system. The liquid formed by this condensation does not accumulate and then evaporate in a single, sudden event the start of the plateau as it does in the simulation. Instead a large number of micro-evaporation events occur, spread over the approximately 15 s period leading up to the plateau (in which condensation also occurs). In this way the fast but smooth rise to the plateau at the saturated temperature of the incoming vapour is achieved.

In the pipe sections upstream of the catalytic converter the moisture behaviour predicted by the simulation was found to have little influence on the gas or wall

temperatures. Furthermore it was found that the temperatures predicted by the simulation in which the moisture effects were neglected produced a better correlation to the experimental results. It is possible that the condensation and evaporation processes do not occur at all in the upstream sections of the exhaust system, and that the moisture model used is inappropriate. Another possibility is that the moisture effects are limited to the very early stages of the test period where the ignition noise in the experimental data would obscure any effects the moisture might have. In either case it is concluded that the moisture has little influence on the transient temperatures in the pipe sections of the exhaust system.

### 7.4.2 Evaluation of Original Hypothesis

The original hypothesis of this research proposed that during a cold start the two-phase behaviour of the product water in the exhaust gases water influences the warm up characteristics of the exhaust system in the section between the exhaust port and the catalytic converter outlet. Furthermore it proposed that the evaporation of liquid present in the catalytic converter causes a delay in the time it takes for the catalytic converter to reach light-off conditions.

From the discussions of the moisture model behaviour and the conclusions regarding the real moisture behaviour it is determined that the first statement in the hypothesis is valid. The moisture plays a significant role in the warm-up behaviour of the catalytic converter and has been confirmed to be the cause of the measured temperature plateau. The moisture effects are not, however, considered to be relevant to the system temperatures upstream of the catalytic converter inlet.

Whether the second statement in the hypothesis, regarding the effect of the moisture on the time taken for the catalytic converter to reach light off, is valid is less clear. The evaporation of the liquid has been shown to cause a pause in the warm-up of the walls at low evaporation rates, as indicated by the brief plateaus in the wall temperatures in Figure 7.7. However, the increased heat transfer to the walls due to condensation and the warming of the gas due to non-equilibrium evaporation counteract the pause in wall temperature rise caused by low evaporation rates. The temperature plateau in the experimental results was originally believed to be an indication of the length of the delay caused by the evaporation, but it was found that the duration of the plateaus in the simulated results does not correspond to the duration of the evaporation occurring in each case.

The simulated temperature plateaus last approximately as long as the experimentally measured plateaus, but in the simulation the liquid evaporates completely some time before the gas temperatures start to rise from the plateau. This indicates that the plateau length is influenced more by the thermal capacity of the monolith walls than by the evaporation process. It is also noted that the gas temperatures obtained from the moisture inclusive simulation, the ‘dry’ simulation and the experimental investigation all reach approximately the same value at the

end of the time period. It is therefore concluded that although the moisture effects do influence the profile of the temperatures in the catalytic converter, they do not produce a significant delay in the warm-up time of the system.

In light of all the preceding discussions, some recommendations can now be made as to how the moisture model and the numerical simulation as a whole can be refined for future research.

## 7.5 Recommendations for the Numerical Simulation

The numerical simulation presented in this research serves as an investigation into which elements of the moisture behaviour have the most influence on the transient temperatures in the exhaust system during a cold start. Recommendations are made as to which aspects of the current numerical simulation are beneficial and which need further refinement so that an improved simulation can be created.

The division of the system into gas, liquid and wall control volumes is a simple but effective way of being able to model the thermodynamic effects of the liquid vapour phase change as well as predict the amount and position of liquid formation. Being able to track the liquid mass through the system over time is a useful tool when analysing the moisture effects and which is not included in other models reported in literature. It is therefore recommended that the fundamental approach to the solution and the structure of the simulation control volumes is maintained in future versions of the simulation.

In the current simulation heterogeneous and homogeneous mass transfer are accounted for separately. It is recommended that this method be maintained, as the current simulation results indicate that both these types of mass transfer are expected to occur. The refinement of the models for evaporation and homogeneous condensation is a key area for the improvement of the simulation as these are the dominant moisture related processes in the catalytic converter. In the current simulation both these processes occur very rapidly, resulting in sudden changes in liquid and vapour mass and temperature. Refinement of the homogeneous condensation rate could be achieved by the inclusion of a droplet deposition model. The evaporation and heterogeneous condensation models should be adapted to include the influence of factors such as the enhanced turbulence due to the pulsing exhaust flow. Physical properties of the exhaust system may also play a role in determining the evaporative mass transfer rates. For example, the porosity of the catalytic converter wall could reduce the evaporation rate if liquid absorbed by the walls needs to diffuse to the surface before evaporation can occur.

The temperature spike in the catalytic converter would also be reduced by the use of a numerical method other than the $K_V$ method, described in Section 3.3, to calculate the bulk gas mixture flow rate in the system. The $K_V$ method was used in order to solve the momentum equation, but resulted in inaccurate predictions of the vapour mass in the control volumes, to which the moisture model was found

to be sensitive (as discussed in Section 7.3). The simulation results have shown that variables such as the pressure drop in the system and the movement of the liquid layer have little influence on the resulting temperatures. It is therefore recommended that the pressure drop be either estimated or neglected and that the liquid layer be treated as stationary. The momentum equation can then be used to solve for the volumetric flow rate instead of having to make use of the $K_V$ approximation.

In Section 7.2 recommendations were made regarding the design of a simplified experimental setup in order to reduce the number of unknown or uncontrollable variables encountered in an actual engine system. The refinement of the mass transfer models would be facilitated by the construction of a numerical model representing this simplified experimental system. Variables should be added or adjusted concurrently in both experiment and simulation, for example adding a pulsing input flow or increasing the vapour content of the gas mixture. The effect of each change and the validity of the method of modelling it can then be better judged.

The recommendations made so far have been with the aim of creating an effective method of modelling the moisture behaviour on a macro-scale. However, the conclusions drawn regarding the real moisture behaviour suggest that in order to fully model the mass transfer a micro-scale model is required. In the micro-timescale factors such as the compressibility of the gas, pressure pulses in the gas flow due to the valve cycle and droplet nucleation and growth rate would become relevant. Such a fine study of this topic is not the goal of the current research, but the creation of a micro-scale model could potentially provide insight into which of the flow parameters are most influential on the macro-scale temperature profiles.

# 8 Conclusion

The purpose of this research was to investigate the behaviour of moisture in the exhaust system of an IC engine, during a cold start, in order to determine the influence of two phase moisture effects on the transient temperature behaviour during warm-up of the exhaust system. Particular emphasis was placed on the warm-up of the catalytic converter, where the moisture effects were postulated to be responsible for a plateau in the temperature profile. The possibility that the presence of this plateau caused a delay in the time taken for the catalytic converter to reach light-off conditions was investigated.

In order to predict the transient temperatures in the exhaust system, as well as the occurrence of any two phase mass transfer, a one dimensional mathematical model of the thermo-fluid behaviour in the system from exhaust port to the catalytic converter exit was created. In order to evaluate the simulation results an experimental investigation was performed in the engine test cells of Cape Advanced Engineering Pty (Ltd), Atlantis. Two separate engine systems, a 1.6 L Volkswagen Bora engine 1.6 L Ford RoCam, were used. The exhaust system of the RoCam engine did not contain a catalytic converter, but had three manifolds of different thermal mass available for use.

As the experimentally measured temperatures are used to evaluate the performance of the numerical simulation, a radiation shielded sensor with a small thermal mass was designed, manufactured and installed in both experimental setups. The goal of the design was to improve the accuracy and response time of the sensor compared to the thermocouples conventionally used in engine testing applications. For comparative purposes the conventional thermocouples were also installed in the system, at the same positions as the shielded sensors. The experimental results showed that the shielded sensors measured temperatures up to 50 °C higher than the conventional thermocouples and showed the desired improvement in response time.

In order to evaluate the accuracy of the shielded sensors the theory governing insertion errors experienced when measuring temperature in a flowing gas was used to create a true gas temperature prediction algorithm. This algorithm was applied to the measurements taken by both types of sensors in the takedown section of the exhaust system. The true gas temperatures predicted from both measurements were approximately the same and very close to the temperature measured by the shielded sensor. This indicates that the desired improvement in accuracy was also achieved.

The experimental results from the Bora engine setup clearly show the temperature plateau at the catalytic converter mid-bed and outlet. The plateau occurred at approximately 53 °C for all three load cases. The duration of the plateau decreased as the engine load increased, and was longer at the catalytic converter outlet than at the mid-bed. This indicates that the duration of the plateau was

influenced by both the mass flow rate through the exhaust system and the temperature of the exhaust gases. The influence of the mass flow rate was found to be larger than that of the temperature.

The experimental results from the RoCam setup showed that a change in thermal mass brought about by changing the manifold material from cast iron to stainless steel produced negligible variation in the downstream gas temperatures. The more significant reduction in the thermal mass obtained by using a manifold with a reduced wall thickness produced an increase in the downstream gas temperatures.

The relative change in the experimental gas temperatures with a change in load or manifold in the pipe sections was also exhibited in the numerical results. In the pipe sections upstream of the catalytic converter the most dominant factor influencing the temperature of the gas and walls is the convective heat transfer. In the manifold and takedown pipes the gas flow fluctuates significantly due to the exhaust valve cycle. As a result the turbulence levels in the pipes are higher than would be expected for a steady flow of the same average mass flow rate. The convective heat transfer predicted by conventional methods is therefore also too low. An enhanced turbulence Nusselt correlation was used in the model, in combination with a Convective Augmentation Factor (*CAF*), to represent the real heat transfer rate. The value of the *CAF* is dependent on the physical characteristics of the exhaust system and is determined by comparison of numerical and experimental results. The *CAF* values found to be applicable to this research varied between 0.7 and 1.5. These are reasonable values when compared to those reported in literature. The effect of moisture on the temperatures in the pipe sections was found to be of little consequence compared to the convective heat transfer rate.

The numerical simulation results for the catalytic converter also exhibit a temperature plateau. However, at the onset of the plateau a sharp spike in the simulated gas temperatures, that is not present in the experimental results, was observed. After this spike the simulated temperatures drop down to plateau temperatures that are in the order of 15 °C higher than the experimental plateaux. The duration of the experimental plateaux were well represented by the simulation plateaux for all load cases.

In order to gain an understanding of the moisture model behaviour the effects of the homogeneous condensation, heterogeneous condensation and evaporation were individually investigated. It was observed that both types of condensation cause warming of the system walls. The increased heat transfer caused by condensation contributes to the step up to the plateau temperature, but was found to be insufficient to produce the step if evaporation is not also present.

In the model the evaporation process occurs in a non-equilibrium manner and causes warming of the gas. The warming caused by the sudden evaporation of the accumulated liquid in the catalytic converter is the cause of the severe temperature

spike at the onset of the plateau. It was further observed that the level at which the plateau occurs is determined by the vapour pressure in the gas mixture. The difference in plateau temperatures between the simulated and experimental results is attributed to the under-estimation of the total gas mixture mass in the control volumes by the gas flow rate model. The lower mass results in a lower vapour pressure and a correspondingly higher saturation temperature.

From a comparison of this modelled behaviour and the experimental results it is concluded that moisture behaviour in the real catalytic converter is a combination of condensation and evaporation occurring in the early stages of the warm–up of the system. The liquid formed by this condensation does not accumulate and then evaporate in a single, relatively sudden event the start of the temperature plateau (as it does in the numerical simulation). Instead, in reality a large number of micro-evaporation events occur during the period in which the condensation is also occurring. In this way the fast but smooth rise to the plateau at the saturated temperature of the incoming vapour is achieved.

In the original hypothesis of this research it was proposed that the temperature plateau in the experimental results was an indication of the length of the delay in the warm-up of the catalytic converter caused by the evaporation. The simulation results indicate that the duration of the plateau does not correspond to the duration of the evaporation period. It was also found that the final temperature results obtained from the simulation in which the moisture effects were included and a simulation in which the moisture effects were neglected were comparable. From this it is concluded that although the behaviour of the moisture has a strong influence on the warm-up temperature profile of the catalytic converter, this behaviour is not expected to delay the light-off of the catalyst.

In final conclusion, the one dimensional model developed in this research provides insight into the behaviour of moisture in the exhaust system of an IC engine during a cold start. Although the model is relatively simple and requires refinement in a number of areas, the results obtained allowed predictions to be made of the time, position and duration of liquid formation in the exhaust system. The research presented here therefore provides useful groundwork for a more complex study of the influence of the two-phase moisture behaviour on the transient temperatures in the exhaust system.

# 9 Recommendations

In order to advance the understanding of the moisture behaviour in the exhaust system, recommendations for future experimental and theoretical work are made. These recommendations include the refinement of the design of the shielded temperature sensor, the refinement of the numerical simulation by comparison to a systematically built up experimental setup and, finally, the inclusion of the moisture behaviour model into a comprehensive CFD code.

The shielded sensor designed during this research allowed accurate and responsive temperature measurements to be taken in the takedown section of the exhaust system. However, the shielded sensors had an upper operational temperature limit that prevented them from being used at the exhaust port. This proved to be a disadvantage during the construction of the numerical simulation as the incoming flow temperature was less accurately measured by the conventional thermocouples at the port. In Section 7.1 a redesign of the shielded sensor was proposed in order to increase its robustness without significantly reducing its accuracy and temperature response time. It is recommended that this redesigned sensor be manufactured and its performance assessed. The sensor can then be used to provide more accurate input temperatures for the numerical simulation.

An algorithm was constructed using insertion error theory to predict the true gas temperature from the measurements in the takedown pipe and was shown to be accurate for these sections. The validity of using this algorithm to predict the true port temperatures could not be verified due to the difference in the flow conditions prevailing at the port and takedown sections. It is therefore recommended that the redesigned shielded sensor measurements be compared to the conventional thermocouple measurements over a range of conditions prevailing in the exhaust system. From this comparison the variation in the insertion errors associated with the conventional thermocouples can be quantified as a function of exhaust flow conditions. Accurate predictions of true gas temperatures could then be made in situations in which the shielded sensors cannot be used.

In Sections 7.2 and 7.5 recommendations were made regarding the simultaneous construction of a numerical simulation and an experimental setup from an initially very simplified case. It is recommended that this procedure be performed so that the influence of each flow variable on the moisture behaviour can be determined. Particular emphasis should be placed on the influence of flow rate, moisture content of the bulk gas and pulsing vs steady flow conditions. Additional factors such as initial liquid present in the catalytic converter wall and the porosity of the monolith ceramic should also be investigated. The conditions in the exhaust system that were determined from the experimental work in this research could be used as a guideline for appropriate conditions in the simplified experimental setup. From this systematic study a reliable moisture model specific to exhaust gas flow conditions should be created and applied to the numerical simulation

here. This numerical simulation could then be elaborated into a two dimensional model in which such factors as the exhaust system wall geometry and flow distribution in the catalytic converter are accounted for.

The final recommendation leading from this research would be to incorporate the relevant two phase moisture model in to an existing comprehensive CFD code representing the catalytic converter. This method was used with success by Clarkson and Benjamin (1995). The behaviour of the moisture in combination with the exothermic reactions could then be studied and final conclusions regarding its influence made.

# 10 References


Abu-Qudais M, Instantaneous exhaust gas temperature and velocity for a diesel engine, *Applied Energy*, Vol 56, No1, pp 59-70, 1997

Bally JW, Riley WF and McConnel KG, *Instrumentation for Mechanical Measurements*, Second Edition, Wiley, 1993

Batty JC and Folkman SL, *Food Engineering Fundamentals*, Wiley, 1983

Beckwith TG, Marangoni RD and Lienhard JH, *Mechanical measurements*, Fifth Edition, Addison Westley, 1993

Benjamin S, Simulating the performance of automotive catalytic converters, *Business Briefing: GlobalAutomotive Manufacturing and Technology*, pp 1-5, 2003

Bird RB, Stewart WE and Lightfoot EN, *Transport Phenomena*, Wiley, 1960

Blint JR and Haworth DC, Modelling oxidation of exhaust gasses diluted by air under exhaust manifold conditions, *Proceedings of the Combustion Institute*, Vol 28, pp 2451-2457, 2000

Burch SD, Keyser MA, Colucci CP, Potter, TF and Benson DK, Applications and benefits of catalytic converter thermal management, *SAE Paper* 961134, 1996

Carey VP, *Liquid-Vapour Phase Change Phenomena*, Hemisphere Publishing Corporation, 1992

Cavina N, Measurement of exhaust gas temperatures: Theoretical and experimental analysis, *Design, Application Performance and Emissions of Modern Internal Combustion Engine Systems and Components, ICE* Vol 39, ICEF2002-539, ASME, 2002

Çengel Y, *Heat Transfer: An Engineering Approach*, Second Edition, McGraw Hill, 2003

Çengel Y and Boles M, *Thermodynamics: An Engineering Approach*, Fourth Edition, McGraw Hill, 2002

Chan SH and Hoang DL, Heat transfer and chemical reactions in the exhaust system of a cold-start engine, *International Journal of Heat and Mass Transfer*, Vol 42, pp 4165-4183, 1999

Cho YS, Kim CR, Kim DS, Lee J, Lee SW, Myung KH and Choo JS, Prediction of exhaust temperatures at the inlet of an underbody catalytic converter during FTP-75 test, *Society of Automotive engineers*, Paper 972913, 1997

Clarkson RJ and Benjamin SF, Modelling the effect of moisture on catalyst warm-up, *Proceedings of the Institute of Mechanical Engineers/SAE VTMS2 Conference*, Paper C496/002, 9-12 May 1995

Depcik C and Assanis D, A universal heat transfer correlation for intake and exhaust flow in an spark-ignition internal combustion engine, *SAE Paper* 2002-01-0372, 2002

Ferguson CR and Kirkpatric AT, *Internal Combustion Engines*, Second Edition, Wiley, 2001

Incropera FP and DeWitt DP, *Fundamentals of Heat and Mass Transfer*, Fifth Edition, Wiley, 2002

Kelleners P, Simulation of compressible multi-phase flow with condensation, *Centre for Turbulence research: Annual Research Briefs*, pp 49-67, 2003

Kandylas IP and Stamatelos AM, Engine exhaust system design based on heat transfer computation, *Energy Conversion & Management*, Vol 40, pp 1057-1072, 1999

Koltsakis GC, Warm-up behaviour of monolithic reactors under non-reacting conditions, *Chemical Engineering Science*, Vol 52, no 17, pp 2891-2899, 1997

Koltsakis GC and Stamatelos AM, Modelling dynamic phenomena in 3-way catalytic converters, *Chemical Engineering Science*, Vol 54, pp 4567-4578, 1999

Konstantinidis PA, Koltsakis GC and Stamatelos AM, Transient heat transfer modelling in automotive exhaust systems, *IMechE Paper* C11395, 1997

Laing PM, Development of an alternator-powered electrically-heated catalyst system', *SAE Technical Paper* 932676, 1994

Marais JM, Transient thermal modelling of a motor vehicle exhaust system, *Unpublished Final Year BSc Eng Project*, University of Stellenbosch, 2004

Meisner and Sorenson, Computer simulation of exhaust manifold flow and heat transfer, *SAE Paper* 860242, 1986

Michalski L, Eckersdorf K and McGee J, *Temperature Measurement*, Wiley, 1991

Mills AF, *Heat and Mass Transfer*, Irwin, 1995

Mills AF, 'RAD3.exe', Gaseous radiation calculation program, http://mae.ucla.edu/academics/faculty/mills.htm, 2008

Potter MC and Wiggert DC, *Mechanics of Fluids*, Third Edition, Brooks/Cole, 2002

Siemund S, Leclerc JP, Schweich D, Prigent M and Castanga F, Three-way monolithic catalytic converters: Simulations versus experiments, *Chemical Engineering Science*, Vol 51, No 15, pp 3709-3720, 1996

Stull DR, Prophet H *et al.*, *JANAF Thermochemical Tables*, Second Edition, US Department of Commerce, National Bureau of Standards, 1971

UniTemp Product Catalogue, www.unitemp.com, 2008

Versteeg HK and Malalasekera W, *An Introduction to Computational Fluid Dynamics*, Prentice Hall, 1995

Wallis GB, Annular two-phase flow II: Additional Effects, *Journal of Basic Engineering*, Vol 92, pp 73-82, 1970

Wendland DW, Automobile exhaust-system steady-state heat transfer, *SAE Paper* 931085, 1993

Whalley PB, *Boiling, Condensation and Gas-Liquid Flow*, Oxford Science Publications, 1987

White F, *Viscous Fluid Flow*, Second Edition, McGraw-Hill, 1991

Wolfram Mathworld, Runge Kutta Method, http://mathworld.wolfram.com/Runge-KuttaMethod.html, 2009

# Appendix A: Experimental Data and Analysis Methods

This section gives further information regarding the experimental setups, the setup and calibration documentation and the procedure followed for the experimental data processing.

## A1 Exhaust System Dimensions and Properties

The dimensions and properties of the exhaust systems of both test setups are listed here. Test Setup 1 consisted of a VW Bora 1.6 L (gasoline) engine equipped with an exhaust system which contained a Volkswagen/Audi ceramic monolith catalytic converter. The properties of the exhaust system are given in Table A.1. The manifold and takedown pipe material properties listed are taken from Incropera and DeWitt (2002), and the catalytic converter properties from Koltsakis and Stamatelos (1999).

**Table A. 1 Exhaust Pipe and Catalytic Converter Properties for Experimental Setup 1**

| Property | Manifold | Takedown Pipe | Property | Catalytic Converter |
|---|---|---|---|---|
| Flow Path Length | 0.225 m | 0.45 m | Monolith Length | 0.2 m |
| Inner Diameter | 0.04 m | 0.04 m | Outer Diameter | 0.15 m |
| Wall Thickness | 0.008 m | 0.0025 m | Channel Wall Thickness | 0.0001 m |
| - | - | - | Channel Width | 0.001 m |
| Material | Cast Iron | Stainless Steel | Material | Ceramic (cordierite) |
| Thermal Capacity | 447 J/kgK | 480 J/kgK | Thermal Capacity | 1020 J/kgK |
| Thermal Conductivity | 72 W/mK | 15 W/mK | Thermal Conductivity | 1.5 W/mK |
| Density | 7870 kg/m$^3$ | 8000 kg/m$^3$ | Density | 1550 kg/m$^3$ |

Experimental Setup 2 consisted of a Ford RoCam 1.6 L (gasoline) engine with no catalytic converter in the exhaust system. Three manifold options were available. The properties of the exhaust system with each manifold option are given in Table A.2.

**Table A. 2 Exhaust Pipe Properties for Experimental Setup 2**

| Property | Manifold 1 | Manifold 2 | Manifold 3 | Takedown Pipe |
|---|---|---|---|---|
| Flow Path Length | 0.330 m | 0.330 m | 0.330 m | 0.5 m |
| Inner Diameter | 0.04 m | 0.04 m | 0.04 m | 0.04 m |
| Wall Thickness | 0.0045 m | 0.0045 m | 0.0025 m | 0.0025 m |
| Material | Cast Iron | Stainless Steel | Stainless Steel | Mild Steel |
| Thermal Capacity | 447 J/kgK | 480 J/kgK | 480 J/kgK | 434 J/kgK |
| Thermal Conductivity | 72 W/mK | 15 W/mK | 15 W/mK | 64 W/mK |
| Density | 7870 kg/m$^3$ | 8000 kg/m$^3$ | 8000 kg/m$^3$ | 7830 kg/m$^3$ |

## A2 Experimental Setup Checklist and Calibration

The engine set-up check list procedure is shown in Figure A.1, the set-up details, listing the quantities measured, are shown in Figure A.2 and the calibration certificate for the test assembly is shown in Figure A.3. These documents were provided by the CAE technicians responsible for the operation of the test cell.

Stellenbosch Automotive Engineering (Pty) Ltd

**ENGINE SET-UP CHECKLIST**

| ENGINE BUILD | INITIAL TICK BOX PLEASE | | |
|---|---|---|---|
| | YES | NO | N/A |
| CORRECT CLUTCH PLATE, PRESSURE PLATE AND FLYWHEEL ASSEMBLY | ✓ | | |
| BELL HOUSING ADAPTOR ASSEMBLY SECURED | ✓ | | |
| THERMOSTAT REQUIREMENTS MET | ✓ | | |

| ENGINE ACCESSORIES | INITIAL TICK BOX PLEASE | | |
|---|---|---|---|
| | YES | NO | N/A |
| DRIVE BELT TENSIONED | ✓ | | |
| REQUIRED AUXILLIARIES (A/C, PAS, ALTERNATOR) FITTED SECURELY | ✓ | | |
| STARTER MOTOR SECURED AND BOLTS TORQUED | ✓ | | |

| ENGINE OIL | INITIAL TICK BOX PLEASE | | |
|---|---|---|---|
| | YES | NO | N/A |
| CORRECT MASS INTO ENGINE | ✓ | | |
| LEVEL CHECKED | ✓ | | |
| CORRECT DIPSTICK USED; LABELLED | ✓ | | |
| CORRECT WATER SUPPY TO COOLER (EXTERNAL OR ENGINE) - CORRECT FLOW DIRECTI | ✓ | | |
| TEMPERATURE CONTROLLER SET POINT CHECKED | ✓ | | |
| ALL OIL PRESSURE SENSORS FITTED | ✓ | | |
| ALL OIL TEMPERATURE SENSORS FITTED | ✓ | | |
| ALL MEASUREMENTS BOSSES NOT USED PROPERLY BLOCKED | ✓ | | |
| ALL FITTINGS AND BRAIDED HOSE TIGHTENED | ✓ | | |
| OIL FILLER CAP SECURED | ✓ | | |
| OIL FILTER TIGHTENED | ✓ | | |

| FUEL | INITIAL TICK BOX PLEASE | | |
|---|---|---|---|
| | YES | NO | N/A |
| CORRECT OCTANE SUPPLIED | | | |
| PROPER FUEL HOSE USED | ✓ | | |
| FUEL RAIL SUPPLY & RETURN CORRECTLY INSTALLED | ✓ | | |
| FUEL LINE INSPECTED FOR DAMAGE | ✓ | | |
| WORN OUT ENDS ON FUEL LINE TRIMMED WITH KNIFE BEFORE INSTALLATION | ✓ | | |
| FUEL LINE PROTECTED AGAINST CHAFING | ✓ | | |
| FUEL SYSTEM FLUSHED IF REQUIRED | ✓ | | |
| PUMP RAN TO CHECK FOR FUEL PRESSURE | ✓ | | |
| IF RUNNING FROM FUEL DRUM, IS DRUM CORRECTLY EARTHED (EARTH STRAP FITTED) | ✓ | | |
| FUEL PRESSURE FITTING TIGHTENED | ✓ | | |
| FUEL TEMPERATURE FITTING TIGHTENED | ✓ | | |
| FUEL PUMP SAFELY POSITIONED | ✓ | | |
| FUEL FILTER REPLACED | ✓ | | |

| COOLANT | INITIAL TICK BOX PLEASE | | |
|---|---|---|---|
| | YES | NO | N/A |
| COOLANT IN & COOLANT OUT CORRECTLY INSTALLED | ✓ | | |
| FLOW DIRECTION THROUGH AUXILARIES CHECKED - CABIN HEATER, THROTTLE BODY E | ✓ | | |
| CORRECT COOLANT USED | ✓ | | |
| COOLANT LEVEL CHECKED | ✓ | | |
| COOLANT SYSTEM BLED | ✓ | | |
| COOLANT BOTTLE CAP TIGHTENED | ✓ | | |
| COOLANT LINES INSPECTED FOR DAMAGE | ✓ | | |
| ALL PRESSURE SENSORS FITTED | ✓ | | |
| ALL TEMPERATURE SENSORS FITTED | ✓ | | |
| TEMPERATURE CONTROLLER SET POINT CHECKED | ✓ | | |

**Figure A.1 CAE Engine Set-Up Checklist**
**(best available electronic copy)**

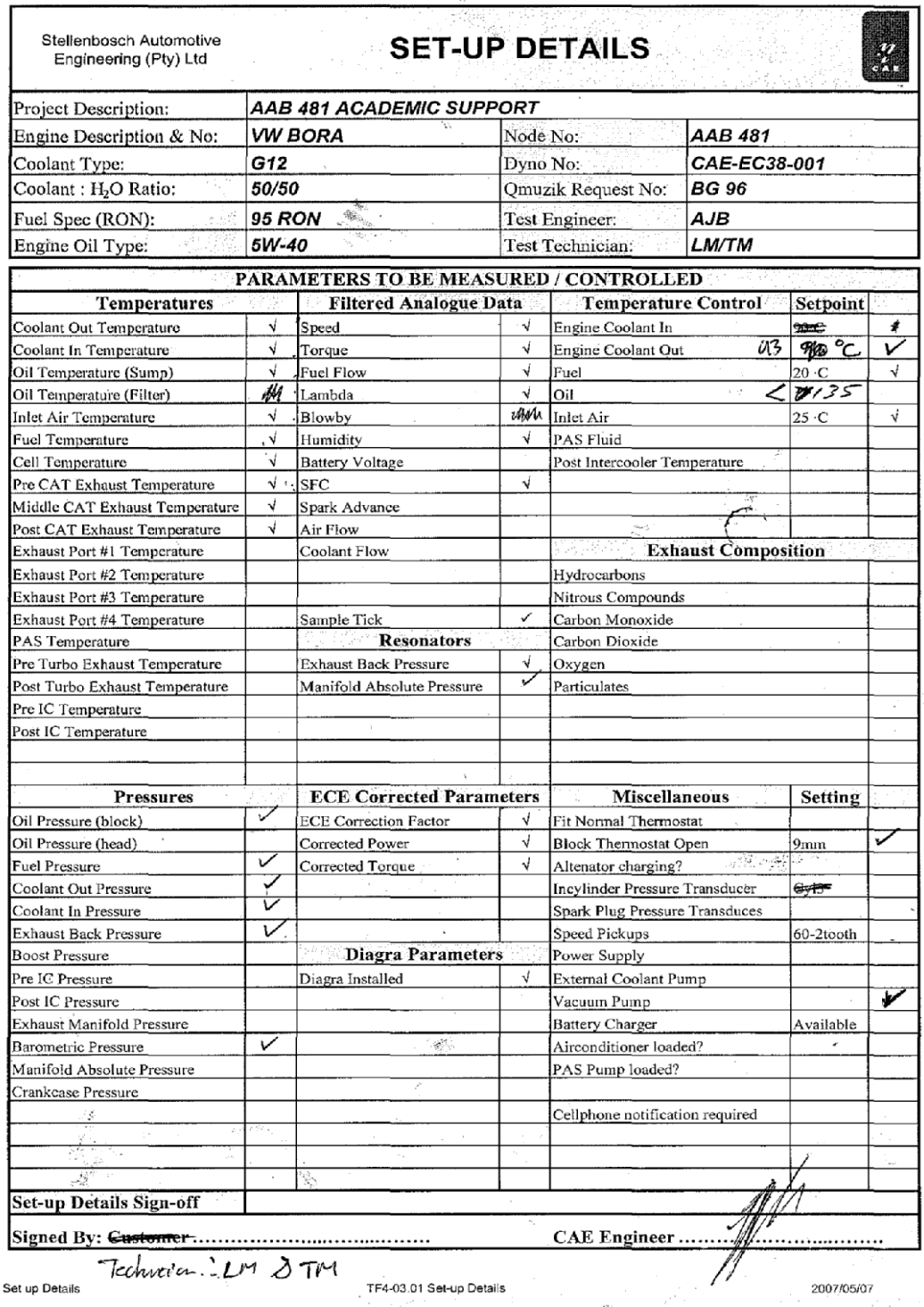

Stellenbosch Automotive Engineering (Pty) Ltd

# SET-UP DETAILS

| | | | |
|---|---|---|---|
| Project Description: | AAB 481 ACADEMIC SUPPORT | | |
| Engine Description & No: | VW BORA | Node No: | AAB 481 |
| Coolant Type: | G12 | Dyno No: | CAE-EC38-001 |
| Coolant : $H_2O$ Ratio: | 50/50 | Qmuzik Request No: | BG 96 |
| Fuel Spec (RON): | 95 RON | Test Engineer: | AJB |
| Engine Oil Type: | 5W-40 | Test Technician: | LM/TM |

**PARAMETERS TO BE MEASURED / CONTROLLED**

| Temperatures | | Filtered Analogue Data | | Temperature Control | Setpoint | |
|---|---|---|---|---|---|---|
| Coolant Out Temperature | √ | Speed | √ | Engine Coolant In | ~~20°C~~ | # |
| Coolant In Temperature | √ | Torque | √ | Engine Coolant Out | 103 ~~90~~ °C | ✓ |
| Oil Temperature (Sump) | √ | Fuel Flow | √ | Fuel | 20 °C | √ |
| Oil Temperature (Filter) | ~~√~~ | Lambda | √ | Oil | < ~~120~~ 135 | |
| Inlet Air Temperature | √ | Blowby | ~~√~~ | Inlet Air | 25 °C | √ |
| Fuel Temperature | √ | Humidity | √ | PAS Fluid | | |
| Cell Temperature | √ | Battery Voltage | | Post Intercooler Temperature | | |
| Pre CAT Exhaust Temperature | √ | SFC | √ | | | |
| Middle CAT Exhaust Temperature | √ | Spark Advance | | | | |
| Post CAT Exhaust Temperature | √ | Air Flow | | | | |
| Exhaust Port #1 Temperature | | Coolant Flow | | **Exhaust Composition** | | |
| Exhaust Port #2 Temperature | | | | Hydrocarbons | | |
| Exhaust Port #3 Temperature | | | | Nitrous Compounds | | |
| Exhaust Port #4 Temperature | | Sample Tick | ✓ | Carbon Monoxide | | |
| PAS Temperature | | **Resonators** | | Carbon Dioxide | | |
| Pre Turbo Exhaust Temperature | | Exhaust Back Pressure | √ | Oxygen | | |
| Post Turbo Exhaust Temperature | | Manifold Absolute Pressure | ✓ | Particulates | | |
| Pre IC Temperature | | | | | | |
| Post IC Temperature | | | | | | |
| | | | | | | |
| | | | | | | |

| Pressures | | ECE Corrected Parameters | | Miscellaneous | Setting | |
|---|---|---|---|---|---|---|
| Oil Pressure (block) | ✓ | ECE Correction Factor | √ | Fit Normal Thermostat | | |
| Oil Pressure (head) | | Corrected Power | √ | Block Thermostat Open | 9mm | ✓ |
| Fuel Pressure | ✓ | Corrected Torque | √ | Altenator charging? | | |
| Coolant Out Pressure | ✓ | | | Incylinder Pressure Transducer | ~~Cyl5~~ | |
| Coolant In Pressure | ✓ | | | Spark Plug Pressure Transduces | | |
| Exhaust Back Pressure | ✓ | | | Speed Pickups | 60-2tooth | |
| Boost Pressure | | **Diagra Parameters** | | Power Supply | | |
| Pre IC Pressure | | Diagra Installed | √ | External Coolant Pump | | |
| Post IC Pressure | | | | Vacuum Pump | | ✓ |
| Exhaust Manifold Pressure | | | | Battery Charger | Available | |
| Barometric Pressure | ✓ | | | Airconditioner loaded? | | |
| Manifold Absolute Pressure | | | | PAS Pump loaded? | | |
| Crankcase Pressure | | | | | | |
| | | | | Cellphone notification required | | |
| | | | | | | |
| | | | | | | |
| | | | | | | |

**Set-up Details Sign-off**

**Signed By:** ~~Customer~~ Technician: LM & TM ..... **CAE Engineer** .....

Set up Details TF4-03.01 Set-up Details 2007/05/07

**Figure A.2 CAE Engine Set-Up Details Listing Measured Values (best available electronic copy)**

Stellenbosch Automotive Engineering (Pty) Ltd

# CERTIFICATE OF CALIBRATION

| Project Node & Description: | AAB 481 ACADEMIC SUPPORT | | | | Set-up Request No: | BG 96 | Dyno No: | CAE-EC3 | Engine No: | 861_DUMMY | Test Engineer: | | AJB |
|---|---|---|---|---|---|---|---|---|---|---|---|---|---|
| **Channels to be Calibrated** | **Unit** | **Range of Instrument** | **Zero Applied** | **Zero Measured** | **Range Applied** | **Range Measured** | **ETA-Measured Value 1** | **ETA-Measured Value 2** | **ETA Output Value 1** | **ETA Output Value 2** | **PASS / FAIL** | **Initials of Calibrator** | **Comments** |
| **Analogue Channels** | | | | | | | | | | | | | |
| Speed | rpm | 0 - 6500 rpm | 0 | 0 | 6000 | | | | | | ✓ | Fluke | |
| Torque | Nm | 0 - 200 Nm | 0 | 0 | 157,113 | | | | | | ✓ | Weights | |
| Fuel_Mass | g | 600g / 900g | 0 | 0 | 120.0 | 120.0 | 35666 | 32767 | 118,8 | 6713 | ✓ | Weights | |
| V_Baro | V | 90 kPa - 110 kPa | 0 | 0 | 2.5 | 2,5 | 0 | 1 | 0 | 32767 | ✓ | Druck | |
| Lambda | | 0.69 - 1.67 | 0 | 0 | 1 | 1 | 0 | 1 | 0 | 32767 | | Druck | |
| Spark_Adv | ° | 0°-50° | 0 | 0 | 10 | 10 | 1 | 1 | 0 | 32767 | ✓ | Timing Light | |
| V_Batt | V | 0 - 20VDc | 0 | 0 | 10 | 15 | 0 | 1 | 0 | 1 | | Druck | |
| Humidity | % | 10% - 100% | 0 | 0 | 10 | 10 | 0 | 1 | 0 | 100 | ✓ | Druck | |
| Blow_By | l/min | 0-120 l/min | 0 | | 5 | | | | | | ✓ | | |
| **Temperature Channels** | | | | | | | | | | | | | |
| T_Cool_In | °C | 0°C-759°C | 0 | 0 | 100 | 100 | 0 | 1 | 0 | 1 | ✓ | Druck | |
| T_Cool_Out | °C | 0°C-759°C | 0 | 0 | 100 | 128 | 0 | 1 | 0 | 1 | ✓ | Druck | |
| T_Cool_Mix | °C | 0°C-759°C | 0 | | 100 | | 0 | 1 | 0 | 1 | | Druck | |
| T_Oil | °C | 0°C-759°C | 0 | 0 | 150 | 130 | 0 | 1 | 0 | 1 | ✓ | Druck | |
| T_Fuel | °C | 0°C-759°C | 0 | 0 | 30 | 30 | 0 | 1 | 0 | 1 | ✓ | Druck | |
| T_Air_In | °C | 0°C-759°C | 0 | 0 | 25 | 25 | 0 | 1 | 0 | 1 | ✓ | Druck | |
| T_Men | °C | 0°C-759°C | 0 | | 25 | | 0 | 1 | 0 | 1 | | Druck | |
| T_PAS | °C | 0°C-759°C | 0 | | 50 | | 0 | 1 | 0 | 1 | | Druck | |
| T_Exh | °C | 0°C-1359°C | 0 | | 900 | | 0 | 1 | 0 | 1 | | Druck | |
| T_Port 1 | °C | 0°C-1359°C | 0 | | 900 | | 0 | 1 | 0 | 1 | | Druck | |
| T_Port 2 | °C | 0°C-1359°C | 0 | | 900 | | 0 | 1 | 0 | 1 | | Druck | |
| T_Port 3 | °C | 0°C-1359°C | 0 | | 900 | | 0 | 1 | 0 | 1 | | Druck | |
| T_Port 4 | °C | 0°C-1359°C | 0 | | 900 | | 0 | 1 | 0 | 1 | | Druck | |
| T_Dyno_B1 | °C | 0°C-1359°C | 0 | | 60 | | 0 | 1 | 0 | 1 | | Druck | |
| T_Dyno_B2 | °C | 0°C-1359°C | 0 | | 60 | | 0 | 1 | 0 | 1 | | Druck | |
| T_Dyno_B3 | °C | 0°C-1359°C | 0 | | 60 | | 0 | 1 | 0 | 1 | | Druck | |
| T_Dyno_LP1 | °C | 0°C-1359°C | 0 | | 180 | | 0 | 1 | 0 | 1 | | Druck | |
| T_Dyno_LP2 | °C | 0°C-1359°C | 0 | | 180 | | 0 | 1 | 0 | 1 | | Druck | |
| T_Pre_Cat | °C | 0°C-1359°C | 0 | 0 | 900 | 400 | 0 | 1 | 0 | 1 | ✓ | Druck | |
| T_Cat | °C | 0°C-1359°C | 0 | 0 | 900 | 904 | 0 | 1 | 0 | 1 | ✓ | Druck | |
| T_Pre_Cat | °C | 0°C-1359°C | 0 | 0 | 900 | 406 | 0 | 1 | 0 | 1 | ✓ | Druck | |
| **Pressure Channels** | | | | | | | | | | | | | |
| P_Fuel | Bar | 0 Bar - 10 Bar | 0 | 0 | 5.0 | 5000 | 32717 | 9814 | 0 | 5000 | ✓ | Keller | |
| P_Oil | Bar | 0 Bar - 10 Bar | 0 | 0 | 5.0 | 3000 | 32768 | 9824 | 0 | 1000 | ✓ | Keller | |
| P_Oil_Head | Bar | 0 Bar - 10 Bar | 0 | | 5.0 | | | | | | | Keller | |
| P_Cool_In | Bar | 0 Bar - 2.5 Bar | 0 | 0 | 2.5 | 1500 | 32767 | 16348 | 0 | 2500 | ✓ | Keller | |
| P_Cool_Out | Bar | 0 Bar - 2.5 Bar | 0 | 0 | 2.5 | 2000 | 32768 | 16240 | 0 | 2500 | ✓ | Keller | |
| P_Sump | Bar | -0.5 Bar - 0.5 Bar | 0 | | 0.5 | | | | | | | Keller | |
| P_Exh | mBar | 0 mBar - 2.5 mBar | 0 | 0 | 2.5 | 1700 | 16691 | 17935 | 0 | 2500 | ✓ | Keller | |
| P_Man | mBar | -1 mBar - 0 mBar | 0 | 2,3 | -80.0 | 900 | 5835 | 16346 | 1000 | 800 | ✓ | Keller | |
| **Other** | | | | | | | | | | | | | |
| Bosch Smoke Meter | | | | | | | | | | | | | |
| **Calibration Checked By:** | | | | | **Signature:** | | | | | | **Date:** | | 01/05/2007 |

ATL 06 TEST SHEETS TF4-04.01CalibrationCertificate 2007/05/04

**Figure A.3 Calibration Certificate for the CAE Test Cell Assembly**
**(best available electronic copy)**

## A3 Error Analysis

An example of the procedure used to determine the probability distribution in the experimental data is performed using the measurements taken by the shielded sensor at the takedown pipe inlet at the high load of ES2 (using the standard cast iron manifold). Four test runs were performed for this test configuration and the temperatures corresponding to the time $t$ = 100 s, as listed in Table A.3, are used.

**Table A.3 Measured Takedown pipe Inlet Gas Temperatures (Shielded Sensor) at t = 100 s for the High Load Case of Experimental Setup 2**

| Test Run | 1 | 2 | 3 | 4 |
|---|---|---|---|---|
| Temperature (°C) | 413.437 | 397.841 | 405.561 | 404.032 |

The four test runs provide a sample number $n$ = 4, so the $t$-distribution appropriate for small samples ($n$ < 30) (Beckwith *et al.*, 1993) is applied. The sample mean

$$\bar{x} = \sum_{i=1}^{n} \frac{x_i}{n} = \frac{(413.437 + 397.841 + 405.651 + 404.032)}{4} = 405.218 \ ^\circ\text{C} \qquad \text{A.1}$$

is used as an approximation of the true mean. The sample standard deviation is an approximation of the true standard deviation of an infinite sample population and is given by:

$$S_x = \sqrt{\frac{\left(\sum_{i=1}^{n} x_i^2 - n\bar{x}^2\right)}{(n-1)}} = \sqrt{\frac{\left(413.437^2 + 397.841^2 + 405.561^2 + 404.032^2 - 4\left(405.218^2\right)\right)}{(4-1)}} = 6.416 \ ^\circ\text{C} \qquad \text{A.2}$$

The true mean $\mu$ can then be said, with $c$% confidence, to fall within the interval

$$\bar{x} - t_{\alpha/2,v}\frac{S_x}{\sqrt{n}} < \mu < \bar{x} + t_{\alpha/2,v}\frac{S_x}{\sqrt{n}} \qquad (c\%) \qquad \text{A.3}$$

where $\alpha = 1 - c, v = n - 1$. The value of $t_{\alpha/2,v}$ is taken from tabulated values in Beckwith *et al*. (1993). For the 95% confidence interval:

$c = 0.95$

$\alpha = 1 - 0.95 = 0.05$

$v = n - 1 = 3$

$t_{\alpha/2,v} = t_{0.025,3} = 3.182$

The precision uncertainty $P_x$ for this interval is now:

$$P_x = t_{\alpha/2,\nu}\frac{S_x}{\sqrt{n}} = 3.182\frac{6.416}{\sqrt{4}} = 10.208\ ^\circ\text{C} \qquad \text{A.4}$$

The true mean can then be said, with $c$% confidence, to fall within the interval:

$$\bar{x} - P_x < \mu < \bar{x} + P_x \qquad (c\%)$$

$$405.218 - 10.208 < \mu < 405.218 + 10.208 \qquad (95\%)$$

$$395.010 < \mu < 415.526 \qquad (95\%)$$

The procedure above was performed in Microsoft Excel (2003) for each data set over the period of the test run. As there are many data points for each measured temperature, the average of the 95% uncertainty bounds over the whole period for each measurement is taken. In Figure A.4 the averaged gas and wall temperatures for the high load case of ES2 are shown. The error bars on each plotted measurement indicate corresponding average 95% confidence interval.

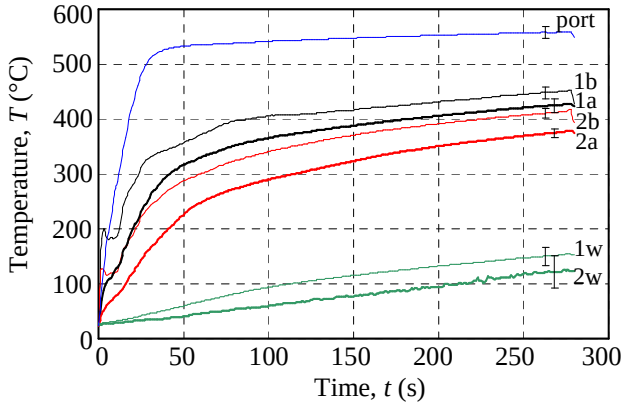


1: (a) Takedown Pipe Inlet, Unshielded Sensor, (b) Takedown Pipe Inlet, Shielded Sensor
2: (a) Takedown Pipe Outlet, Unshielded Sensor, (b) Takedown Pipe Outlet, Shielded Sensor
1w: Takedown Pipe Inlet Wall, 2w: Takedown Pipe Outlet Wall

**Figure A.4 Average Gas and Wall Temperatures for the High Load of Experimental Setup 2 with 95% Confidence Intervals**

The range of the uncertainty intervals in this example indicate that the data was reasonably well repeated. The exception is the takedown pipe outlet wall temperature (2w), which seemed to experience some fluctuation in the original data.

In the results of the experimental analysis given in Section 6 similar error bars representing the average 95% confidence interval of each temperature are plotted on the applicable curves.

# Appendix B: Determination of Input Conditions for the Numerical Simulation

The initial values and input conditions required for the numerical simulation are determined from the experimental data. The method by which this is done is described by means of a sample calculation in Section B1. The resulting input and initial values corresponding to each experimental configuration are summarised in table form in Section B2.

## B1 Method of Input Determination

The numerical simulation requires the ambient temperature as the initial temperature condition for the exhaust system. The input mass flow rates of gas and vapour and the input temperature must also be determined. The methods of determining each of these values are now individually discussed. The experimental data used in the sample calculations that follow are obtained from the high load case of ES2 using the standard cast iron manifold. This is the same set of data that was used in the error analysis of Appendix A.

### B1.1 Ambient Temperature

The ambient temperature, $T_{amb}$, was taken as the arithmetic mean value of all the ambient temperatures for the four test runs of the given test configuration. This produced a single constant value for the test configuration.

$$T_{amb} = \frac{\bar{T}_{amb,Run1} + \bar{T}_{amb,Run2} + \bar{T}_{amb,Run3} + \bar{T}_{amb,Run4}}{4} = 22.7\,°\text{C} \qquad \text{B.1}$$

where $\bar{T}_{amb,Run1,2,3\ and\ 4}$ are the average ambient temperatures for test runs 1 to 4. The values for this calculation are not shown as there are too many data points (540 logged values per run) for them to be practically illustrated.

### B1.2 Gas Specific Heat and Specific Gas Constant

The specific gas constant, $R_g$, and specific heat, $C_{P,g}$, of the *gas* are dependent on the composition of the gas. The gas composition was determined by means of a combustion analysis. Before the analysis is performed the measured fuel flow rate and air/fuel ratio factor λ are determined. Although these values vary with time, for the purposes of the gas property calculation the average values are obtained by taking the mean of the data for all test runs of a given test configuration (as was done for the ambient temperature).

For the test configuration under discussion the averaged value for the fuel flow rate is $\dot{m}_{fuel} = 0.000602$ kg/s and $\lambda = 0.973$. From these values the mass flow rate of air is calculated:

$$\begin{aligned} \dot{m}_{air} &= \lambda A_s \dot{m}_{fuel} \qquad \text{B.2} \\ &= (0.973)(15.27)(0.000602) \\ &= 0.00895 \text{ kg/s} \end{aligned}$$

where $A_s$ = 15.27 is the mass based stoichiometric air/fuel ratio for gasoline ($C_7H_{17}O_0N_0$).

The total mass flow rate of the combustion gasses is now:

$$\dot{m}_T = \dot{m}_{fuel} + \dot{m}_{air} \qquad \text{B.3}$$
$$= 0.000602 + 0.00895$$
$$= 0.00955 \text{ kg/s}$$

The combustion analysis can now be performed using the equilibrium combustion reaction equation:

$$C_\alpha H_\beta O_\gamma N_\delta + a_s(O_2 + 3.76N_2) \rightarrow n_1CO_2 + n_2H_2O + n_3N_2 + n_4O_2 + n_5CO + n_6H_2 \qquad \text{B.4}$$

For this fuel $\alpha$ = 7, $\beta$ = 17, $\delta$ = 0 and $\gamma$ = 0. The constants $n_{1\text{-}6}$ represent the number of moles of each combustion product for every mole of fuel burnt. The calculation of these molar constants depends on whether the combustion is *lean* ($\lambda$ > 1) or *rich* ($\lambda$ < 1). Table B.1 shows the formulae for these molar constants in both cases.

**Table B.1 Calculation of Combustion Product Constants**

| **Species** | n | $\lambda > 1$ | $\lambda < 1$ |
|---|---|---|---|
| ***$CO_2$*** | $n_1$ | $\alpha$ | $\alpha - n_5$ |
| ***$H_2O$*** | $n_2$ | $\beta/2$ | $\beta/2 - d + n_5$ |
| ***$N_2$*** | $n_3$ | $\delta/2 + 3.76a_s$ | $\delta/2 + 3.76a_s$ |
| ***$O_2$*** | $n_4$ | $a_s(\lambda - 1)$ | 0 |
| ***CO*** | $n_5$ | 0 | $n_5$ |
| ***$H_2$*** | $n_6$ | 0 | $d - n_5$ |

In Table B.1 $a = 1 - K$, $b = \beta/2 + K\alpha - d(1-K)$, $c = -\alpha dK$, $d = 2a_s(1-\lambda)$ and $n_5 = \dfrac{-b + \sqrt{b^2 - 4ac}}{2a}$. The molar stoichiometric air/fuel ratio for this fuel is $a_s = \alpha + \dfrac{\beta}{4} - \dfrac{\gamma}{2} = 11.25$. The constant *K*, defined as $K(T) = \dfrac{n_2 n_5}{n_1 n_6}$, is the temperature dependent equilibrium constant for the reaction:

$$CO_2 + H_2 \leftrightarrow CO + H_2O \qquad \text{B.5}$$

The value of *K* is obtained from a curve fit for a temperature range of 400 < *T* < 3200 K, as published in JANAF table data (Stull *et al*., 1971):

$$\ln K(T) = 2.743 - \frac{1.761}{t} - \frac{1.611}{t^2} + \frac{0.2803}{t^3} \qquad \text{B.6}$$

where $t = \dfrac{T}{1000}$.

For the example under study the equilibrium constant $K$ is evaluated at a representative exhaust gas temperature of $T = 1000t = 880$ K as follows:

$$\ln K(T) = 2.743 - \frac{1.761}{t} - \frac{1.611}{t^2} + \frac{0.2803}{t^3}$$

$$= 2.743 - \frac{1.761}{0.88} - \frac{1.611}{0.88^2} + \frac{0.2803}{0.88^3} = -0.92714$$

which gives $K = 0.395683$.

For this example $\lambda = 0.973 < 1$, so the rich case combustion analysis is performed in order to calculate the molar constants $n_{1\text{-}6}$. The unknown variables in Table B.1 are evaluated as:

$$a = 1 - K = 1 - 0.39568 = 0.6043$$

$$d = 2a_s(1-\lambda) = 2(11.25)(1-0.973) = 0.5984$$

$$b = \beta/2 + K\alpha - d(1-K) = 17/2 + 0.395683(7) - 0.5984(1-0.39568) = 10.908$$

$$c = -\alpha dK = -7(0.5984)(0.39568) = -1.6574$$

$$n_5 = -b + \sqrt{b^2 - 4ac}\,/2a$$

$$= -10.908 + \sqrt{10.908^2 - 4(0.6043)(-1.6574)}\,/2(0.6043) = 0.15069$$

and the resulting molar constants, and the fraction of the total number of moles each constant represents, are given in Table B.2.

**Table B.2 Molar Combustion Product Composition for Sample Calculation**

| **Species** | $i$ | $\lambda < 1$ | $n_i$ (mol) | $y_i = n_i / n_{Total}$ |
|---|---|---|---|---|
| $CO_2$ | 1 | $\alpha - n_5$ | 6.849313 | 0.120852 |
| $H_2O$ | 2 | $\beta/2 - d + n_5$ | 8.052286 | 0.142078 |
| $N_2$ | 3 | $\delta/2 + 3.76a_s$ | 41.175 | 0.726511 |
| $O_2$ | 4 | 0 | 0 | 0 |
| $CO$ | 5 | $n_5$ | 0.150687 | 0.002659 |
| $H_2$ | 6 | $d - n_5$ | 0.447714 | 0.120852 |
| Total mol: $n_{Total}$ =56.675 | | | | |

The molar composition and the individual molar mass of each combustion product are now used to calculate the mass fraction of each gas species. The results are shown in Table B.3.

**Table B.3 Mass Fraction of Combustion Products for Sample Calculation**

| Species | $M_i$ (g/mol) | $m_i = n_i M_i/1000$ (kg) | $X_i^m = m_i / m_{Total,mix}$ |
|---|---|---|---|
| $CO_2$ | 44.01 | 0.301438 | 0.18781 |
| $H_2O$ | 18.015 | 0.145022 | 0.090355 |
| $N_2$ | 28.013 | 1.153435 | 0.718643 |
| CO | 28.011 | 0.004221 | 0.00263 |
| $H_2$ | 2.016 | 0.000903 | 0.000562 |
| Total | | $m_{Total,mix}$ = 1.605019 | 1 |

The simulation treats the total exhaust gas as a mixture of the vapour and the combined 'dry' gas components. The vapour is therefore removed from the gas mixture and the properties of the remaining gas are calculated. For this to be done the mass fractions of the constituent 'dry' gas components are calculated for the portion of the gas mixture from which the vapour has been excluded, as shown in Table B.4.

**Table B.4 Mass Fractions, Cp and R Values of the Gas Components Excluding Water Vapour**

| Species | $M_i$ (g/mol) | $m_i = n_i M_i/1000$ (kg) | $X_i^{m,g} = \frac{m_i}{m_{Total,g}}$ | $C_{P.i}$ (J/kgK) | $R_i$ (J/kgK) |
|---|---|---|---|---|---|
| $CO_2$ | 44.01 | 0.301438 | 0.206465 | 1102 | 188.9 |
| $N_2$ | 28.013 | 1.153435 | 0.790026 | 1086 | 296.8 |
| CO | 28.011 | 0.004221 | 0.002891 | 1100 | 296.8 |
| $H_2$ | 2.016 | 0.000903 | 0.000618 | 14571 | 4124 |
| Total | | $m_{Total,g}$ = 1.459997 | 1 | | |

The gas properties are now calculated using the individual component properties and mass fractions:

$$R_g = \sum R_i X_i^{m,g} \qquad \text{B.7}$$
$$= 188.9(0.20645) + 296.8(0.790026) + 296.8(0.002891) + 4124(0.000618)$$
$$= 276.9 \text{ J/kg}$$

$$C_{Pg} = \sum C_{Pi} X_i^{m,g} \qquad \text{B.8}$$
$$= 1102(0.20645) + 1086(0.790026) + 1100(0.002891) + 14571(0.000618)$$
$$= 1097.7 \text{ J/kg}$$

The value of $C_{Pg}$ is taken as constant for each test configuration. This is judged to be reasonable since the variation in the $C_P$ of the dominant gas component, nitrogen, is in the order of 1% over the temperature range occurring in the experiments. The properties of the *gas mixture* will, however, vary according to the amount of vapour present, as described in Section 3.

### B1.3 Exhaust Port Gas Mass Flow Rate

The input mass flow rate of the gas $\dot{m}_{g,Input\,2,High}(t)$ is calculated from the ratio of the gas mass to the gas mixture mass and the total incoming mass flow rate. In this calculation the incoming total mass flow rate is calculated for the full test period from the measured values of $\dot{m}_{fuel}$ kg/s and $\lambda$ using Equation 2.3 at each logged point. The incoming gas mass flow rate is then calculated using the total incoming gas flow rate and the average mass ratio between the gas and the gas mixture, again at each logged point:

$$\dot{m}_g = \frac{m_{Total,g}}{m_{Total,mix}} \dot{m}_T \qquad \text{B.9}$$

Equation B.10 was evaluated for the test period using Microsoft Excel. The values of $\dot{m}_g$ are plotted against time in Figure B.1. The time dependent input gas mass flow rate function $\dot{m}_{g,Input\,2,High}(t)$ is defined by the curve fit also shown on Figure B.1. This fit was generated by minimising the square of the error using the Microsoft Excel Solver function.

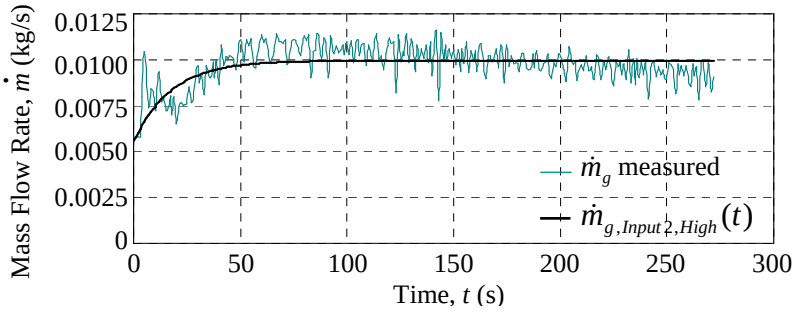


**Figure B.1 Time Dependent Input Gas Mass Flow Rate for Experimental Setup 2, High Load**

The time dependent curve fit function for this load case is given by:

$$\dot{m}_{g,Input2,High}(t) = 0.0044\left(1 - e^{-0.0564t}\right) + 0.0055 \text{ kg/s} \qquad \text{B.10}$$

with $t$ in s. The gas mass flow rate input functions were generated in a similar way for the other load cases. As there was not a significant difference between the input flow mass rates for the same load case using different manifolds in ES2, only one input function per load was used for ES2. The functions for the three load cases of both ES1 and ES2 are given in Section B.2.

### B1.4 Exhaust Port Vapour Mass Flow Rate

The input mass flow rate of the vapour $\dot{m}_{v,Input\,2,High}$ is the sum of the combustion product vapour and any vapour that was drawn in with the intake air. To calculate the intake vapour amount the ambient humidity is needed. An average of the measured relative humidity values was taken in the same way as for the ambient temperature, giving:

$$\phi_{amb} = 0.405548$$

At $T_{amb} = 22.7\,°C$, the saturated vapour pressure $P_{sat@T_{amb}}$ = 2.505 kPa (Çengel and Boles, 2002). The absolute humidity is now:

$$\omega = 0.622\frac{\phi P_{sat@T_{amb}}}{P_{amb} - \phi P_{sat@T_{amb}}} \qquad \text{B.11}$$

$$= 0.622\frac{0.04055(2.505)}{101.15 - 0.04055(2.505)} = 0.006384 \text{ kg water/kg dry air}$$

So at each logged point during the test the intake vapour is calculated using:

$$\dot{m}_{v,intake} = \omega \dot{m}_{air} \qquad \text{B.12}$$

$$= 0.006384\dot{m}_{air}$$

The mass of the combustion product vapour is calculated as the mass of the gas mixture less the mass of the gas. The total vapour flow rate at each logged point in the test is thus:

$$\dot{m}_v = \left(\dot{m}_T - \dot{m}_g\right) + \dot{m}_{v,intake} \qquad \text{B.13}$$

The values generated at each logged point and are shown in Figure B.2. A curve fit was performed in the same way as for the input gas input mass rate and is also shown in Figure B.2.

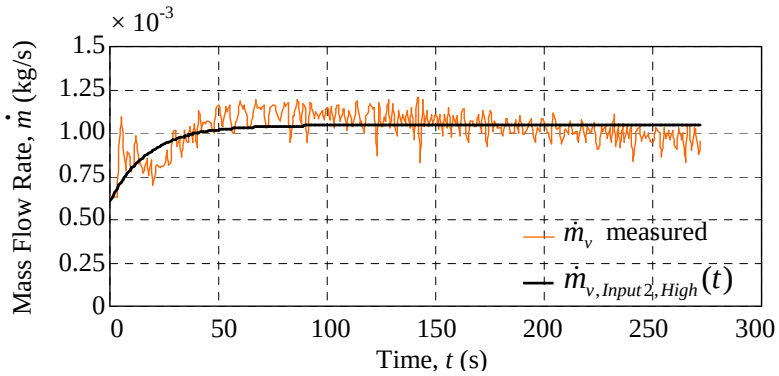


**Figure B.2 Time Dependent Input Vapour Mass Flow Rate for Experimental Setup 2, High Load**

The time dependent curve fit function is given by:

$$\dot{m}_{v,Input\,2,High}(t) = 0.000437\left(1 - e^{-0.0564t}\right) + 0.000608 \text{ kg/s} \qquad \text{B.14}$$

with $t$ in s. As for the gas mass flow rates, the vapour mass flow rate input functions for all the load cases of ES1 and ES2 are given in Section B.3.

### B1.5 Exhaust Port Temperature Function

As discussed in Section 4 two options for the input temperature functions were considered during the course of this research. These are the function generated by a curve fit of the measured data, and a function generated using the true gas temperature prediction method discussed in Section 4.

The curve fit of the measured data was obtained by using Excel Solver to minimise the square of the error between the data and the curve fit in the same way as for the mass flow rate functions. The true gas temperature prediction was performed by using this curve fit as the input value to the true gas prediction algorithm based on the theory laid out in Section 4. In this way a data set of predicted true gas temperatures was generated for the test period. This data was then also converted to a time dependent function by means of a curve fit. The measured and predicted temperature data sets for the test configuration under discussion are plotted in Figure B.3, with the relevant curve fits also shown.

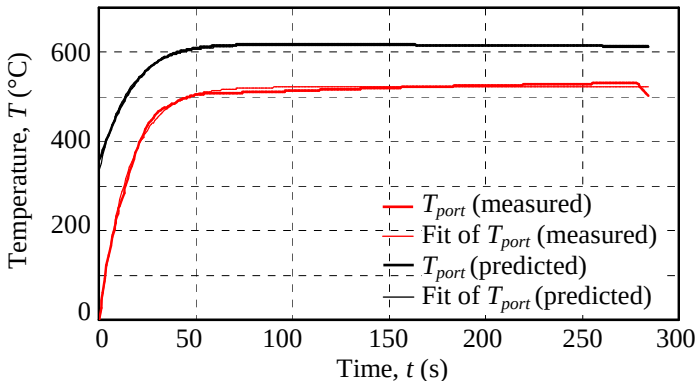


**Figure B.3 Predicted Exhaust Port Temperatures with Input Temperature Function for Experimental Setup 2, Cast Iron Manifold, High Load**

After investigation of the consequences of using each of the input temperature functions it was decided that the curve fit of the measured data would be used (as was discussed in Section 7.3). The exhaust port temperature input function is therefore given by the function of the curve fit of the measured data:

$$T_{Input2,High}(t) = 524.0\left(1 - e^{-0.0750t}\right) + 296\,\mathrm{K} \qquad \text{B.15}$$

with $t$ in s. A list of the input temperature functions for all the load cases of ES1 and ES2 is provided in Section B.2. As is the case with the mass flow rates, the input temperatures at each load in ES2 did not vary significantly with a change in manifold, so only one input temperature per load was generated for ES2.

## B2 Summary of Input Conditions for Numerical Simulation

The procedure described in Section B.1 was performed for all the test configurations of ES1 and ES2. The constant input values for all test configurations are summarised in Table B.5 and the time dependent input functions are given in Tables B.6 and B.7.

**Table B.5 Constant Input Values for All Test Configurations**

| Setup | Input | Low | Medium | High |
|---|---|---|---|---|
| ES1 | $T_{amb}$ (K) | 296.2 | 284.7 | 297 |
| | $R_g$ (J/kgK) | 274.7 | 274.8 | 275.1 |
| | $C_{Pg}$ (J/kgK) | 1089.0 | 1088.9 | 1088.5 |
| ES2 Cast Iron Manifold | $T_{amb}$ (K) | 293.6 | 295.5 | 295 |
| | $R_g$ (J/kgK) | 281.7 | 274.4 | 276.9 |
| | $C_{Pg}$ (J/kgK) | 1114.5 | 1088.5 | 1097.7 |
| ES2 Stainless Steel Manifold | $T_{amb}$ (K) | 297.1 | 299.1 | 298 |
| | $R_g$ (J/kgK) | 282.2 | 274.2 | 275.8 |
| | $C_{Pg}$ (J/kgK) | 1117.9 | 1087.4 | 1094.2 |
| ES2 Thin Walled Stainless Steel Manifold | $T_{amb}$ (K) | 292.3 | 294.8 | 295 |
| | $R_g$ (J/kgK) | 281.9 | 274.1 | 275.7 |
| | $C_{Pg}$ (J/kgK) | 1116.6 | 1086.7 | 1093.7 |

**Table B.6 Time Dependent Mass Flow Rate and Temperature Input Functions for Experimental Setup 1**

| | | |
|---|---|---|
| **Input Temperature Functions (K)** | Low Load | $T_{Input1,Low}(t) = 4610.3\left(1-e^{-0.0718t}\right)+320$ |
| | Medium Load | $T_{Input1,Med}(t) = 448.0\left(1-e^{-0.1250t}\right)+340$ |
| | High Load | $T_{Input1,High}(t) = 476.4\left(1-e^{-0.1102t}\right)+334$ |
| **Input Gas Mass Flow Rate Functions (kg/s)** | Low Load | $\dot{m}_{g,Input1,Low}(t) = -0.0056\left(1-\mathrm{e}^{-0.1210t}\right)+0.0132$ |
| | Medium Load | $\dot{m}_{g,Input1,Med}(t) = -0.0167\left(1-\mathrm{e}^{-0.2198t}\right)+0.0245$ |
| | High Load | $\dot{m}_{g,Input1,High}(t) = -0.0254\left(1-\mathrm{e}^{-0.3312t}\right)+0.0275$ |
| **Input Vapour Mass Flow Rate Functions (kg/s)** | Low Load | $\dot{m}_{v,Input1,Low}(t) = -0.00068\left(1-\mathrm{e}^{-0.1348t}\right)+0.00153$ |
| | Medium Load | $\dot{m}_{v,Input1,Med}(t) = -0.00138\left(1-\mathrm{e}^{-0.2058t}\right)+0.00234$ |
| | High Load | $\dot{m}_{v,Input1,High}(t) = -0.00152\left(1-\mathrm{e}^{-0.3358t}\right)+0.00288$ |

**Table B.7 Time Dependent Mass Flow Rate and Temperature Input Functions for Experimental Setup 2**

| | | |
|---|---|---|
| **Input Temperature Functions (K)** | Low Load | $T_{Input2,Low}(t) = 446.0\left(1-\mathrm{e}^{-0.0750t}\right)+292$ |
| | Medium Load | $T_{Input2,Med}(t) = 521.3\left(1-\mathrm{e}^{-0.0665t}\right)+287$ |
| | High Load | $T_{Input2,High}(t) = 524.0\left(1-\mathrm{e}^{-0.0750t}\right)+296$ |
| **Input Gas Mass Flow Rate Functions (kg/s)** | Low Load | $\dot{m}_{g,Input2,Low}(t) = -0.0028\left(1-\mathrm{e}^{-0.0059t}\right)+0.0054$ |
| | Medium Load | $\dot{m}_{g,Input2,Med}(t) = -0.0167\left(1-\mathrm{e}^{-0.02198t}\right)+0.0245$ |
| | High Load | $\dot{m}_{g,Input2,High}(t) = 0.0044\left(1-\mathrm{e}^{-0.0564t}\right)+0.0055$ |
| **Input Vapour Mass Flow Rate Functions (kg/s)** | Low Load | $\dot{m}_{v,Input2,Low}(t) = -0.00025\left(1-\mathrm{e}^{-0.0061t}\right)+0.000533$ |
| | Medium Load | $\dot{m}_{v,Input2,Med}(t) = -0.001381\left(1-\mathrm{e}^{-0.02058t}\right)+0.002342$ |
| | High Load | $\dot{m}_{v,Input2,High}(t) = 0.000437\left(1-\mathrm{e}^{-0.0564t}\right)+0.000608$ |

# APPENDIX C: Numerical Simulation Solution Method and Sample Calculation

In order to illustrate the solution method used in the numerical simulation, a brief description of the overall solution algorithm structure is given (this structure is represented diagrammatically in Figure 3.9). A sample calculation of the calculation procedure in a single control volume over one time step is also provided. For convenience a nomenclature particular to this discussion and sample calculation is given in Section C.1.

## C1 Sample Calculation Nomenclature

| **Roman Letters:** | | **Subscripts:** | |
|---|---|---|---|
| A | Area, $m^2$ | AB | Gas species A in species B |
| C | Specifc Heat, J/kgK, or coefficient of friction | amb | Ambient |
| cv | Control volume size, m | CatFlow | Catalytic converter gas mixture flow |
| D | Diameter, m or diffusivity, m/s | CatSurface | Catalytic converter surface area |
| G | Volumetric flow rate, $m^3/s$ | c | Channel |
| H | Total enthalpy, J | cat | Catalytic converter |
| h | Heat transfer coefficient, $W/m^2K$ or mass transfer coefficient, m/s or specific enthalpy, J/kg | cond | Conduction |
| i | Control volume number | conv | Convection |
| j | Time step number | cs | Cross section |
| K | Runge Kutta constant, K or volumetric flow rate adjustment factor | cv | Control volume |
| k | Thermal conductivity, W/mK | cvc | Catalytic converter control volume |
| L | Length, m | evap | Evaporation |
| m | Mass, kg | g | Gas |
| $\dot{m}$ | Mass flow rate, kg/s | gL | Gas-liquid interface |
| n | Final control volume | gw | Gas-wall interface |
| P | Pressure, Pa or perimeter, m | H | Hydraulic |
| Q | Heat transfer rate, W | Input1High | Indicating the high load input values from Experimental Setup 1 |
| R | Specific gas constant, J/kgK | i | Control volume number or inside or interface |
| T | Temperature, K | ideal | Predicted by the ideal gas equation |
| $\Delta\dot{T}$ | Temperature gradient, K/s | in | Into the control volume |
| t | Time, s | j | Time step number |
| U | Internal energy, J | L | Liquid |
| v | Velocity, m/s | Lw | Liquid-wall interface |
| $\dot{v}$ | Velocity gradient, $m/s^2$ | min | Minimum |
| X | Channel width, m | mix | Gas mixture |
| z | Thickness, m | old | Calculated in a previous time step |
| **Greek Letters:** | | out | Out of the control volume |
| α | Absorbtivity | T | Total |
| ε | Emissivity | V | Volume |
| μ | Viscosity, $Ns/m^2$ | v | Vapour |
| ν | Specific volume, $m^3/kg$ | w | Wall |
| ρ | Density, $kg/m^3$ | wcs | Channel wall cross sectional area |
| σ | Stefan-Boltzmann Constant | | |

| Dimensionless Numbers | |
|---|---|
| Pr | Prandtl number |
| Re | Reynolds number |
| Sc | Schmidt number |
| Sh | Sherwood number |

## C2 Summary of Solution Method

The numerical model consists of four consecutive control volume '*for*' loops, representing the four pipe sections, inside a time '*for*' loop. Control volume numbers are represented by i, time step numbers by j and the time step length is Δt.

### C.1.1 Definition of Initial Conditions

Before the solution is begun the geometry of each pipe section and all relevant constants are defined. Initial values for the temperature, total pressure, gas, liquid and vapour masses and related properties for each pipe section are allocated according to ambient conditions.

The input conditions into the model are the temperature and mass flow rates of gas and vapour into the first pipe control volume, which represent the flow through the exhaust valve. These values are determined from the experimental investigation discussed in Section 5 and Appendix B. The input values are defined as the values in the first control volume of the model, cv(1). The first pipe control volume is therefore defined as cv(2) (as shown in Figure 3.4).

### C.1.2 Stepwise Solution Procedure

With the input and initial conditions defined, the (outer) '*for'* loop for the time vector t(j) and the inner '*for*' loops for the position vectors, cv(i) of each pipe section are constructed.

**Start time loop**: *for* j = 2: length(t)
At the start of each time step the input functions are used to calculate the *driving* volumetric flow rate for the time step j of the gas mixture using the ideal gas equation. This value is constant throughout the system for the time step, but the local volumetric flow rates in each control volume will be calculated by adjusting this value by the $K_v$ method described in Section 3.3. The differential change in gas mixture velocity over the time step is calculated using the change in volumetric flow rate (defined by the change in the input functions over the time step) and the pipe section cross sectional area.

As the volumetric flow rates calculated are the total flow rates through the manifold, they are divided by four to account for the averaged flow rate through a single manifold pipe. The same is done for the differential change in velocity, which is then taken as constant over the pipe section. With the inputs to the first pipe section (the manifold), the consecutive control volume calculations can now be performed.

**Start cv loop 1 (Manifold):** for i = 2:$n_1$
For the fourth order Runge Kutta solution the differential equations must be evaluated once at the beginning of the time step, (defined as the end of the previous time step) t = (j-1)Δt, twice at the middle of the time step t = (j-0.5)Δt and once at the end of the time step t = (j)Δt in order to evaluate the factors $K_{1\text{-}4}$. For $K_1$, at the beginning of the time step, the relevant values at the end of the previous time step (or the initial values when j = 1) are used.

The time dependent mass, mass flow rates and all related properties of the liquid, vapour and gas are calculated for each Runge Kutta constant, from which the gas mixture, liquid layer and wall temperatures in the control volume are calculated. This procedure is described by the sample calculation given in Section C.2.

The calculations are performed progressively down the pipe until the final control volume for this pipe section cv($n_1$) is reached.
**End cv loop 1**

The final values of Pipe Section 1 are used as the input values to Pipe Section 2 but the mass flow rates of gas, vapour and liquid are doubled to account for the flow in two manifold pipes combining into one of the two pipes in the first section of the takedown pipe. The *driving* gas mixture volumetric flow rate for this section is taken as half the total volumetric flow rate.

**Start cv loop 2 (Takedown Pipe, part 1):** *for* i = $n_1$+1:$n_2$
The calculations in this cv loop are performed in the same manner as in cv loop 1, but the input values mentioned above as well as the pipe geometry and material properties differ.
**End cv loop 2**

As before the final values from the final control volume cv($n_2$) are used as the input values to cv loop 3. Again the gas, vapour and liquid mass flow rates are doubled as the two pipe pipes of the first part of the takedown section join to form a single pipe. The total *driving* gas mixture volumetric flow rate is used in this section.

**Start cv loop 3 (Takedown Pipe, part 2):** *for* i = $n_2$+1:$n_3$
The calculations in this cv loop are performed in the same manner as in cv loop 2. Only the input values mentioned above differ.
**End cv loop 3**

As the total flow moves from the outlet of the takedown pipe into the catalytic converter there is no adjustment made to the mass or volumetric flow rates at this point. The change in flow area from the pipe to the catalytic converter does however result in a velocity decrease which is accounted for by means of the ratio of new to old area.

**Start cv loop 4 (Catalytic Converter):** *for* i = $n_2$+1:$n_3$
The same general calculation procedure as before is followed for the catalytic converter section, with a few differences. The total flow area and mass flow rates of the gas, vapour and liquid are used in the calculations except in the Reynolds and Nusselt number calculations where a single channel is modelled. Also, the external convection and radiation terms in the wall temperature differential equation (Equation 3.9) are neglected in this section as the catalytic converter channels have been assumed to be adiabatic at the centreline of the channel walls (as was discussed in Section 3.2).
**End cv loop 4**

In order to decrease the simulation time the values of all relevant properties for each control volume are saved in vector form for the previous time step only. These ‘old’ vectors are used as

the initial values for the next time step. The desired output results of the simulation, namely the gas mixture, liquid and wall temperatures, the liquid and vapour masses and other values of interest such as local pressure and flow rates are periodically saved to a Microsoft Excel spreadsheet. The desired control volume vectors are stored at intervals corresponding to 0.5 s of elapsed time, which corresponds to the sampling rate of the experimental investigation.
**End time loop**

The procedure described above is applicable to the simulation corresponding to ES1. For ES2, where the manifold joins into a single takedown pipe, only two control volume loops are used. The total mass flow rate is again divided by four at the manifold inlet, and the total mass flow is used in the takedown section.

## C3 Numerical Simulation Sample Calculation

The following this sample calculation is provided in order to illustrate the solution procedure in each control volume. The calculation is performed using initial values that were generated by stopping the simulation at a point corresponding to a time of $t$ = 13 s, in the control volume at the catalytic converter mid-bed cv($n_3$ + ($n_4$-$n_3$)/2), which corresponds to measurement position 3 (shown in Figure 6.1) in the high load case of ES1. This point in time and position was chosen because it allows the moisture behaviour to be illustrated (that is, there is a liquid layer present and mass transfer processes are still occurring).

### C3.1 Constants, Initial Values and Variable Property Functions

Before the calculation is performed the point in time and position in the exhaust system are defined. The geometry of the control volume and the physical properties of the gas, vapour and wall are also defined.

#### C3.1.1 Time and Position

| | | | |
|---|---|---|---|
| $i := 85$ | Control volume number | $j := 26000$ | Time step number |
| $cv := 0.01\,m$ | Control volume length | $\Delta t := 0.0005\,s$ | Time step size |

From the above the time and position are calculated as:

| | |
|---|---|
| $t := j \cdot \Delta t = 13\,s$ | Total time elapsed |
| $L_{cv} := cv \cdot i = 0.85\,m$ | Distance from exhaust port to control volume under discussion |

#### C3.1.2 Catalytic Converter Geometry and Material Properties

The catalytic converter geometry and material properties used are listed below:

| | | | |
|---|---|---|---|
| $D_{cat} := 0.15\,m$ | Catalytic converter outer diameter | $k_{cat} := 1.5\frac{W}{m \cdot K}$ | Wall thermal conductivity |
| $L_{cat} := 0.2\,m$ | Catalytic converter Length | $\rho_{cat} := 1550\frac{kg}{m^3}$ | Wall density |
| $z_c := 0.0001\,m$ | Channel wall half thickness | $C_{Pcat} := 1020\frac{J}{kg \cdot K}$ | Wall heat capacity |
| $X := 0.001\,m$ | Channel width | | |

From which the following are calculated:

$A_{cat} := \pi \cdot \frac{D_{cat}^2}{4} = 0.02\ m^2$ Total cross sectional area of catalytic converter

$A_c := X^2 = 1 \times 10^{-6}\ m^2$ Cross sectional channel flow area

$P_c := 4 \cdot X = 4 \times 10^{-3}\ m$ Inner perimeter of a channel

$D_{Hc} := 4 \cdot \frac{A_c}{P_c} = 1 \times 10^{-3}\ m$ Hydraulic diameter of a channel

$A_{catT} := (X + 2 \cdot z_c)^2 = 1.44 \times 10^{-6}\ m^2$ Total area occupied by a channel

$N_c := \frac{A_{cat}}{A_{catT}} = 12272$ Number of channels in catalytic converter

$A_{CatFlow} := A_c \cdot N_c = 0.01\ m^2$ Total cross sectional flow area in catalytic converter

$V_{cv} := A_{CatFlow} \cdot cv = 0.12\ L$ Volume in the control volume

$A_{wcs} := (A_{catT} - A_c) \cdot N_c = 5.4 \times 10^{-3}\ m^2$ Total cross sectional wall area

$m_w := \rho_{cat} \cdot A_{wcs} \cdot cv = 0.14\ kg$ Wall mass per control volume

### C3.1.3 Physical Properties of the Gas, Vapour and Liquid

The following properties of the gas, vapour and liquid were taken as constant:

| | | | |
|---|---|---|---|
| $R_g := 274.4 \frac{J}{kg \cdot K}$ | Gas constant of the dry gas | $R_v := 461.5 \frac{J}{kg \cdot K}$ | Gas constant of the vapour |
| $C_{Pg} := 1089 \frac{J}{kg \cdot K}$ | Constant pressure heat capacity of the gas | $C_{Pv} := 2000 \frac{J}{kg \cdot K}$ | Constant pressure heat capacity of the vapour |
| $C_{vg} := R_g - C_{Pg}$ | Constant volume heat capacity of the gas | $C_{vv} := R_v - C_{Pv}$ | Constant volume heat capacity of the vapour |
| $Pr := 0.6974$ | Prandtl number of the gas | $C_{PL} := 4220 \frac{J}{kg \cdot K}$ | Heat capacity of the liquid |
| $\mu_L := 2.5 \times 10^{-4} N \cdot \frac{s}{m^2}$ | Viscosity of the liquid | $\rho_L := 990 \frac{kg}{m^3}$ | Density of the liquid |
| $\alpha_g := 0.046$ | Absorbtivity of the gas | $\varepsilon_g := 0.061$ | Emissivity of the gas |

The properties that were calculated as functions of temperature are illustrated in Figures C.1 to C.4. The data were taken from the steam tables in Incropera and DeWitt (2002) and the curve fit functions were generated in Microsoft Excel.

Thermal conductivity of gas and vapour:

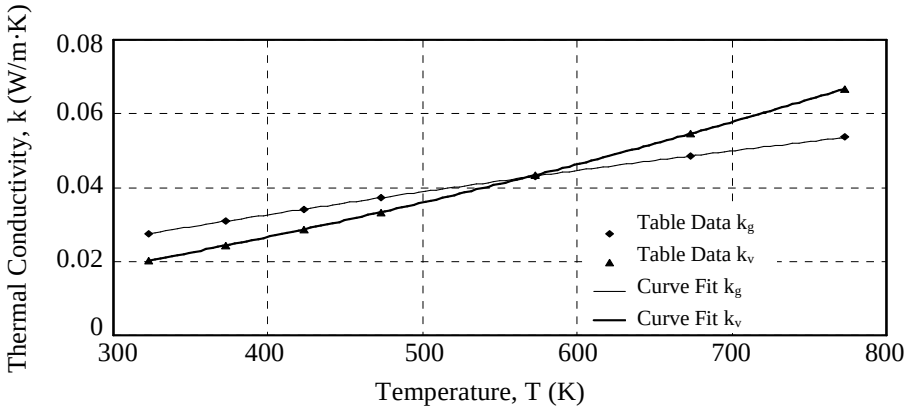


**Figure C.1 Thermal Conductivity of the Gas and Vapour as a Function of Temperature**

The curve fit functions for the thermal conductivity of the gas and vapour are as follows (T in K):

$$k_g(T) := -2.475710^{-8}T^2 + 8.505510^{-5}T + 2.550210^{-3}\frac{W}{m\cdot K}$$

$$k_v(T) := 5.695810^{-8}T^2 + 4.094710^{-5}T + 1.185210^{-3}\frac{W}{m\cdot K}$$

Viscosity of the gas and vapour:

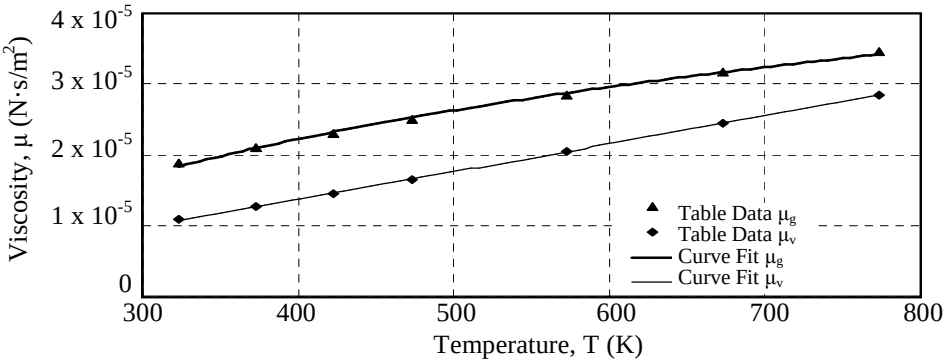


**Figure C.2 Viscosity of the Gas and Vapour as a Function of Temperature**

The curve fit functions for the gas and vapour viscosity are (T in K):

$$\mu_g(T) := 1.81410^{-5}\ln(T) - 8.647410^{-5}N\cdot\frac{s}{m^2}$$

$$\mu_v(T) := 3.37410^{-12}T^2 + 3.570510^{-8}T - 1.127710^{-6}N\cdot\frac{s}{m^2}$$

Enthalpy of saturated water vapour:

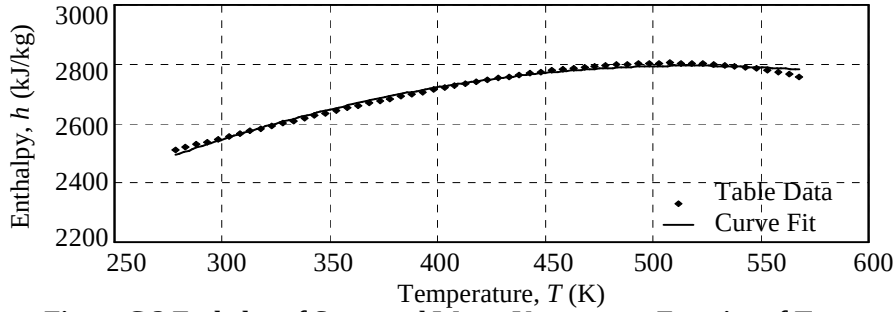


**Figure C.3 Enthalpy of Saturated Water Vapour as a Function of Temperature**

The curve fit function of the vapour enthalpy is:

$$h_{sat}(T) := -5.244746 \cdot T^2 + 5430.757 \cdot T + 1388989 \cdot \frac{J}{kg}$$

for the temperature range 283K < T < 70K. Upper and lower enthalpy limits are set as $h_{sat} = 2501.3$ kJ if T < 283K and $h_{sat} = 2099.3$ kJ if T ≥ 570K.

**Saturated Vapour Pressure:**

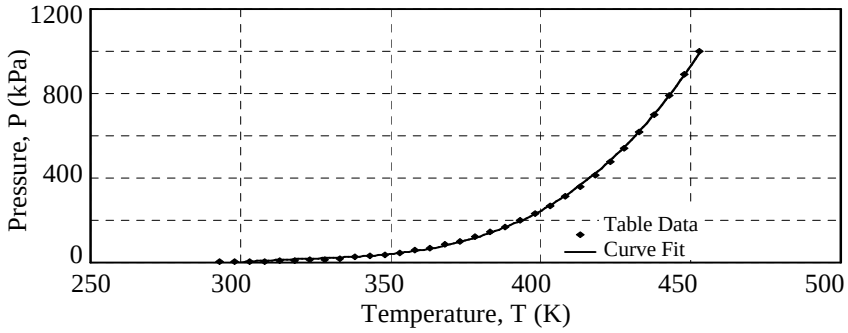


**Figure C.4 Saturated Pressure of Water Vapour as a Function of Temperature**

The curve fit of the saturated vapour pressure was piecewise defined as follows:

$$P_{sat}(T) := 2.386 \times 10^{-40} \cdot T^{17.419} Pa \qquad \text{if } T < 340K$$

$$P_{sat}(T) := 0.072898 e^{0.0351 \cdot T_{old} + 10128} Pa \qquad \text{if } T \geq 340K$$

An upper limit of 500kPa was set to prevent divergence in the simulation.

### C3.1.4 Miscellaneous Other Constants

Other constants used in the simulation include:

$\sigma := 5.67 \times .10^{-8} \frac{W}{m^2 K^4}$ Stephan-Boltzmann Constant

$h_{Lw} := 1000 \frac{W}{m^2 \cdot K}$ Convective heat transfer coefficient between the liquid layer and the wall

### C3.1.5 Initial Values Calculated in the Previous Time Step or Control Volume

The stored values calculated in the previous times step for the control volume in question, as well as some values calculated in the current time-step for the previous control volume are used as inputs. The relevant values for the control volume at the end of the previous time step are:

| | | | | | |
|---|---|---|---|---|---|
| $T_{mix\_old} := 299.09249\,K$ | Gas mixture temperature | | $\dot{m}_{g\_old} := 0.01231868\,\frac{kg}{s}$ | Gas mass flow rate | |
| $T_{L\_old} := 297.65776\,K$ | Liquid layer temperature | | $\dot{m}_{v\_old} := 0.33506719\times 10^{-3}\,\frac{kg}{s}$ | Vapour mass flow rate | |
| $T_{w\_old} := 297.54375\,K$ | Wall temperature | | $\dot{m}_{L\_old} := 0\,\frac{kg}{s}$ | Liquid mass flow rate | |
| $m_{g\_old} := 0.0981168\times 10^{-3}\,kg$ | Gas mass | | $v_{L\_old} := 0\,\frac{m}{s}$ | Liquid velocity | |
| $m_{v\_old} := 0.002672195\times 10^{-3}\,kg$ | Vapour mass | | $P_{old} := 100085.9\,Pa$ | Pressure | |
| $m_{mix\_old} := 0.1007884\times 10^{-3}\,kg$ | Gas mixture mass | | $K_{v\_old} := 0.6856$ | Volumetric flow rate adjustment factor | |
| $m_{L\_old} := 0.154535\times 10^{-3}\,kg$ | Liquid mass | | | | |

Values calculated in the previous control volume during this time step are also required:

$T_{mix\_old.in} := 304.7604\ K$ Temperature of gas mixture into control volume

$\dot{m}_{g.in} := 0.012390026\,\frac{kg}{s}$ Gas mass flow rate into the control volume

$\dot{m}_{g2.in} := 0.012388786\,\frac{kg}{s}$ Gas mass flow rate into the control volume

$\dot{m}_{v.in} := 0.4070377\times 10^{-3}\,\frac{kg}{s}$ Vapour mass flow rate into the control volume

$\dot{m}_{v2.in} := 0.4070231\times 10^{-3}\,\frac{kg}{s}$ Vapour mass flow rate into the control volume

$\dot{m}_{L.in} := 0\,\frac{kg}{s}$ Liquid mass flow rate into the control volume

$v_{mix.in} = 2.773\,\frac{m}{s}$ Gas mixture velocity into the control volume

The temperature of the wall in the next control volume is also needed (for the calculation of axial conduction heat transfer):

$T_{w\_old.out} := 297.1869\,K$ Wall temperature in the next control volume

## C3.2 Time Dependent Inputs

At the exhaust port the input values into the system are given by:

$T_{Input1High}(t) := 400.37\cdot\left(1 - e^{-0.0626\cdot t}\right) + 686.65 = 909.588\ K$ Input temperature

$\dot{m}_{gInput1High}(t) := -0.0254\left(1 - e^{-0.3312\cdot t}\right) + 0.0275 = 12.308\times 10^{-3}\,\frac{kg}{s}$ Input gas mass flow rate

$\dot{m}_{vInput1High}(t) := -0.00152\left(1 - e^{-0.3358\cdot t}\right) + 0.00288 = 1.379\times 10^{-3}\,\frac{kg}{s}$ Input vapour mass flow rate

From these input values the total *driving* volumetric flow rate is calculated using the ideal gas equation:

$R_{InputMix} := \frac{\dot{m}_{gInput1High}}{\dot{m}_{InputMix}} \cdot R_g + \frac{\dot{m}_{vInput1High}}{\dot{m}_{InputMix}} \cdot R_v = 341.92 \cdot \frac{J}{kg \cdot K}$ Specific gas constant of the gas mixture

$G := \dot{m}_{InputMix} \cdot R_{InputMix} \cdot \frac{T_{Input1High}}{P_{old1}} = 36.45447 \times 10^{-3} \frac{m^3}{s}$ Driving volumetric flow rate

$v := \frac{G}{A_{CatFlow}} = 2.97058 \frac{m}{s}$ Driving gas velocity at the end of the time step

The driving volumetric flow rate must also be calculated at the start and mid-point of the time step, because the Runge Kutta method requires calculations to be performed at the start, midpoint and end of the time step. The same method as above is used, but with $t = t - \Delta t$ and $t = t - \Delta t/2$ substituted into the input functions. This gives:

$G_{old} = 36.45434 \times 10^{-3} \frac{m^3}{s}$ Driving volumetric flow rate at beginning of the time step

$v_{old} = 2.970567 \frac{m}{s}$ Driving gas velocity at beginning of the time step

$G_2 = 36.4544 \times 10^{-3} \frac{m^3}{s}$ Driving volumetric flow rate at mid-point of the time step

$v_2 = 2.970572 \frac{m}{s}$ Driving gas velocity at mid-point of the time step

From the difference in velocity over the time step is used to calculate the differential change in velocity:

$\dot{v} := \frac{v - v_{old}}{\Delta t} = 19.93 \times 10^{-3} \frac{m}{s^2}$ Differential change in velocity over the time step

## C3.3 Calculations Performed in the Control Volume

The calculations in the control volume can now be begun. The fourth order Runge Kutta method required the temperature gradients to be predicted at the beginning of the time step, twice at the mid-point of the time step, and at the end of the time step (as shown in Equation 3.2). The Runge Kutta constants $K_{1\text{-}4}$ are calculated for the gas mixture, liquid layer and wall temperatures. For clarity in the explanations that follow, the calculations performed at the start of the time step will be referred to as the $K_1$ calculations, those performed at the mid-point of the time step as the $K_2$ and $K_3$ calculations (for the first and second set of calculations respectively) and those at the end of the time step as the $K_4$ calculations.

The sample calculation as a whole is divided into broad steps. Steps 1 to 4 describe the $K_1$ calculation procedure in detail. Step 5 describes the $K_{2\text{-}4}$ calculations briefly, listing only relevant differences from the $K_1$ calculations and the results obtained for each. Steps 6 to 8 describe the method used to calculate the final values, of for example the temperatures and masses, in the control volume.

**Step 1: Calculation of the gas mixture properties and the internal convective heat transfer coefficient**

The $K_1$ calculation procedure begins with the calculation of the gas mixture Reynolds number. To do this the gas mixture density is calculated using the mass of vapour and gas in the control volume at the end of the previous time step. The gas mixture viscosity is calculated from the temperature dependent viscosity function for the gas and vapour, and the relative masses of gas and vapour in the gas mixture.

$\rho_{mix1} := \frac{m_{g\_old} + m_{v\_old}}{V_{cv}} = 821.303 \times 10^{-3} \frac{kg}{m^3}$ Gas mixture density

$$\mu_{mix1} := \frac{m_{g\_old} \cdot \mu_g(T_{mix\_old}) + m_{v\_old} \cdot \mu_v(T_{mix\_old})}{m_{mix\_old}} = 16.75 \times 10^{-6} \frac{kg}{m \cdot s}$$ Gas mixture viscosity

$$Re_{D1} := \rho_1 \cdot v_{old} \cdot \frac{D_{Hc}}{\mu_{mix1}} = 145.656$$ Reynolds number

Using the Reynolds number the internal convective heat transfer coefficient is calculated using an appropriate Nusselt correlation. In this case the flow is laminar, so a constant Nusselt number is used (as defined by Equation 2.7).

$Nu_D := 4.0$ Nusselt number for laminar flow

$$k_{mix1} := \frac{m_{g\_old} \cdot k_g(T_{mix\_old}) + m_{v\_old} \cdot k_v(T_{mix\_old})}{m_{mix\_old}} = 25.583 \times 10^{-3} \frac{W}{m \cdot K}$$ Gas mixture thermal conductivity

$$h_{i1} := Nu_D \cdot \frac{k_g(T_{mix\_old})}{D_{Hc}} = 11.4536 \frac{W}{m^2 \cdot K}$$ Internal convective heat transfer coefficient

**Step 2: Calculation of the moisture mass transfer**

The vapour pressure is determined from the vapour mass and the ideal gas equation, and the saturation pressure from the gas temperature and a curve fit of steam table data shown in Figure C.4.

$$P_{v1} := \frac{R_v \cdot m_{v\_old} \cdot T_{mix\_old}}{V_{cv}} = 3.006 \times 10^3 \text{ Pa}$$ Partial pressure of the vapour

$$P_{vsat} := P_{sat}(T_{mix\_old}) = 3.19 \times 10^3 \text{ Pa}$$ Saturated vapour pressure

The vapour partial pressure is lower than the saturation pressure. The amount of condensation (or evaporation) occurring is therefore calculated using the heterogeneous mass transfer model (Equations 2.22 to 2.25).

$$D_{AB1} := 1.87 \times 10^{-10} \cdot \frac{(T_{mix\_old})^{2.072}}{P_{old} \cdot 10^{-5}} = 25.196 \times 10^{-6} \frac{m^2}{s}$$ Diffusivity of water vapour in air

$$Sc_1 := \frac{\mu_{mix1}}{\rho_{mix1} D_{AB1}} = 809.416 \times 10^{-3}$$ Schmidt number

$$Sh_1 := 0.023 \cdot Re_{D1}^{0.8} \cdot Sc_1^{0.35} = 1.1488$$ Sherwood number

$$h_{conv\_evap1} := Sh_1 \cdot \frac{D_{AB1}}{D_{Hc}} = 28.946 \times 10^{-3} \frac{m}{s}$$ Convective mass transfer coefficient

$$\dot{m}_{evap1} := h_{conv\_evap1} \cdot \frac{A_{CatSurface}}{R_v} \cdot \left( \frac{P_{sat}(T_{L\_old})}{T_{L\_old}} - \frac{P_{v1}}{T_{mix\_old}} \right) = -5.994 \times 10^{-6} \frac{kg}{s}$$ Heterogeneous mass transfer rate

The negative mass transfer rate indicates that condensation is occurring. Before the calculation is continued a check is performed to make sure that if the calculated rate is maintained for the full time step it does not cause more vapour to condense than is present in the control volume. This is done by comparing the mass that will condense over the time step to the mass of vapour present:

$$\dot{m}_{evap1} := m_{evap1} \cdot \Delta t = -2.997 \times 10^{-9} \text{ kg}$$ Mass of liquid evaporating (negative value indicates vapour is condensing)

This is a smaller mass than the initial vapour mass $m_{v\_old} := 0.002672195 \times 10^{-3}\,kg$. The calculated mass transfer rate is therefore allowable.

**Step 3: Calculation of the change in gas, vapour and liquid masses in the control volume**

The change in mass of the gas, vapour and liquid over the time step are now calculated. The mass flow rate of the gas at this point in time (the start of the time step) is taken as the 'old' value corresponding to the end of the previous time step. The liquid layer velocity is negligible at this point in time (as given by $v_{L\_old} := 0\frac{m}{s}$ ). The mass flow rate of vapour out of the control volume after the condensation has occurred is calculated using the new vapour density in the control volume:

$\rho_{v\_out1} := \frac{m_{v\_old} + m_{evap1}}{V_{cv}} = 21.765 \times 10^{-3}\,\frac{kg}{m^3}$ Density of vapour leaving the control volume

$\dot{m}_{v1} := \rho_{v\_out1} \cdot G_{old} \cdot K_{v\_old} = 543.614 \times 10^{-6}\,\frac{kg}{s}$ Vapour mass flow rate out of the control volume

The change in the gas, vapour and liquid mass is now calculated using the continuity equations as given by Equations 3.3 to 3.5.

$\Delta m_{g1} := \left(\dot{m}_{g\_old.in} - \dot{m}_{g\_old}\right) \cdot \Delta t = 35.673 \times 10^{-9}\,kg$ Change in gas mass over time step

$\Delta m_{v1} := \left(\dot{m}_{v\_old.in} - \dot{m}_{v1}\right) \cdot \Delta t + m_{evap1} = -71.285 \times 10^{-9}\,kg$ Change in vapour mass over time step

$\Delta m_{L1} := -m_{evap1} = 2.997 \times 10^{-9}\,kg$ Change in liquid mass over time step

**Step 4: Calculation of the first estimate of the new temperatures of the gas mixture, liquid layer and wall**

At the start of the time step the constant volume specific heat for the gas mixture is calculated as follows:

$R_{mix1} := \frac{m_{g\_old} \cdot R_g + m_{v\_old} \cdot R_v}{m_{mix\_old}} = 279.362 \cdot \frac{J}{kg \cdot K}$ Specific gas constant of the gas mixture

$C_{Pmix1} := \frac{m_{g\_old} \cdot C_{Pg} + m_{v\_old} \cdot C_{Pv}}{m_{mix\_old}} = 1113.16\,\frac{J}{kg \cdot K}$ Constant pressure heat capacity of the gas mixture

$C_{vmix1} := C_{Pmix1} - R_{mix1} = 833.798\,\frac{J}{kg \cdot K}$ Constant volume heat capacity of the gas mixture

The change in temperature of the gas mixture, liquid layer and wall is calculated using the energy equations given by Equations 3.7 to 3.9. In order to evaluate the differential temperature change in the gas mixture the following first need to be calculated: The change in internal energy, the change in enthalpy associated with the gas mixture flow, the enthalpy transfer associated with the condensation and the convective, conductive and radiation heat transfer.

For the change in internal energy of the gas and vapour:

$\Delta U_{g1} := C_{vg} \cdot \left(T_{mix\_old} - 273\right) \cdot \frac{\Delta m_{g1}}{\Delta t} = 1.516 W$ Change in internal energy due to the change in mass of gas in the control volume

$\Delta U_{v1} := C_{vv} \cdot \left(T_{mix\_old} - 273\right) \cdot \frac{\Delta m_{v1}}{\Delta t} = -5.723 W$ Change in internal energy due to the change in mass of vapour in the control volume

For the enthalpy associated with the gas and vapour flow:

$h_{g.in} := C_{Pg}\cdot\left(T_{mix\_old.in} - 273\right) = 34.587\times 10^{3}\ \frac{J}{kg}$ Specific enthalpy carried by the gas flow into the control volume

$h_{g1} := C_{Pg}\cdot\left(T_{mix\_old} - 273\right) = 28.415\times 10^{3}\ \frac{J}{kg}$ Specific enthalpy carried by the gas flow out of the control volume

$\Delta H_{g1} := \dot{m}_{g\_old.in}\cdot h_{g.in} - \dot{m}_{g\_old}\cdot h_{g1} = 78.503\,W$ Total rate of change in energy due to gas flow

$h_{v.in} := C_{Pv}\cdot\left(T_{mix\_old.in} - 273\right) = 63.521\times 10^{3}\ \frac{J}{kg}$ Specific enthalpy carried by the vapour flow into the control volume

$h_{v1} := C_{Pv}\cdot\left(T_{mix\_old} - 273\right) = 52.185\times 10^{3}\ \frac{J}{kg}$ Specific enthalpy carried by the vapour flow out of the control volume

$\Delta H_{v1} := \dot{m}_{v\_old.in}\cdot h_{v.in} - \dot{m}_{v1}\cdot h_{v1} = -2.513\,W$ Total rate of change change in energy due to vapour flow

For the enthalpy transfer associated with the condensation:

$h_{evap1} := h_{sat}\left(T_{mix\_old}\right) = 2.544\times 10^{6}\ \frac{J}{kg}$ Enthalpy of a saturated gas at the gas mixture temperature

$\Delta H_{evap1} := \dot{m}_{evap1}\cdot h_{evap1} = -15.25\,W$ Rate of energy transfer associated with the condensation

For the internal convection and radiation heat transfer:

$Q_{conv.gL1} := h_{i1}\cdot A_{CatSurface}\cdot\left(T_{mix\_old} - T_{L\_old}\right) = 8.066\,W$ Internal convective heat transfer

$Q_{rad.gw1} := \alpha_g\cdot A_{CatSurface}\cdot\sigma\cdot T_{w\_old}^{4} - \varepsilon_g\cdot A_{CatSurface}\cdot\sigma\cdot T_{mix\_old}^{4} = -3.551\,W$ Internal radiation heat transfer

The rate of change in gas mixture temperature is therefore:

$$\Delta\dot{T}_{mix1} := \frac{\Delta H_{g1} + \Delta H_{v1} + \Delta H_{evap1} - Q_{conv.gL1} + Q_{rad.gw1} - \Delta U_{g1} - \Delta U_{v1}}{m_{mix\_old}\cdot C_{vmix1}} = 495.023\frac{K}{s}$$

The first Runge Kutta constant is now calculated and used to make the first prediction of the temperature at the mid-point of the time step:

$K_{mix1} := \Delta\dot{T}_{mix1}\Delta t = 247.511\times 10^{-3}\ K$ Predicted change in gas mixture temperature for a full time step

$T_{mix2} := T_{old} + 0.5\,K_1 = 299.216K$ Predicted gas mixture temperature at mid-point of the time step

A similar procedure is followed for the liquid layer. In the case of the liquid layer the radiation heat transfer and the enthalpy associated with the flow are absent, but an additional convective term, between the liquid layer and the wall, is added.

The change in internal energy of the liquid layer (due to the change in liquid mass) is given by:

$$\Delta U_{L1} := C_{PL}\cdot\left(T_{L\_old} - 273\right)\cdot\frac{\Delta m_{L1}}{\Delta t} = 623.743\times 10^{-3}\ W$$

For the convection from the liquid to the wall:

$$Q_{convLw1} := h_{Lw} \cdot A_{CatSurface} \cdot \left(T_{L\_old} - T_{w\_old}\right) = 5.596\,W$$

Convective heat transfer between the liquid layer and wall

The rate of change in liquid temperature is therefore:

$$\dot{\Delta T}_{L1} := \frac{-\Delta H_{evap1} + Q_{conv.gL1} - Q_{convLw1} - \Delta U_{L1}}{m_{L\_old} \cdot C_{PL}} = 44.2\,\frac{K}{s}$$

It is noted that the rate of change of liquid temperature is much lower than that in the gas temperature. This is because the high rate of heat transfer from the gas to the liquid is counter-balanced by the high rate of heat transfer from the liquid to the wall.

The first Runge Kutta constant for the liquid is now calculated and used to make the first prediction of the liquid temperature at the mid-point of the time step:

$$K_{L1} := \dot{\Delta T}_{L1} \cdot \Delta t = 22.1 \times 10^{-3}\,K$$

Predicted change in liquid temperature over the whole time step

$$T_{L2} := T_{L\_old} + 0.5 \cdot K_{L1} = 297.669\,K$$

Predicted liquid temperature at mid-point of the time step

For the wall the internal gaseous radiation heat transfer is again accounted for and the axial conduction heat transfer is also added. It is noted that because the catalytic converter channels were assumed to have an adiabatic plane at the mid-plane of the channel walls, the external convection and radiation terms of Equation 3.9 are neglected. The axial conduction heat transfer is given by:

$$Q_{cond.in} := \frac{k_{cat} \cdot A_{wcs}}{cv} \cdot \left(T_{w\_old.in} - T_{w\_old}\right) = 3.052\,W$$

Conduction into the control volume

$$Q_{cond} := \frac{k_{cat} \cdot A_{wcs}}{cv} \cdot \left(T_{w\_old} - T_{w\_old.out}\right) = 0.578\,W$$

Conduction out of the control volume

$$\Delta Q_{cond} := \left(Q_{cond.in} - Q_{cond}\right) = 2.474\,W$$

Net conductive heat flux

The rate of change in wall temperature is therefore:

$$\dot{\Delta T}_{w1} := \frac{Q_{convLw1} - Q_{rad.gw1} - \Delta Q_{cond}}{m_w \cdot C_{Pcat}} = 32.451 \times 10^{-3}\,\frac{K}{s}$$

The first Runge Kutta constant is now calculated and used to make the first prediction of the temperature at the mid-point of the time step:

$$K_{w1} := \dot{\Delta T}_{w1} \cdot \Delta t = 16.226 \times 10^{-6}\,K$$

Predicted change in wall temperature over the whole time step

$$T_{w2} := T_{w\_old} + 0.5 \cdot K_{w1} = 297.54376\,K$$

Predicted wall temperature at mid-point of the time step

**Step 5: Prediction of the change in gas, liquid and wall temperatures using the conditions at the mid-point and end of the time step**

The procedure followed in Steps 1 to 4 is repeated in order to predict the temperature gradients during the $K_2$ to $K_4$ calculations. In each case the time and temperature dependent initial values are adjusted. For the $K_2$ calculations the temperatures $T_{mix2}$, $T_{L2}$ and $T_{w2}$ are used as initial values (in the place of the 'old' values in Steps 1 to 4). The mass of gas and vapour in the control volume at the mid-point of the time step are calculated by assuming that half the change in mass of each (predicted in Step 3) will occur over half the time step.

$m_{g2} := m_{g\_old} + \frac{\Delta m_{g1}}{2} = 98.135 \times 10^{-6}\ kg$ Initial value for the gas mass for the $K_2$ calculations

$m_{v2} := m_{v\_old} + \frac{\Delta m_{v1}}{2} = 2.6366 \times 10^{-6}\ kg$ Initial value for the vapour mass for the $K_2$ calculations

The first estimate of the gradients of the gas, liquid and wall temperatures calculated at the mid-point of the time step is then used to calculate the second Runge Kutta constants for the gas mixture, liquid and wall:

$\Delta\dot{T}_{mix2} = 1972.01 \frac{K}{s}$ Gas mixture temperature gradient from $K_2$ calculations

$\Delta\dot{T}_{L2} = 40.863 \frac{K}{s}$ Liquid temperature gradient from $K_2$ calculations

$\Delta\dot{T}_{w2} = 0.2160 \frac{K}{s}$ Wall temperature gradient from $K_2$ calculations

$K_{mix2} := \Delta\dot{T}_{mix2} \Delta t = 986.004 \times 10^{-3}\ K$ Second Runge Kutta constant for the gas mixture temperature

$K_{L2} := \Delta\dot{T}_{L2} \cdot \Delta t = 20.431 \times 10^{-3}\ K$ Second Runge Kutta constant for the liquid temperature

$K_{w2} := \Delta\dot{T}_{w2} \cdot \Delta t = 108.021 \times 10^{-6}\ K$ Second Runge Kutta constant for the wall temperature

A second estimate of the temperatures at the mid-point of the time step is made:

$T_{mix3} := T_{mix\_old} + 0.5 \cdot K_{mix2} = 299.585K$

$T_{L3} := T_{L\_old} + 0.5 \cdot K_{L2} = 297.668K$

$T_{w3} := T_{w\_old} + 0.5 \cdot K_{w2} = 297.544K$

The temperatures $T_{mix3}$, $T_{L3}$ and $T_{w3}$ are the initial temperatures for the $K_3$ calculations and are used to predict the temperature gradients at the mid-point of the time step for a second time. The initial mass of gas is the same as for the $K_2$ calculations. The initial mass of vapour is adjusted to account for the two-phase mass transfer $m_{evap2}$ calculated during the $K_2$ calculations. A change in vapour mass $\Delta m_{v2}$ is calculated in the same way as $\Delta m_{v1}$ is calculated in Step 3, which gives the new initial vapour mass:

$m_{v3} := m_{v\_old} + \frac{\Delta m_{v2}}{2} = 2.7287 \times 10^{-6}\ kg$ Initial value for the vapour mass for the $K_3$ calculations

The second estimate of the gradients of the gas, liquid and wall temperatures at the mid-point of the time step is used to predict the change in each temperature for the time step.

$\Delta\dot{T}_{mix3} = 1763.95 \frac{K}{s}$ Gas mixture temperature gradient from $K_3$ calculations

$\Delta\dot{T}_{L3} = 41.84 \frac{K}{s}$ Liquid temperature gradient from $K_3$ calculations

$\Delta\dot{T}_{w2} = 0.2160 \frac{K}{s}$ Wall temperature gradient from $K_3$ calculations

$K_{mix3} := \Delta\dot{T}_{mix3} \cdot \Delta t = 881.976 \times 10^{-3}\ K$ Third Runge Kutta constant for the gas mixture temperature

$K_{L3} := \Delta\dot{T}_{L3} \cdot \Delta t = 20.92 \times 10^{-3}\ K$ Third Runge Kutta constant for the liquid temperature

$K_{w3} := \Delta\dot{T}_{w3} \cdot \Delta t = 139.267 \times 10^{-6}\ K$ Third Runge Kutta constant for the wall temperature

From which the temperatures at the end of the time step are predicted:

$T_{mix4} := T_{mix\_old} + K_{mix3} = 299.974\ K$

$T_{L4} := T_{L\_old} + K_{L3} = 297.679\ K$

$T_{w4} := T_{w\_old} + K_{w3} = 297.544K$

The temperatures $T_{mix4}$, $T_{L4}$ and $T_{w4}$ are now used to predict the temperature gradients at the end of the time step. The gas and vapour masses used as initial values at the end of the time step need to be calculated. The gas mass flow rate is dependent on the gas density and the volumetric flow rate, which is time dependent. The change in gas mass $\Delta m_{g1}/2$ from the beginning to the mid-point of the time step was calculated using the mass flow rate and density at the beginning of the time step. In a similar manner the change in gas mass $\Delta m_{g2}/2$ from the mid-point to the end of the time step is calculated using the gas density and volumetric flow rate at the mid-point of the time step. This change in gas mass over the second half of the time step is then added to the gas mass present at the mid point of the time step. The gas mass at the end if the time step is then:

$$m_{g4} := m_{g2} + \frac{\Delta m_{g2}}{2} = 96.101\times 10^{-6}\ kg$$

The initial vapour mass at the end of the time step is calculated in a similar manner, but as the mass flow rate at the mid-point of the time step has been approximated twice, the average change in vapour mass over the second half the time step is calculated. This is added to the vapour mass present at the mid-point of the time step.

$$m_{v4} := m_{v2} + \frac{\frac{\Delta m_{v2}}{2} + \frac{\Delta m_{v3}}{2}}{2} = 2.786\times 10^{-6}\ kg$$

The procedure laid out in steps 1 to 4 is now applied a final time, in order to calculate the gas mixture, liquid and wall temperature gradients at the end of the time step. The final Runge Kutta constants are also calculated.

$\dot{\Delta T}_{mix4} = 1518.47\frac{K}{s}$ Gas mixture temperature gradient from $K_4$ calculations

$\dot{\Delta T}_{L4} = 60.539\frac{K}{s}$ Liquid temperature gradient from $K_4$ calculations

$\dot{\Delta T}_{w4} = 0.3035\frac{K}{s}$ Wall temperature gradient from $K_4$ calculations

$K_{mix4} := \dot{\Delta T}_{mix4}\cdot\Delta t = 759.234\times 10^{-3}\ K$ Fourth Runge Kutta constant for the gas mixture temperature

$K_{L4} := \dot{\Delta T}_{L4}\cdot\Delta t = 30.27\times 10^{-3}\ K$ Fourth Runge Kutta constant for the liquid temperature

$K_{w4} := \dot{\Delta T}_{w4}\cdot\Delta t = 151.767\times 10^{-6}\ K$ Fourth Runge Kutta constant for the wall temperature

**Step 6: Calculation of the new gas mixture, liquid and wall temperatures**

The Runge Kutta constants $K_{1\text{-}4}$ for the gas mixture, liquid and wall temperatures are now used to calculate the 'new' value of each temperature using the weighted average given in the definition of the Runge Kutta method:

$$T_{mix} := T_{mix\_old} + \frac{K_{mix1} + 2 \cdot K_{mix2} + 2 \cdot K_{mix3} + K_{mix4}}{6} = 299.89959 \text{ K}$$

$$T_L := T_{L\_old} + \frac{K_{L1} + 2 \cdot K_{L2} + 2 \cdot K_{L3} + K_{L4}}{6} = 297.67123 \text{ K}$$

$$T_w := T_{w\_old} + \frac{K_{w1} + 2 \cdot K_{w2} + 2 \cdot K_{w3} + K_{w4}}{6} = 297.54388 \text{ K}$$

**Step 7: Calculation of the 'new' gas, liquid and vapour masses**

The 'new' values for the mass of gas, vapour and liquid in the control volume are now calculated. Since the mass of gas is a time dependent property, but is not influenced by the predicted temperatures, the mass of gas calculated at the end of the time step $m_{g4}$ is the final mass of gas in the control volume.

In the case of the vapour, the calculations performed at the end of the time step made a final prediction of the two-phase mass transfer $m_{evap4}$. The total amount of two-phase mass transfer occurring over the time step is approximated as the weighted average of the four $m_{evap}$ values calculated:

$$m_{evap} := \frac{m_{evap1} + 2 \cdot m_{evap2} + 2 \cdot m_{evap3} + m_{evap4}}{6} = -499.526 \times 10^{-12} \text{ kg}$$

The new mass of vapour is now calculated using the same method as in Step 3.

$$\rho_{v\_out} := \frac{m_{v\_old} + m_{evap}}{V_{cv}} = 21.773 \times 10^{-3} \frac{\text{kg}}{\text{m}^3}$$

$$\dot{m}_v := \rho_{v\_out} \cdot G \cdot K_{v\_old} = 544.125 \times 10^{-6} \frac{\text{kg}}{\text{s}}$$

$$\Delta m_v := \left(\dot{m}_{v.in} - \dot{m}_v\right) \cdot \Delta t + m_{evap} = -69.052 \times 10^{-9} \text{ kg}$$

$$m_v := m_{v\_old} + \Delta m_v = 2.603 \times 10^{-6} \text{ kg}$$

The final mass of the gas in the control volume is now:

$$m_{mix} := m_g + m_v = 98.704 \times 10^{-6} \text{ kg}$$

The final mass of liquid is decided by the initial mass of liquid and the final amount of two phase mass transfer.

$$m_L := m_{L\_old} - m_{evap} = 154.535 \times 10^{-6} \text{ kg}$$

**Step 8: Calculation of the new pressure in the control volume**

The pressure in the control volume is calculated by means of the momentum equation (given by Equation 3.12, but with the liquid layer velocity terms neglected). If evenly distributed over the inner surface of the control volume, the mass of liquid would produce a film of $z_L = 0.318$ μm thick. The liquid-gas interfacial coefficient of friction $C_{gL}$ (given by Equation 2.29) will therefore tend towards the value of gas-wall interfacial coefficient of friction $C_{gw}$. This allows the wall shear force to be calculated.

$C_{gw} := 0.079\,Re_{D4}^{-0.25} = 0.023$ Coefficient of friction for laminar flow at the gas-wall interface

$\tau_i := 0.5 \cdot C_{gw} \cdot \rho_4 \cdot v^2 = 80.63 \times 10^{-3}$ Pa Shear force at the gas-wall interface

The gas mixture velocity and the axial velocity of the condensing mass are given by:

$v_{mix} := v \cdot K_{v\_old} = 2.0366 \frac{m}{s}$ Gas mixture velocity

$v_{evap} := v_{mix} = 2.0366 \frac{m}{s}$ Axial velocity of the condensing vapour

If evaporation had occurred, the axial velocity of the evaporating mass would have been equal to the liquid velocity.

The new pressure in the control volume is now calculated using Equation 3.12:

$$P := \frac{(v_{mix.in} - v_{mix}) \cdot (\dot{m}_{g.in} + \dot{m}_{v.in}) - m_{mix} \frac{dv}{dt} + \dot{m}_{evap} \cdot (v_{evap} - v_{mix}) - \tau_i \cdot A_{CatSurface} + P_{old} \cdot A_{wcs}}{A_{CatFlow}} = 100.083 \times 10^3 \text{ Pa}$$

**Step 9: Calculation of the new value of $K_V$**

The new value of the volumetric flow rate adjustment factor $K_V$ (given by Equation 3.13) is calculated by using the ideal gas equation to predict a volume for the gas mixture in the control volume. The new gas mixture mass, temperature and pressure have already been calculated, while the specific gas constant still needs to be calculated.

$R_{mix} := \frac{m_g \cdot R_g + m_V \cdot R_V}{m_{mix}} = 279.495 \frac{J}{kg \cdot K}$ New specific gas constant of the gas mixture

$V_{ideal} := \frac{m_{mix} \cdot R_{mix} \cdot T_{mix}}{P} = 85.724 \times 10^{-6}\ m^3$ Volume the gas mixture should occupy according to the ideal gas equation

$K_V := \frac{V_{ideal}}{V_{cv}} = 0.699$ Volumetric flow rate adjustment factor for next time step

The result $K_V = 0.699$ indicates that the gas mixture flow out of the control volume needs to be reduced. This is reasonable since the gas has contracted due to cooling (compared to the incoming temperature) and the mass of gas in the control volume was reduced by condensation.

The ‘new’ values for the control volume are stored in vector form to be used as the inputs to the calculations for the next time step.

# APPENDIX D: Sensor Manufacturing Drawings

The shielded sensor design described in Section 4 consists of a thin thermocouple wire inside a radiation shield assembly. The manufacturing drawings of the inner and outer radiation shields and an assembly drawing are supplied as follows:

| DRAWING No. | DESCRIPTION | PAGE |
|---|---|---|
| SSD-A1 | THERMOCOUPLE RADIATION SHIELD | 1 OF 3 |
| SSD-01 | INNER SHIELD | 2 OF 3 |
| SSD-02 | OUTER SHIELD | 3 OF 3 |

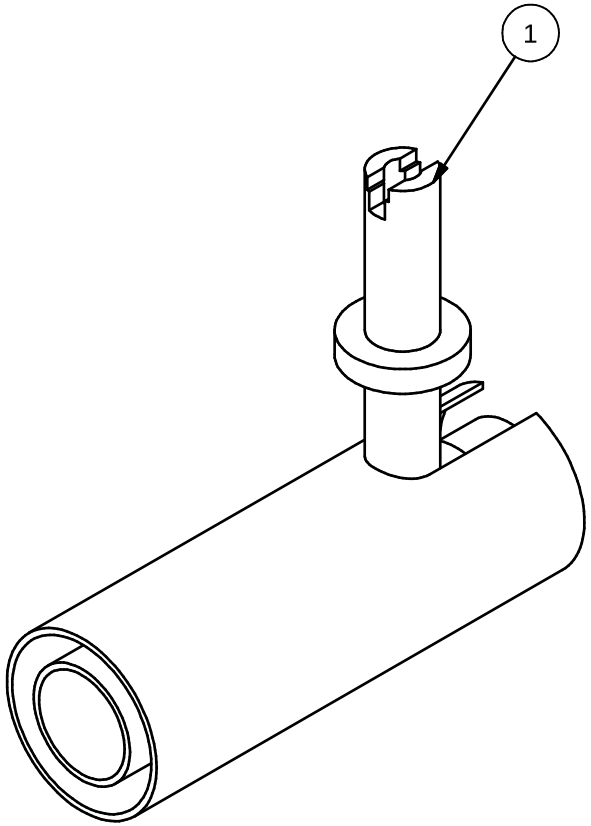


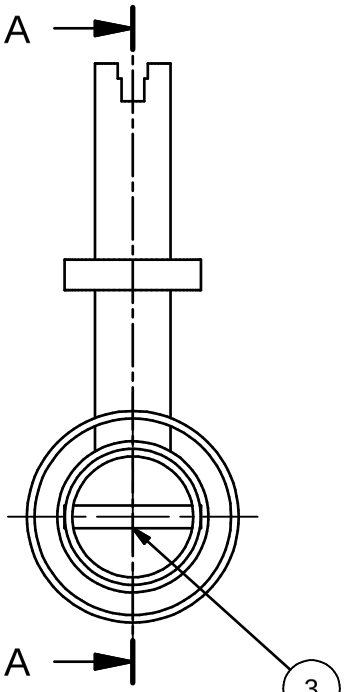


A-A ( 2 : 1 )

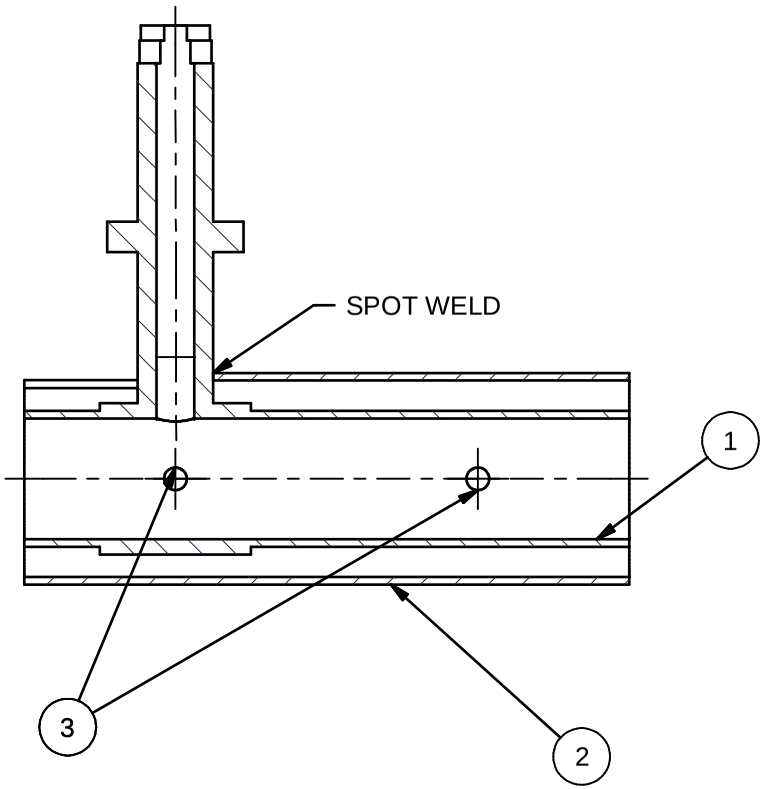


| ITEM | DESCRIPTION | QTY | MATERIAL / SPECIFICATIONS |
|---|---|---|---|
| 3 | HORIZONTAL SUPPORT PIN | 2 | Ø1.5X9mm STAINLESS STEEL WIRE |
| 2 | OUTER SHILED | 1 | SSD-02 |
| 1 | INNER SHIELD | 1 | SSD-01 |

**UNIVERSITY OF STELLENBOSCH**

SCALE 2:1
DIM IN mm

TITLE: THERMOCOUPLE RADIATION SHIELD

STUDENT NUMBER 13902229 | DRAWN BY L HAWORTH | REVIEWED | DATE 29/01/2007 | PAGE 1 OF 3 PAGES | No. SSD-A1

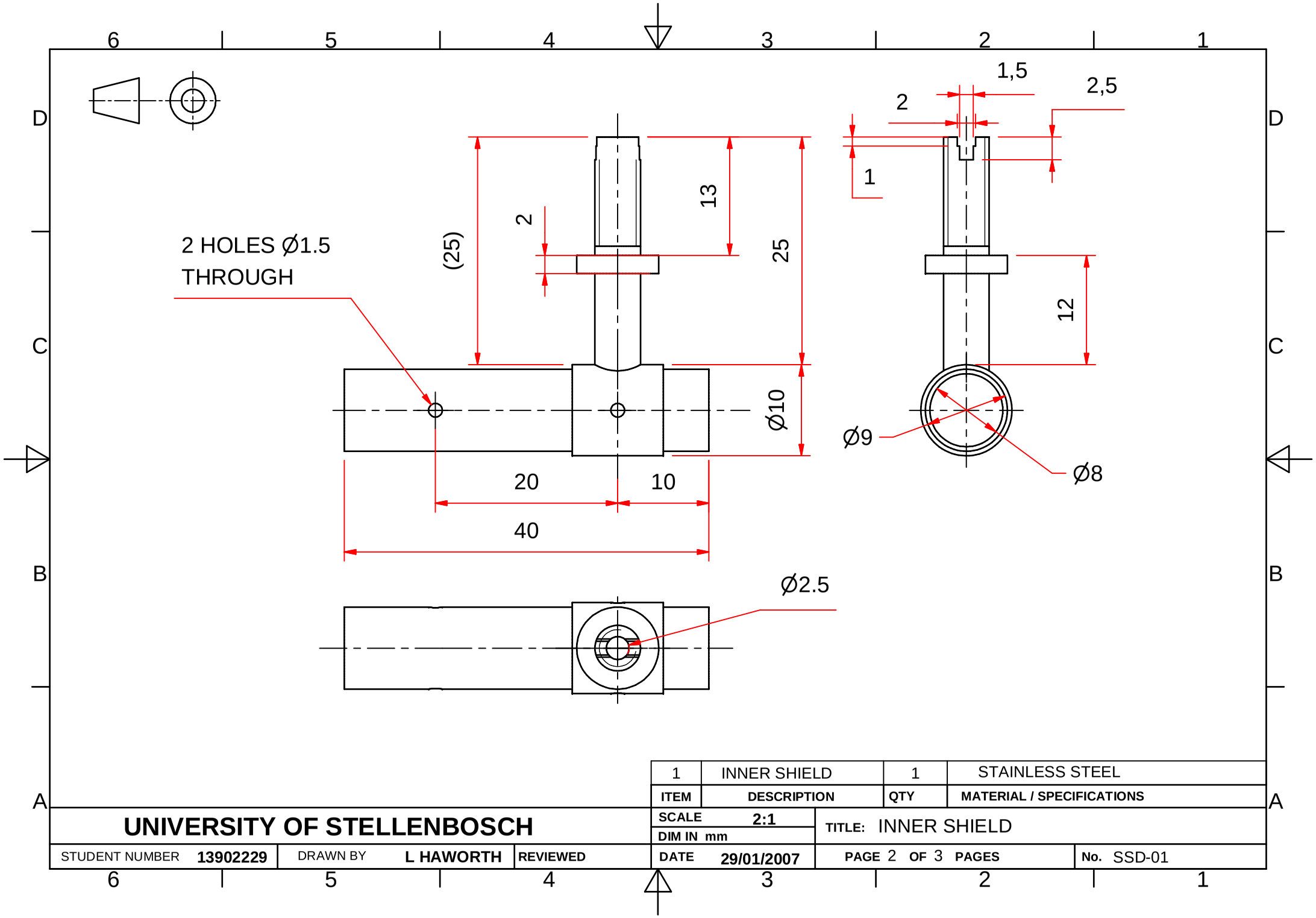


| ITEM | DESCRIPTION | QTY | MATERIAL / SPECIFICATIONS |
|---|---|---|---|
| 1 | INNER SHIELD | 1 | STAINLESS STEEL |

**UNIVERSITY OF STELLENBOSCH**

| | | | |
|---|---|---|---|
| SCALE 2:1 | | TITLE: INNER SHIELD | |
| DIM IN mm | | | |
| STUDENT NUMBER 13902229 | DRAWN BY L HAWORTH | REVIEWED | DATE 29/01/2007 |
| PAGE 2 OF 3 PAGES | | No. SSD-01 | |

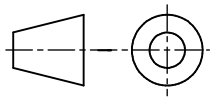

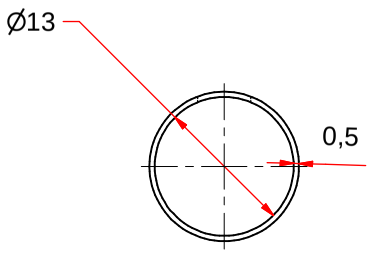


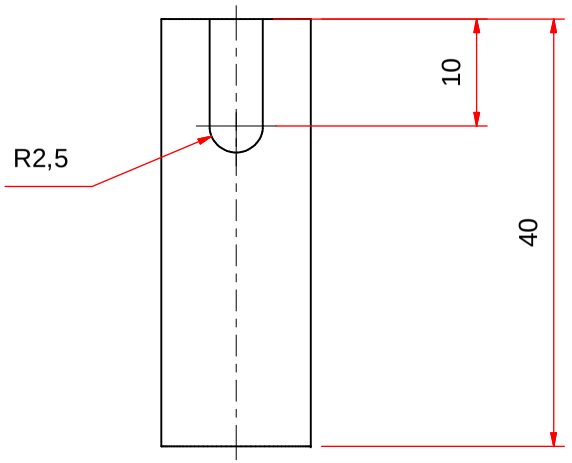


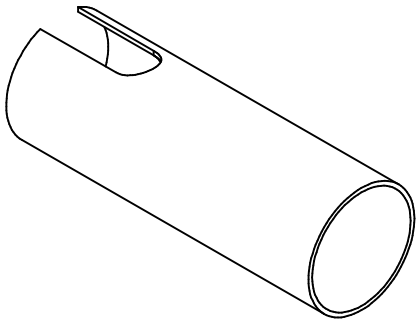

| ITEM | DESCRIPTION | QTY | MATERIAL / SPECIFICATIONS |
|---|---|---|---|
| 1 | OUTER SHIELD | 1 | STAINLESS STEEL |

**UNIVERSITY OF STELLENBOSCH**

| | | | | | |
|---|---|---|---|---|---|
| STUDENT NUMBER 13902229 | DRAWN BY L HAWORTH | REVIEWED | SCALE<br>DIM IN mm mm | TITLE: OUTER SHIELD | |
| | | | DATE 29/01/2007 | PAGE 3 OF 3 PAGES | No. SSD-02 |